# Microfluidics enhanced synthesis of micellar nanostructures

Joshua J Cardiel

A dissertation submitted in partial fulfillment of the
requirements for the degree of

Doctor of Philosophy

University of Washington

2014

Reading Committee:

Amy Q Shen, Chair

Lilo D Pozzo, Chemical Engineering Department

Liguo Wang, Biological Structure Department

Program Authorized to Offer Degree:
UW Dual Ph.D. in Mechanical Engineering & Nanotechnology

# Microfluidics enhanced synthesis of micellar nanostructures

Joshua J Cardiel

A dissertation submitted in partial fulfillment of the
requirements for the degree of

Doctor of Philosophy

University of Washington

2014

Program Authorized to Offer Degree: UW Dual Ph.D. in Mechanical Engineering & Nanotechnology

University of Washington

**Abstract**

Microfluidics enhanced synthesis of micellar nanostructures

Joshua J Cardiel

Chair of the Supervisory Committee:
Professor Amy Q Shen
Mechanical Engineering

Surfactant molecules can self-assemble into various morphologies under proper combinations of surfactant concentration, temperature, and flow conditions. In equilibrium, micelles can transition from entangled to branched structures with increasing ionic strength and temperature. Under flow conditions, micellar structure transition can follow different trajectories. In the present work, the structural and rheological evolution of both ionic and non-ionic micellar solutions are studied. When both ionic and non-ionic micellar solutions are subjected to strain rates $\sim 10^3$ $s^{-1}$ and strain $\sim 10^3$, we observe the formation of stable flow-induced structured phases (FISPs), with entangled, branched, and multi-connected micellar bundles, evidenced by electron microscopy (cryo-EM, TEM, and SEM) and small-angle neutron scattering (SANS). The rheological properties of both ionic and non-ionic micellar solutions and their corresponding FISPs are obtained by using one point passive microrheology and two point passive microrheology. The rheological properties variation from the original micellar solutions to their corresponding FISPs is associated with the structural evolution from the precursor to FISPs. The formation of FISPs is correlated with local micellar gradients concentrations, hight stretching in the microposts arrays, entropic fluctuations, flow kinematics, and microspatial confinement. Finally, some potential sensing applications and nanotemplating uses of the FISPs are presented.

## TABLE OF CONTENTS

Page

# LIST OF FIGURES

## ACKNOWLEDGMENTS

I would like to express sincere appreciation to my adviser Professor Amy Q. Shen, for her valuable advice, knowledge and support during the last five years. Also, I would like to thank my undergrad adviser Prof. Baltasar Mena Iniesta for introducing me to the world of science. Without his advise the beginning of this journey would have been more difficult.

I would also like to thank my supervisory committee members Liguo Wang, Lilo D Pozzo, Jae-Hyun Chung and Guozhong Cao for their support and providing fresh perspectives for this research. Thanks to Prof. Pozzo and her student Pablo who taught me how to do scattering (SANS&SAXS), though I still have to learn a lot! Thanks to Prof. Wang and his student Lige who taught me how to perform electron-microscopy (TEM, cryo-EM). Thanks to Prof. Chung who taught me some approaches to develop basic sensors. Thanks to Prof. Elliot Fried for all his guidance during the theoretical modeling proposed in this dissertation.

I wish to thank Maria Hopper for all her help during this journey. With her help all this adventure was way more easier. I still remember that on my first Friday in Seattle she and her husband invited me to have dinner. That night was a good start to this journey. Thanks Maria.

I extend my gratitude to all my lab-mates (Rachel, Jess, Perry, Shilpa, Ya, Di, and Neville), external labmates (Pablo, Lige, Shin, and Naty). Thank you guys for your help and friendship.

Shin and Naty, thanks a lot for making me drunk $n$–times (where $n \gg 1$), those nights playing pool and having nonsense conversations were great. Shilpa, I will miss those late

afternoon/night existential talks (a.k.a. a long monologue complaining about my life), also thanks for all your help and time during my pre-presentations for master thesis, general exam, and conferences. Pablo, I hope we can keep those coffee breaks talking about... you know what. Ya, thanks for being my right hand in the lab, also thanks for making me addicted to cookies and green tea. Zenko, thanks for all the super late ($\sim$1 a.m.) coffee breaks where we talked about life (most of the times you ended up calling me stubborn). Also, thanks for making me addicted to protein milkshakes, though they never worked. Shirin, thanks for that symbiosis that we made at the beginning of grad school. We did really well surviving the cultural shock (a.k.a. loneliness). To all of you thanks a lot and I stay in touch.

This research would not have been possible without the staff and facilities of Nanotech User Facility, Mass Spectrometry Facility, MOLES, and the Nanomanufacturing Lab at the University of Washington. Part of this work was carried out at the Pacific Northwest National Laboratory (PNNL) and at the National Institute of Standards and Technology (NIST). This work was supported by NSF (CBET-CAREER 0852471), CONACYT and University of Washington Royalty Research Fund 65-5738.

## DEDICATION

To my family, they made sure I got to where I am today, by laying a foundation on which they were certain anything could be built. Sincere appreciation to my aunt Lety for all her support during these years. Ely, without all your help this adventure would never have happened, thank you.

# Chapter 1

# INTRODUCTION

## *1.1 Wormlike micelles*

Surfactant molecules in aqueous solutions can self-assemble into different structures such as spherical micelles, cylindrical micelles, lamellar phases, and vesicles [1]. The morphology of these self-assembled structures is influenced by surfactant concentration, temperature, external additives (e.g., co-surfactants or salts), and flow conditions. The packing of the hydrophilic tails of surfactant molecules normally determines the smallest dimension of the surfactant aggregate, hence the molecular structures determines the self-assembled shape.

The surfactant packing parameter ($p = v/(a_0 l_c)$) is a geometric ratio of the volume $v$ of the surfactant, to the area of the head group $a_0$, and surfactant tail length $l_c$ [1]. The tail typically consists of hydrocarbon chains $n_c$ carbon atoms,

$$\begin{aligned} l_c(\mathring{A}) &\approx 1.54 + 1.265 n_c \\ v(\mathring{A}^3) &\approx 24.4 + 26.9 n_c \end{aligned} \tag{1.1}$$

the head group can be ionic or non-ionic, and $a_0$ is more difficult to estimate. Spherical micelles are the most common aggregates formed in surfactant solutions. Spherical micelles present a packing parameter of $p \sim 1/3$, while cylindrical micelles $p \sim 1/2$. The addition of salts screens electrostatic interactions between charged head groups thus increasing $p$ by a reduction of $a_0$ (see figure 1.1). The linear growth of wormlike micelles can result in overall contour length ($\bar{L}_c$) of microns. The aggregation of number is a function of surfactant volume fraction $\phi$ and the scission energy ($E_s c$), which is the energy required to break a micelle into two parts

$$\bar{L}_c \sim \phi^{1/2} e^{(E_s c/(2k_B T))} \tag{1.2}$$

where $k_B T$ is the thermal energy. For non-ionic micelles the prediction of $\bar{L}_c$ is determined

by

$$\bar{L}_c \sim 2\phi^{1/2} e^{(E_c/(2k_BT))} \tag{1.3}$$

where $E_c$ is the end-cap energy.

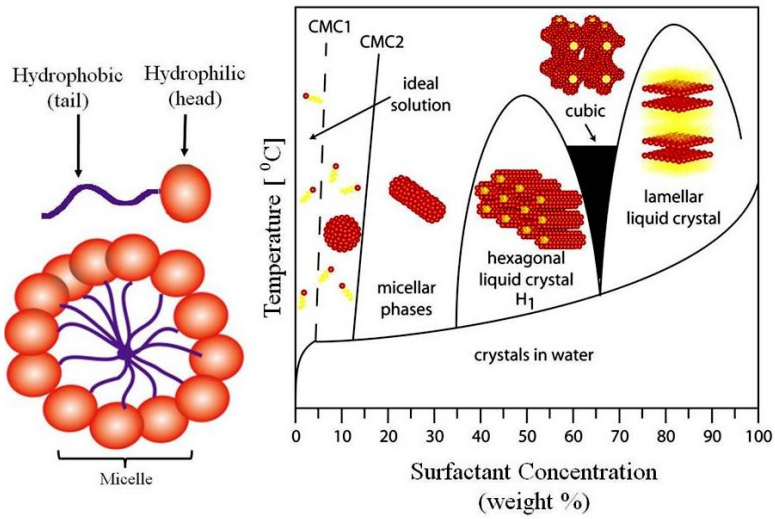


Figure 1.1: Phase diagram for CTAB micelles. The microstructure varies as a function of surfactant and temperature.

### *1.2 Micellar structures*

Cylindrical micelles have a moderate spontaneous curvature. The energy of these type of aggregates is optimized when the curvature is uniform everywhere, forming long linear structures [1]. The entropy term introduces a degree of randomness through the wormlike micelles, thus conformation entropy is added in the manner similar to the entropy of polymeric structures, and then wormlike micelles can have topological defects, in the form of end-caps, branch junction points, or combination of both [2–5]. The creation of entangled structures depends on the surfactant geometry, salinity and surfactant concentration. The possibility of connected structures was established about 30 years ago by Porte *et al.* [6]. Porte *et al.* used a model that related the polymorphism of the micelles to local free energy. Hence, with higher salt concentrations, the entangled linear micelles can transition to branched

and multi-connected micellar networks, revealed by complementary techniques such as rheological measurements, scattering techniques and electron microcopy imaging [6–19]. This structural transition has been related to the zero shear viscosity reaching a maximum with increasing salt concentration.

Additionally, wormlike micellar solutions are known to exhibit a variety of interesting phenomena, some of which are shear banding [20,21], shear thickening [22,23], shear-induced transitions and instabilities, and flow-induced structure formation [24–30]. Wormlike micelles have also found applications in oil recovery, drag reduction, nano-templating, and many biomedical and health care products [31–33]. Despite widespread use in different fields, the microscopic structures and the mechanisms by which wormlike micelles form under flow is not fully understood and, thus, the study of their rheological and other dynamical behavior is still a prevalent area of research. Although some nonionic surfactant solutions can form wormlike micelles [34–45], the majority of studies have focused on ionic surfactant solutions [4]. In views of biomedical as well as biotechnological applications, nonionic micellar solutions are preferred over ionic surfactant systems due to their electrolyte-free environment, biocompatibility, and less eco-toxic properties. In this dissertation the use of ionic and non-ionic micellar solutions is investigated.

Wormlike micelles are usually compared with polymer structures due to their viscoelastic properties and entangled structure. In a flexible polymer system, the size of the flight step segment is so short that the distance between the entangled cross points is never reached. However, in wormlike micelles the size of the step flight (Kuhn length) is comparable with the distance between entanglements points. Several types of semiflexible polymers systems can form different structures comparable with the structures created by micellar chains. Thus, it is possible to extrapolate the microstructural parameters of polymers to those of the entangled wormlike micelles. The polymer entangled structure is a strong function of the persistence length $l_p$ and the diameter of the semiflexible polymer $d$. Therefore, it might be expected that wormlike micelle structures show strong function of $l_p$ and $d$. Moreover, other microstructural parameters in wormlike micelles can be extracted from analogous polymers system such as: Contour length $L$ which is the average length of the wormlike micelle, mesh size $\xi$ as the distance between two wormlike micelles, and entanglement length $l_e$ defined as

the distance between two cross points in the entangled structure.

### *1.3 Flow-induced structures*

Flow-induced structure (FIS) formation has routinely been reported in solutions of wormlike micelles; however, until now these structures were all temporary and would decay upon cessation of the flow [5, 22–25]. The transient structures were first reported by Rehage and Hoffman [5] when a wormlike micellar solution (aqueous solution of cationic surfactant cetyltrimethylammonium bromide (CTAB) and organic salt sodium salicylate (NaSal) formed a gel-like structure under shear flow above a critical shear rate at low surfactant concentration. They referred to this gel-like structure as *shear-induced structure* **(SIS)** because upon cessation of the flow, the structures would disintegrate. Pine *et al.* [24, 25] also observed the appearance of SIS which formed "gel-like" fingers in wormlike micellar solutions ([0.1-7]/[0.1-7] mM CTAB/NaSal and 7.5/7.5 mM of TTAA/NaSal) sheared in a Couette cell. They noticed that the shear viscosity increase of the wormlike micellar solution coincided with the onset of the SIS formation. In addition, they predicted the existence of wormlike micellar bundles with a diameter of $\sim$ 200 nm based on the small angle light scattering (SALS) patterns. The relaxation time of the SIS ranged from several seconds to a couple of hours [24]. Similarly, others observed birefringent SIS formation in a surfactant and salt solution. After shearing stopped the birefringent structures quickly disappeared [46]. Kadoma *et al.* showed that CTAB/NaSal (0.03/0.24 M) based SIS consisted of highly elongated and locally-concentrated micellar strings from time-dependent SALS studies under a simple shear flow [13]. These SIS have been widely studied using birefringence, light scattering, neutron scattering, x-ray scattering, and nuclear magnetic resonance.

Irreversible flow induced structures from wormlike micelles were first reported by Vasudevan *et al.* [30] in 2010. A semi-dilute CTAB/NaSal ([CTAB] = 50 mM, [NaSal] = 16 mM) based shear-thickening precursor solution formed a stable "gel-like" *flow-induced structured phase* (**FISP**) after the precursor flowed through a microfluidic tapered channel packed with glass beads (20-100 $\mu$m in diameter). It is believed that this irreversible "gel-like" FISP occurs from a combination of the high rates of strain ($\dot{\epsilon} \sim$ 5,000 s$^{-1}$) and

from the extensional characteristics of the flow. The FISP maintained stable for more than a year, at temperature $\sim$23$\pm$2°C subsequent to the cessation of the flow. With the same wormlike micellar solution and micropost arrays of gap size (7 $\mu$m), Dubash *et al.* [47] formed the FISP and found that the rheological properties of the FISP were at least one order of magnitude larger than those of the precursor micellar solution. Cheung *et al.* [48] extended this work by adding Nile Red dye (a fluorescent dye whose intensity is related to the CTAB concentration) to the precursor and tracked the local micellar concentrations during flow. They reported that the micropost configuration could generate local micellar concentration variation up to 25% that strongly correlated with the FISP. Of note is that the majority of direct observations of transient flow-induced structures in experiments has involved purely shear flows. In contrast, the flow which results in irreversible structure formation such as FISP has both shear and extensional flow components and the rates of strain are generally several orders of magnitude larger than those in the purely shear flows.

### *1.4 Objectives and Overview*

The goal of this dissertation is to investigate the rheology, dynamics, and microstructure of the FISPs (see figure 1.2). The experimental results are categorized within existing literature. The organization of this dissertation is as follows. Chapter 2 introduces the experimental techniques used to characterize the micellar solutions (precursors) and their corresponding FISPs. Chapters 3, 4 and 5 show the structure and rheology, as well as, explain the formation of FISPs by using organic salts (e.g., NaSal and SHNC) and non-ionic surfactants. Chapter 6, presents the use of NaSal based FISP to form nano-torus micellar bundles for potential nanotemplating applications. Chapter 7, shows the use of NaSal based FISP to encapsulate single-walled carbon nanotubes (SWCNT) for pH sensing. Chapter 8 presents the use of the non-ionic FISP for glucose sensing applications. Finally, Chapter 9 shows some suggestions for future work.

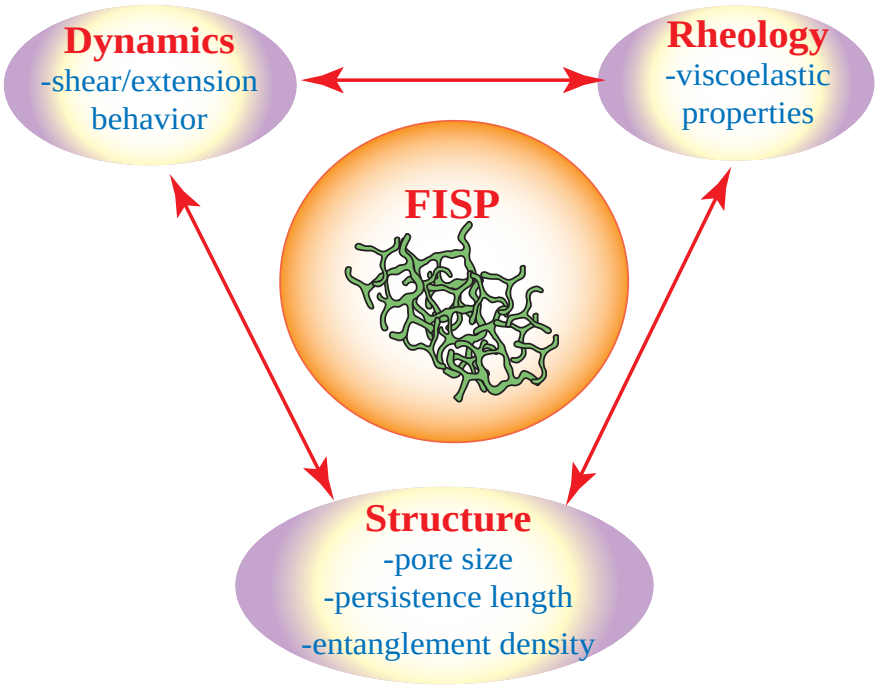


Figure 1.2: Structure, Dynamics, and Rheology of FISPs

# Chapter 2

# MATERIALS AND METHODS

Three micellar solutions were investigated in the present work. One cationic micellar solutions composed by cetyltrimethylammonium bromide (CTAB) and sodium salicylate (NaSal), and a second cationic micellar solution composed by CTAB and the organic salt 3-hydroxy naphthalene-2-carboxylate (SHNC). A third non-ionic micellar solution composed by Polyoxyethylene(20) sorbitan monooleate, also known as Tween-80, and Monolaurin (ML) was also studied. The three micellar solutions (precursors) exhibited the formation of ionic and non-ionic FISPs when subjected to high strain rates. The rheological and structural characterizations of the precursor and their corresponding FISP was performed by using cryo-electron microscopy (cryo-EM), transmission electron microscopy (TEM), scanning electron microscopy (SEM), small-angle neutron scattering (SANS), one point and two point passive microrheology, bulk rheometry, and ultra-violet spectroscopy. The next subsections briefly describe the precursor preparation, FISPs formation, and a short background for each technique used to characterize the precursors and their corresponding FISPs.

## *2.1 Materials*

### *2.1.1 NaSal/CTAB micellar solution*

Two ionic micellar solutions (precursors) were used to form ionic FISP. Both precursors were semi-dilute and consist of CTAB and NaSal in an aqueous solution. The shear-thickening ($\text{precursor}_{50}$, [CTAB] = 50 mM) and shear thinning ($\text{precursor}_{100}$, [CTAB] = 100 mM) solutions have concentration ratio [NaSal]/[CTAB] = 0.32 to maintain proportionality of the electrostatic interaction. Both solutions are made with DI water, surfactant cetyltrimethylammonium bromide (CTAB) (Sigma Aldrich Co.), and organic salt sodium salicylate (NaSal) (Sigma Aldrich Co.). The solutions were prepared by adding the appro-

priate amounts of CTAB and NaSal to DI water and mixing for 4 hours using a magnetic stir bar, and were then left at rest under room temperature for two days to equilibrate.

*2.1.2 SHNC/CTAB micellar solution*

The wormlike micellar solution (precursor) was an aqueous mixture of the cationic surfactant cetyltrimethylammonium bromide (CTAB), purchased from Sigma-Adrich (Saint Louis, MO) and the organic salt 3-hydroxy naphthalene-2-carboxylate (SHNC), purchased from TCI America (Portland, OR). All chemicals were used as received. The solution was prepared by adding the appropriate amount of CTAB and SHNC to deionized (DI) water and mixing for 24 hours. The precursor was left at rest for 1 week to equilibrate. The precursor concentration was fixed at [CTAB=45 mM] with the molar ratio of R = [SHNC]/[CTAB] = 0.32.

*2.1.3 Non-ionic micellar solution*

Polyoxyethylene(20) sorbitan monooleate, also known as Tween-80, was purchased from Fisher Scientific (Pittsburgh, PA, USA). Monolaurin (ML) was a commercial product from Tokyo Chemical Industry Co.Ltd., America (TCI AMERICA). All the chemicals were used as received. The precursor was prepared by adding appropriate amount of Tween-80 and ML in deionized water and mixing by a magnetic stir bar at room temperature for 24h, and then leaving the solution at rest for 2 days to ensure equilibrium before experiments. Based on the partial ternary phase diagram of water/Tween-80/ML system at 25 °C presented by Sharma *et al.* [39], micelles can be formed when the concentration of Tween-80 is larger than 20 wt%. In this work, we choose 25 wt% of Tween-80 and the concentration of ML at a weight ratio $\chi = 0.09$ ($\chi$ = ML/(ML+Tween-80)) in total surfactants, due to its relatively low zero shear viscosity of the solution ($\sim$ 0.1 Pa·s), enabling us to pump the precursor solution through the microfluidic device.

*2.1.4 Microfluidic Device Fabrication*

The microfluidic devices were fabricated by using standard soft lithography techniques [49]. Briefly, a thin layer of SU-8 2050 photoresist (MicroChem Corp., Newton, MA) was spun onto a silicon wafer and cured. A Heidelberg $\mu$PG-101 machine (Heidelberg Instruments

GmbH, Heildelberg, 45 Germany) at 4× speed and 75% of 18 mW was applied to write the mold of microchannel onto the photoresist. The wafer was subsequently cured, developed, and surface treated to render it hydrophobic. Modeling glue sticks the silicone tubing ports at the designed inlets and outlets of the microchannel. A mixture 10:1 of Sylgard 184-PDMS elastomer was poured onto the etched wafer, desiccated, and cured at 60 °C for ∼1 h. The resulting PDMS cast was peeled off from the wafer and plasma bonded onto a glass-slide using a Femnto plasma cleaner (Diener Electronic). A syringe pump (Harvard apparatus) was used to pump the precursor solution into the device through the inserted polyethylene tubing (Intramedic). The PDMS-glass microfluidic device has a channel height of ∼75 $\mu$m and total channel width of 1.26 mm containing a hexagonal array of microposts with diameter of 100 $\mu$m and spacing of 15 $\mu$m.

### *2.1.5 Microheater Device Fabrication*

Gold microheaters were fabricated to study the localized temperature behavior of the FISP. We used gold liftoff procedure to pattern the microheaters onto glass cover slides (GCS). First, a layer of chrome (∼15 nm) was deposited onto a GCS by using chemical vapor deposition process (CVP). Then, a second layer of gold (∼200 nm) was deposited on the GCS with the chrome layer. Then, the photoresist (AZ–1512) was spun onto the gold-GCS at 3000 RPM, a nominal thickness of ∼1.2 $\mu$m was obtained. Then, the photoresist onto the gold-chrome-GCS was exposed with the microheater design and developed. Finally, the remaining photoresist, and the metal on top of the GCS, was removed using chrome etching and gold etching processes, as well as, acetone bath. Figure 2.1 (A) shows the final gold microheater patterned onto the GCS. After the microheater were fabricated, we bonded them onto the PDMS microchannel containing the hexagonal microposts array. Figure 2.1 (B) presents the microheater right after the microposts array with some FISP-like fingers formed at room temperature. DC voltage and current was applied to vary the resistance of the microheaters, hence, temperature could be varied. The microheater and a thermocouple were connected to a power-source and computer with a home-made LabView program to control the temperature. The experimental error of the microheater was ∼1.5±0.3 °C.

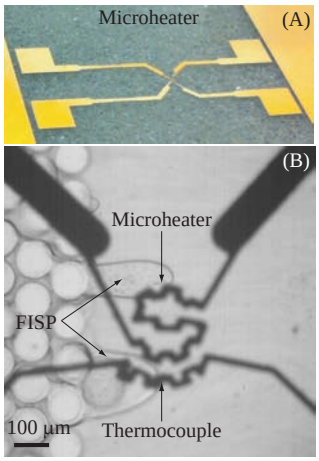


Figure 2.1: (a) Gold microheater used to study the temperature response of the FISPs. (b) Microheater bonded onto the hexagonal microposts array; (b) shows some SHNC-based FISP-like finger formed at room temperature.

## *2.2 Methods*

The rheological behavior of most micellar solutions, can exhibit many regimes depending on the scale, amplitude, and rate of strain imposed. Generally speaking, there are two types of rheological techniques to study the viscoelastic response of micellar solutions: macrorheology and microrheology (see figure 2.2). This section provides a brief description of these two techniques.

### *2.2.1 Macrorheology*

For the precursors, steady shear rheometry and oscillatory-shear rheometry were performed using a stress controlled rheometer (AR 2000, TA Instruments). The temperature was varied from at 23 to 60 °C. Acrylic cone-plate (40 mm in diameter and 1° of truncation angle) and aluminum cone-plate geometries (60 mm in diameter and 2° of truncation angle) geometries were used for all measurements. Standars rheological parameters (zero shear viscosity $\eta_0$, relaxation time $\lambda_{\text{eff}}$, and elastic modulus $G_0$) and rheological measurements were performed. Below is a brief description of the rheological parameters and measurements performed. The

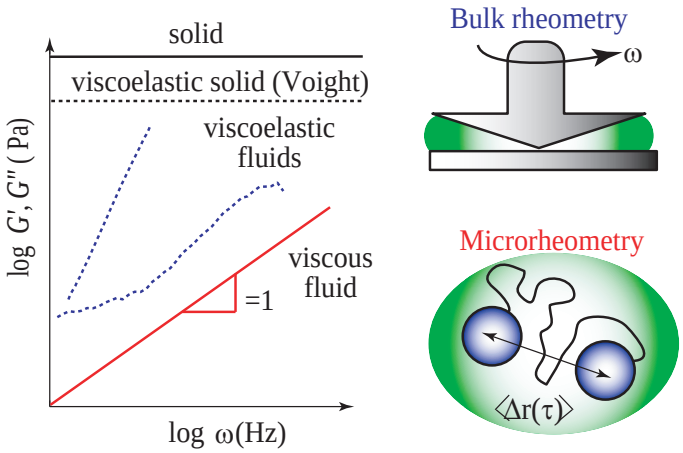


Figure 2.2: Schematic illustration of frequency-dependent shear moduli for typical fluids, solids, viscoelastic solids described by Voigt model, and viscoelastic liquids described by the Maxwell model.

shear stress $\sigma$ is defined as the applied force $f$ divided by the contact area $A$:

$$\sigma \equiv \frac{f}{A} \tag{2.1}$$

and the shear strain is defined as $\gamma$ as the displacement ($\Delta x$) of a fluid divided by its thickness $h$:

$$\gamma \equiv \frac{\Delta x}{h} \tag{2.2}$$

If a fluid is completely solid, then the stress is proportional to the strain. The constant of proportionality (shear modulus) is defined as:

$$G \equiv \frac{\sigma}{\gamma} \tag{2.3}$$

The shear modulus and the shear stress have the same units (Pa). Each sub-parcel of the material that undergoes shear will exhibit the same local stress and strain, assuming uniform material deformation. Sterss $\sigma_{ij}$ and strain $\gamma_{kj}$ are 2nd rank tnesors, and stifness ($C_{ijkl}$) is a 4th rank tensor relating them ($\sigma_{ij} = C_{ijkl}\gamma_{kj}$) [50]. Since the strain and stress tensors are symmetric, and the trace of any tensor is independent of basis, the most complete coordinate-free decomposition of the strain tensor is to represent it as the sum of a constant tensor and a traceless symmetric tensor as:

$$\gamma_{kj} = \frac{1}{3}\gamma_{kk}\delta_{ij} + (\gamma_{ij} - \frac{1}{3}\gamma_{kk}\delta_{ij}) \tag{2.4}$$

The first term on the right is known as the volumetric strain tensor; it corresponds to deformations due to hydrostatic compression. The second term, known as the deviatoric strain tensor, or shear tensor, is traceless, corresponding to a volume-conserving shear deformation. Any arbitrary deformation can be captured by a linear combination of these two elementary deformations, and thus a generalized Hookes Law for isotropic materials is [50]:

$$\sigma_{ij} = 3K(\frac{1}{3}\gamma_{kk}\delta_{ij} + (\gamma_{ij}) + 2G(\gamma ij - \frac{1}{3}\gamma_{kk}\delta_{ij}) \tag{2.5}$$

Here K is known as the bulk modulus, and G is known as the shear modulus. Written in this way, it is clear that $K$ and $G$ are elements of the stiffness tensor $C_{ijkl}$ for isotropic materials. If the material is purely liquid the shear stress is independent of strain, the shear stress depends linearly on the shear rate $\dot{\gamma}$. The constant of proportionality, know as viscosity is defined as:

$$\eta \equiv \frac{\sigma}{\dot{\gamma}} \tag{2.6}$$

Viscosity has units of force per unit area time (Pa·s in SI units). Fluids for which 2.6 holds are known as Newtonian fluids. Note that for such fluids, the resistance to deformation (shear stress) depends on the rate of deformation and not the amplitude of the deformation, as for solids.

Most of soft matter exhibits viscoelastic properties, having time-dependent mechanical responses intermediate between Newtonian fluids and Hookean solids. A time-dependent generalized shear relaxation function $G(t) \equiv \sigma(t)/\gamma$ is required to describe such behavior. Depending on the material, the response of $G(t)$ will be different. For instance, a Hookean solid the stress will be $\gamma G$ for as long as the stress is applied and then it will shortly return to zero once the stress is released. In Newtonian liquids the stress will exhibit an initial transient spike and then decay rapidly to zero. For pure viscous liquids, the stress will decay exponentially with a characteristic relaxation time ($\lambda_{\text{eff}}$). In order to understand the rheological behavior of viscoelastic materials, mechanical models of linear

viscoelastic response have been proposed. Mechanical models of viscoelastic materials utilize linear combinations of springs and dashpots to mathematically model elastic and viscous components, respectively. The elastic elements can be modeled as springs with elastic modulus $G'$, and, the viscous modulus can be modeled as dashpots with $G''$ as viscous dissipation.

The simplest mechanical models for viscoelastic behavior are theMaxwell and Voigt models. The Maxwell model idealizes the viscoelastic material as a spring in series with a dashpot. The Maxwell model captures the essential features of the rheology of an entangled polymeric network. In such an entangled polymer network, stresses in the network can relax at long times, whereas for short times, entanglements between polymer strands prevent relaxation and give rise to a dominantly elastic rheological response. Accordingly, such networks possess a relaxation time scale, below which the response is dominantly elastic $G'$ and above which the response is dominantly viscous $G''$.

Under imposed total strains $\gamma = \gamma_{elastic} + \gamma_{viscous}$, the strain across the elastic spring and the stress across the viscous dashpot will adjust until stress on both elements is the same as:

$$\sigma = G\gamma_{elastic} = \eta \frac{d\gamma_{viscous}}{dt} \tag{2.7}$$

Hence, in the Maxwell model the stress relaxation modulus is defined by:

$$G(t) \equiv \frac{\sigma(t)}{\gamma_0} = Ge^{\frac{-t}{\tau}} \tag{2.8}$$

Thus, the most important features of the Maxwellian model are:

- The modulus is independent of strain in the linear regime
- A single relaxation time governs the stress relaxation

$$\sigma(t) = \dot{\gamma} \int_0^\infty G(\tau) d\tau \tag{2.9}$$

Dynamic viscoelasticity measurements are made by applying a sinusoidally oscillating strain (or stress) to a sample and measuring its stress (or strain) response, respectively,

as a function of frequency (see figure 2.2). For linear viscoelastic materials, the result is two sinusoidal functions, and both the elastic and dissipative properties of the material are computed from the amplitudes and phase shifts of the sinusoidal functions. In strain-controlled oscillatory measurements, for example, the applied strain varies sinusoidally with time:

$$\gamma(t) = \gamma_0 sin(\omega t) \tag{2.10}$$

Viscoelastic materials can be characterized as having a stress which is out of phase with the strain by a relative phase angle $0 \leq \delta \leq \pi/2$:

$$\sigma(t) = \sigma_0 sin(\omega t + \delta) \tag{2.11}$$

with the consequence that the stress and strain are related by the general expression:

$$\sigma(t) = \gamma_0[G'(\omega)sin(\omega t) + G''(\omega)cos(\omega t)] \tag{2.12}$$

where $G'(\omega)$ is known as storage modulus and $G''(\omega)$ is known as the loss modulus. By expanding 2.12 $G'(\omega)$ and $G''(\omega)$ can be expressed as:

$$\begin{aligned} G' &= \frac{\sigma_0}{\gamma_0} cos(\delta), \\ G'' &= \frac{\sigma_0}{\gamma_0} sin(\delta), \\ tan(\delta) &= \frac{G''}{G'} \end{aligned} \tag{2.13}$$

Equivalently, and more succinctly, the sentiment of 2.13 can be mathematically expressed using the complex function:

$$\begin{aligned} G^*(\omega) &= G'(\omega) + iG''(\omega), \\ tan\delta(\omega) &= \frac{G''(\omega)}{G'(\omega)} \end{aligned} \tag{2.14}$$

The complex shear modulus characterizes the overall resistance to deformation of a material, regardless of whether that deformation is recoverable (elastic $G'$) or non-recoverable

(viscous $G''$). The information contained in the complex shear modulus can alternatively be expressed in terms of the complex dynamic viscosity $\eta^*(\omega)$ that can be related via $G^*(\omega) = -i\omega\eta^*(\omega)$.

### *2.2.2 Microrheology*

Microrheology is a technique designed to study flow and deformation of very small volumes of soft matter materials, complex fluids and non-Newtonian fluids at micro scales [51]. Complex fluids (e.g. wormlike micelles) generally present intermediate behavior between solids (purely elastic) and fluids (completely viscous) see figure 2.2. In microrheology studies complex fluids are embedded with tracer particles. The displacement and motion of those particles is related to thermal fluctuations or forced exitations in order to extract the rheology parameters (see figure 2.3). Mason and Weitz in 1995 showed that the thermal fluctuations of well-defined tracer probes are directly related to the local time dependent frictional drag or resistance and thus to the linear viscoelastic properties of the complex fluid [51–55]. More specifically, Weitz *et al.* used diffusive wave spectroscopy (DWS) measured the mean square displacement (MSD) of fluctuating spherical colloids in some complex fluids. [53] Weitz related the MSD to the generalized Stokes-Einstein relation (GSER). The GSER is defined by the Stokes and Einstein components respectively. The Stokes component relates the mobility of the probe to the rheological properties of the material (complex shear modulus). Complex shear modulus is defined as the frequency dependent ratio between oscillatory stress and strain. The stress and strain form the real storage component ($G'$) and the imaginary loss component ($G''$) respectively. The Einstein component relates the thermal fluctuations of a probe to its mechanical mobility.

In thermal equilibrium, collisions of the particle with the molecules in the fluid gives rise to Brownian motion which can be quantified by the particles mean square displacement (MSD):

$$\langle \delta x^2(\tau) \rangle = \langle [x(t_0 + \tau) - x(t_0)]^2 \rangle \tag{2.15}$$

where $x(t)$ denotes the position of the tracer particle at time $t$, $\tau$ is the lag time, and

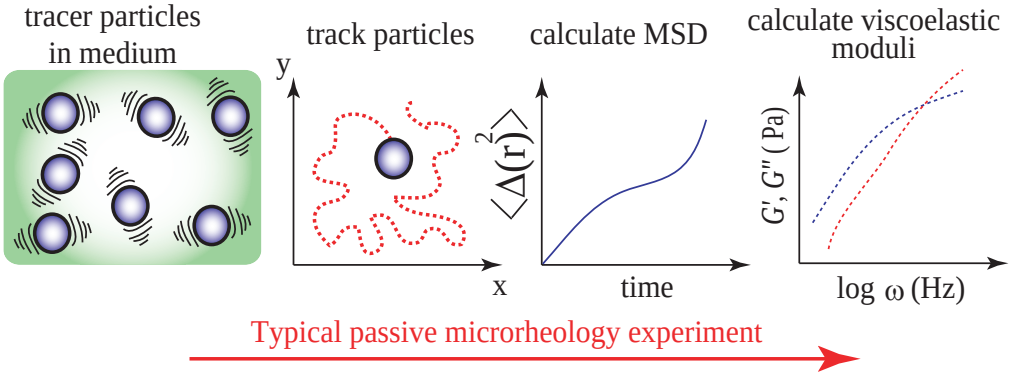


Figure 2.3: Schematic of the workflow of a typical particle tracking microrheology experiment

$\langle\rangle$ denotes time averaging over all initial times $t_0$. For spherical particles with radius $a$ difussing in Newtonian liquid of viscosity $\eta$, the particles MSD is related to the diffusivity $D$ via $\langle \delta x^2(\tau) \rangle = 2D\tau$, where $D = k_B T/(6\pi\eta a)$. Equation 2.15 is known as the Stokes-Einstein relation and is the theoretical cornerstone of all passive microrheology measurements. It asserts that measurements of a particles thermally excited diffusivity can be used to extract the viscosity of the fluid, thus relating an embedded tracer particles dynamics with the mediums rheology.

The Stokes-Einstein relationship has two main contributions: The Einsten part ($D$) that relates the temperature to the mobility of the tracer particles as $D = K_B T M$, where $M = 1/6\pi\eta a$. $M$ is called the particle mobility. $M$ is a deterministic material property that relates the velocity ($v$) of a particle embedded in the medium to the force ($F$) applied to it via $v = MF$.

The first assumption in the generalization of the Stokes mobility is that it adopts the same functional form at all frequencies:

$$M^*(\omega) = \frac{\eta_0}{\eta^*(\omega)} M = (6\pi\eta^*(\omega)a)^{-1} \tag{2.16}$$

Mason and Weitz [52,53], derived the relationship between the probe MSD and frequency-dependent

mobility starting from the Langevin equation:

$$m\dot{V}(t) = f_R(t) - \int_0^t \zeta(t-t')V(t')dt' \tag{2.17}$$

describing the dynamics of a spherical particle subject to a weak random force $f_R(t)$ in an isotropic linear viscoelastic material. Here m and $V$ are the mass and velocity of the probe particle, respectively. $\zeta(t-t')$ is the time-dependent hydrodynamic resistance, defined via

$$F_H(t) = \int_{-\infty}^t \zeta(t-t')V(t-t')dt' \tag{2.18}$$

whose Laplace transform yields

$$\tilde{V}(s) = \frac{mV(0) + f_R(s)}{ms + \tilde{\zeta}(s)} \tag{2.19}$$

where $\tilde{V}(s)$ denotes the Laplace transform of V(t) and $s$ is the Laplace frequency. After some mathematical manipulation (see process in [53]), the resulting expression of the Generalized Stokes-Einstein Relation (GSER):

$$\langle \Delta\tilde{r}^2(s) \rangle = \frac{k_B T}{3\pi\ as\tilde{G}(s)} \tag{2.20}$$

The GSER is the basis for all passive microrheology. It states that the Laplace transform of the probes MSD is related to the Laplace transform of the shear modulus of the medium. An equivalent representation of equation 2.20 in terms of the Fourier components, morevcommonly encountered in oscillatory macrorheological data, can be readily obtained via analytic continuation $s = i\omega$.

One point microrheology use equation 2.20 to obtain the localized rheological properties of single tracer particles. One point microrheology depends on the particle size and material pore size. Hence it is more probable to overestimate or underestimate rheological properties of soft matter. The two-dimensional mean-square displacement (MSD = $\langle \Delta r^2(t) \rangle$) of the embedded microbeads in the FISPs was calculated and plotted. Some light smoothing using a moving average filter (windows size of 99 frames) was performed on the MSD data prior to further analysis. The MSD was then related to the complex modulus $G^*(\omega)$ of the FISPs,

with $\omega$ the frequency. The complex modulus comes from the Stokes–Einstein relation, which shows that the shear-stress relaxation in the locality of the particle is identical to that of the bulk fluid subjected to a shear strain [52]. This approach is valid when the length scale of the heterogeneity of the sample is much smaller than the probe particle size, which can be verified by TEM images of the FISPs. The complex modulus is defined as $G^*(\omega) = G'(\omega) + iG''(\omega)$, where $G'(\omega)$ is the elastic modulus and $G''(\omega)$ is the viscous modulus. Following Mason [52],

$$|G^*(\omega)| \approx \frac{2k_BT}{3\pi a\langle\Delta r^2(\frac{1}{\omega})\rangle\Gamma(1+\alpha(\omega))}, \tag{2.21}$$

where $k_B$ is the Boltzmann constant, $T$ is the absolute temperature, $a$ is the radius of the probe particle, $\Gamma$ is the Gamma function, and

$$\alpha(\omega) = \frac{d(\ln(\Delta r^2(\omega^{-1}))}{d(\ln(\omega^{-1}))} \tag{2.22}$$

is the logarithmic slope of the MSD. For Maxwellian fluids,

$$G'(\omega) = \frac{G_0\omega^2\lambda_{\text{eff}}^2}{1+\omega^2\lambda_{\text{eff}}^2}, \tag{2.23}$$

$$G''(\omega) = \frac{G_0\omega\lambda_{\text{eff}}}{1+\omega^2\lambda_{\text{eff}}^2}. \tag{2.24}$$

Two-point microrheology takes advantage of the interparticle coupling to robustly extract bulk material properties in the face of these potentially confounding influences. Two-point microrheology is based on cross-correlating the equal-time displacements of pairs of tracers [54,55]. Ensemble and time averaging such products over all trajectory pairs yields a mobility correlation tensor, $D_{\alpha\beta}$, that reports the degree of correlation between the tracers random motion during lag time $\tau$ versus their separation $R$:

$$D_{\alpha\beta}(r,\tau) = \langle\Delta_\alpha^i(t,\tau)\Delta_\beta^j(t,\tau)\delta[r-R^{ij}(t)]\rangle_{i\neq j,t} \tag{2.25}$$

where $i$ and $j$ denote different particles, $\alpha$ and $\beta$ denote different coordinates, and $R_{ij}$ is the distance between the distinct particles $i$ and $j$. Spatially, $D(r,\tau)$, can be decomposed into a longitudinal $D_{rr}$ and transverse $D_\perp$ components, where the former is the component

of the motion along the center-to-center separation vector of the two tracers, while the latter two are the components orthogonal to the separation vector (see figure 2.4). For an incompressible medium, the amplitudes are related via $D_{\perp} = 1/2D_{rr}$. Typically, $D_{rr}$ is the strongest component and hence easiest to measure in experiments from a signal-to-noise perspective. Moreover, to lowest order in $a/R$, $D_{rr}$ depends only on the shear modulus of the medium (see figure 2.5) [54]. Accordingly, the shear modulus may be determined using the relation

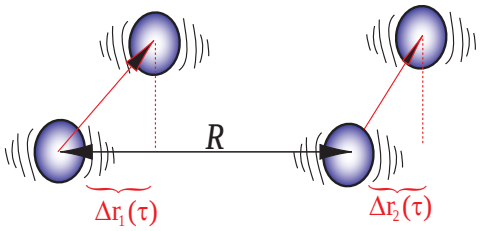


Figure 2.4: Schematic of two-point displacement component. The longitudinal component $D_{rr}$= $\langle \Delta r_1(\tau) \Delta r_2(\tau) \rangle$ is the product of the displacement component projected along the line separating the tracers by distance $R$, with $R \gg a$ ideally.

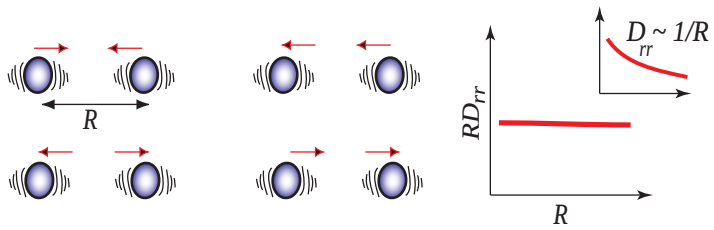


Figure 2.5: Motion of the tracer particles along $D_{rr}$ component.

$$\tilde{D}_{rr}(R,s) = \frac{k_B T}{2\pi R s \tilde{G}(s)} \tag{2.26}$$

where $D_{rr}(R,s)$, is the temporal Laplace transform of $D_{rr}(R,\tau)$. Significantly, equation 2.26 has no explicit dependence on the radius of the particle, suggesting that it is independent of the tracers size, shape and boundary conditions with the medium in the limit

$R >> a$. This is the signal advantage of two-point measurements that has enabled it to surmount the inhomogeneity issue that limited blind application of the GSER in microrheology. Equation 2.26 can be written as

$$\langle \Delta \tilde{r}^2(s) \rangle = \frac{2R}{a} D_{rr}(R, s) \tag{2.27}$$

The complex modulus ($G^*(\omega)$) can be obtained by Fourier transform $\tilde{G}$(s) such as [**?**, **?**]:

$$\tilde{G}(s) = |G^*(\omega)| \approx \frac{2k_B T}{3\pi a \langle \triangle r^2(\frac{1}{\omega}) \rangle \Gamma(1 + \alpha(\omega))}, \tag{2.28}$$

$$\alpha(\omega) = \frac{d(ln(\triangle r^2(\omega^{-1})}{d(ln(\omega^{-1}))}, \tag{2.29}$$

Two point passive microrheology process approximates $\langle \triangle r^2(\tau) \rangle$ locally by a second order polynomial in the logarithmic scale to extract $G^*(\omega)$ [54]. Hence, this process has the advantage that it does not require the experimental data to be fit to an analytical model, nor does it suffer from truncation errors of numerical integrations.

In summary, one point and two point passive microrheology can be described as:

- The viscous forces of the surrounding medium dominate the dynamics of the probe particle
- Buoyancy of the probe particle might affect the microrheology measurements. However passive microrheology can be applied if the probe particle has low rates of sedimentation. Using a purely viscous fluid the rate of sedimentation is given by

$$v_{sed} = \frac{2a^2 mg}{9V\eta} \tag{2.30}$$

The previous equation assumes non-interacting single particle in a purely viscous fluid, where $a$ is the radius of the probe particle, $g$ the gravity, $m$ the mass of the probe particle (adjusted to the buoyancy) $V$ the volume of the particle and $\eta$ the viscosity of the fluid.

- Diffusion of the particle in a purely viscous fluid allows the amplitude of the particle fluctuations to be measured. Diffusion coefficient D is related to the frictional coefficient of the particle and the thermal energy, thus Einstein-Stokes relation can be formed by:

$$D = \frac{k_B T}{f}$$
$$f = 6\pi\eta r \tag{2.31}$$

- Homogeneity, if the material has a non-uniform structure (like porous material) the particle probe has to be bigger than the size of the homogeneities. Otherwise the continuum assumption breakdowns and the ESR cannot be applied

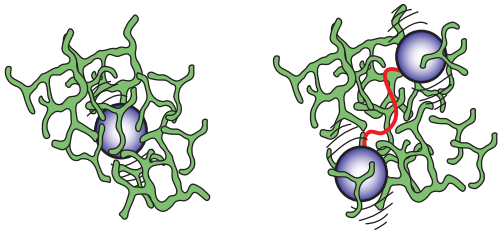

Figure 2.6: One point and two point microrheology techniques

We performed passive microrheology on the precursors and their corresponding FISPs [51, 52]. Due to the small volumes of the FISPs produced in the microdevice (∼80 $\mu$L), rheological properties of the FIPSs were measured by one point and two point passive microrheology. To facilitate these measurements, the precursor solution was seeded with 1 $\mu$m diameter polystyrene microspheres, with 0.01 wt% in the total solution. The experiments were conducted on an inverted Leica microscope at 23±2 °C. Harvard Apparatus digital pumps were used to pump the precursor through the device at a constant flow rate (15 mL/h). Once the precursor passed through the micropost arrays the FISPs began to emerge. We performed all experiments under room temperature (23±2 °C) and were able to produce FISPs with very similar microstructures.

### *2.2.3 Approximation of the strain rate in the micropost*

Two estimates of the rate of strain experienced by a fluid element as it passes through the microfluidic device were approximated. The hexagonal array of microposts was considered to be a packed bed with a void fraction of $\phi$. The empty channel average velocity (i.e., in the absence of the micropost array) is $\hat{Q}/(\hat{W}\hat{H})$, where $\hat{Q}$ is the flow rate, $\hat{W}$ is the channel width, and $\hat{H}$ is the channel height. Thus, the average velocity through the micropost array is $\hat{U}_{\text{avg}} = \hat{Q}/(\phi\hat{W}\hat{H})$.

The first estimate of the magnitude of the rate of strain comes from considering an energy balance between the pressure required to drive the flow and the viscous dissipation of the flow. Inertial effects are considered negligible and are ignored. In the hexagonal array an estimate of the viscous dissipation (per unit volume) is given by

$$\hat{E}_{\text{visc}} \approx \hat{\mu}\hat{\dot{\gamma}}^2, \tag{2.32}$$

where $\hat{\mu}$ is the viscosity. The rate of energy input into the system (from the pressure differential, per unit volume) is

$$\hat{E}_{\text{pres}} \approx \frac{\Delta\hat{p}}{\hat{L}}\hat{U}_{\text{avg}}, \tag{2.33}$$

where $\Delta\hat{p}$ is the magnitude of the pressure difference across the array and $\hat{L}$ is the length of the array. Furthermore, using the Kozeny-Carman equation [69] the pressure gradient can be written as

$$\frac{\Delta\hat{p}}{\hat{L}} = \frac{150\mu\hat{U}_{\text{avg}}}{\hat{D}^2}\frac{(1-\phi)^2}{\phi^2}, \tag{2.34}$$

where $\hat{D}$ is the diameter of the microposts. Thus, equating (2.32) and (2.33) we obtain the following estimate for the magnitude of the rate of strain:

$$\hat{\dot{\gamma}} \approx \sqrt{150}\frac{\hat{Q}}{\hat{D}\hat{W}\hat{H}}\frac{1-\phi}{\phi^2}. \tag{2.35}$$

An alternate estimate can be obtained by considering the rate of strain experienced by a fluid element as it enters the micropost array [69]. The empty channel velocity is $\phi\hat{U}_{\text{avg}}$, and as the fluid element enters the array its velocity must increase to $\phi\hat{U}_{\text{avg}}(\hat{D}+\hat{d})/\hat{d}$ over a distance of roughly $\hat{D}$, where $\hat{d}$ is the spacing between the microposts. Thus the extensional

strain resulting from this acceleration is

$$\hat{\dot{\gamma}}_{\text{ext}} \approx \frac{1}{\hat{D}}\left(\phi\hat{U}_{\text{avg}}\frac{\hat{D}+\hat{d}}{\hat{d}} - \phi\hat{U}_{\text{avg}}\right) = \frac{\phi\hat{U}_{\text{avg}}}{\hat{d}} = \frac{\hat{Q}}{\hat{d}\hat{W}\hat{H}}. \tag{2.36}$$

Furthermore, if we approximate the flow through the gaps between the microposts as a 2D Poiseuille flow, the maximum velocity between two posts is $3\phi\hat{U}_{\text{avg}}(\hat{D}+\hat{d})/(2\hat{d})$. Thus an estimate of the strain due to shear is

$$\hat{\dot{\gamma}}_{\text{sh}} \approx \frac{3\phi\hat{U}_{\text{avg}}}{2\hat{d}}\frac{\hat{D}+\hat{d}}{\hat{d}} = \frac{3\hat{Q}}{2\hat{d}\hat{W}\hat{H}}\frac{\hat{D}+\hat{d}}{\hat{d}}. \tag{2.37}$$

Adding the above two expressions we have

$$\hat{\dot{\gamma}}_{\text{total}} \approx \frac{\hat{Q}}{\hat{d}\hat{W}\hat{H}}\left(\frac{5}{2} + \frac{3\hat{D}}{2\hat{d}}\right). \tag{2.38}$$

The microchannel has a height of $\sim 75$ $\mu$m and a width of $\sim$1260 $\mu$m. The total length of the fluid element traveling through the micropost array is $\sim 1.2$ cm, and the microposts are $\sim 100$ $\mu$m in diameter with the micropost spacing of $\sim$15 $\mu$m, with the void fraction $\phi = 0.21$. So for a flow rate of 15 mL/h, equation (2.35) gives $\hat{\dot{\gamma}} \approx 9.7\times10^4\,\text{s}^{-1}$ and equation (2.38) gives $\hat{\dot{\gamma}}_{\text{total}} \approx 3.7\times10^4\,\text{s}^{-1}$. These two numbers show the same order of magnitude but approach 2 might be more accurate. Hence, we choose $\hat{\dot{\gamma}}_{\text{total}} \approx 3.7\times10^4\,\text{s}^{-1}$ in our paper. The average velocity can be calculated as $\hat{U}_{\text{avg}} = 0.21$ m/s, while the average residence time of a fluid element is $\hat{L}/\hat{U}_{\text{avg}} \approx 0.057$ s. Hence the total strain is estimated as $\hat{\gamma} \approx 2114$.

### *2.2.4 Small-angle neutron scattering SANS*

SANS is a powerful measurement because unlike microscopy, scattering is a non-destructive, bulk measurement that can probe a large size and temporal scale simultaneously. In this way, the native conformation of materials under investigation can be interrogated and the fitting results represent the average characteristics of the sample [57–60]. Small-angle neutron scattering (SANS) technique allows the investigation of length scales on the colloidal nano-scale, hence this technique is suitable for micellar solutions. SANS allows investigation of length scales on the order of 1-1000 Å(see figure 2.7). The length scales are accessible through the scattering vector $q$:

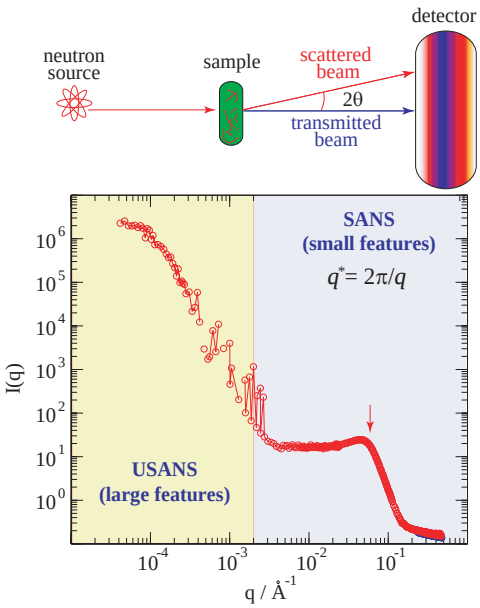


Figure 2.7: At low $q$ large domains can be extracted from SANS/USANS data, whereas, at high $q$ small features of the sample can be approximated

$$q = \frac{4\pi}{\lambda} sin(\frac{\theta}{2}) \tag{2.39}$$

where $\lambda$ is the neutron wavelength and $\theta$ is the scattering angle. The absolute scattering intensity, $I(q)$, depends on the shape and size of micelles in solution, as well as micellar interactions. For monodisperse particles, homogeneous scattering $I(q)$ has to following the form:

$$I(q) = NP(q)S(q) \tag{2.40}$$

The form factor $P(q)$, provides information on the size and shape of the particle, whereas interparticle interaction are represented by the structure factor, $S(q)$.

Extracting information from scattering spectra can be accomplished by fitting methods, where the assumption of form factors and structure factors are done [57, 58, 60]. Fitting process requires some a priori information of the type of the structure present so that the appropriate form and structure factors are selected. There are exact representations of the

form factor, $P(q)$ for simple geometries (e.g., spheres, cylinders), however no exact solution is available for flexible wormlike micelles interacting within themselves. In the dilute limit ($S(q) = 1$), a Guinier approximation to the form factor can be made to obtain structural information. For cylinder with length $L$ larger that its cross-sectional area $A$, the form factor can be approximated as [57]:

$$P(q,\alpha) = \frac{scale}{V} f^2(q) + background$$
$$f(q) = 2(\Delta\rho)Vsin(qLcos(\alpha/2))/(qLcos(\alpha/2))\frac{J_1(qrsin(\alpha))}{qrsin(\alpha)} \tag{2.41}$$

where $\alpha$ is the angle between the axis of the cylinder and $q$, $V$ is the volume of the cylinder, $r$ is the radius of the cylinder, of the cylinder, and $\Delta\rho$ (contrast) is the scattering length density difference between the scatterer and the solvent. $J_1$ is the first order Bessel function.

Spherical micelles can be simulated by using sphere model. This model provides the form factor, $P(q)$, for a monodisperse spherical particle with uniform scattering length density. The form factor is normalized by the particle volume as described below [57]:

$$P(q) = \frac{scale}{V}[\frac{3V\Delta\rho[sin(qr) - qrcos(qr)]}{(qr)^3}]^2 + background \tag{2.42}$$

where scale is a scale factor, volume fraction $V$ is the volume of the scatterer, $r$ is the radius of the sphere, the background level .

When a solution contains sharp interfaces between regions of different scattering length intensity, the scattering intensity at high-$q$ asymptotically reaches:

$$I(q) = \frac{K_p}{q^4} + B \tag{2.43}$$

where $K_p$ is the Porod constant and $B$ is the incoherent background. The Porod constant is related to the surface to volume ($S/V$) ratio, hence structural information can be obtained at high-$q$ without need for assumptions or models. For micellar the sharp interface occurs from the cross-section.

Some micelles exhibit core-shell structures, hence the use of a core-shell model to obtain the structural parameters of such micelles. Core-shell model provides the form factor, $P(q)$,

for a spherical particle with a core-shell structure. The form factor is normalized by the particle volume as [57]:

$$P(q) = \frac{scale}{V_s}[3V_c(\rho_c - \rho_s)\frac{sin(qr_c) - qr_c cos(qr_c)}{(qr_c)^3} + 3V_s(\rho_s - \rho_{solvent})\frac{sin(qr_s) - qrcos(qr_s)}{(qr_s)^3}]^2 \tag{2.44}$$

where scale is a scale factor, $V_s$ is the volume of the outer shell, $V_c$ is the volume of the core, $r_s$ is the radius of the shell, $r_c$ is the radius of the core, $\rho_c$ is the scattering length density of the core, $\rho_s$ is the scattering length density of the shell, and $\rho_{solvent}$ is the scattering length density of the solvent.

The microstructure of fibril-like wormlike micelles can be approximated by using a fractal model. The fractal models approximates the scattering from fractal-like aggregates built from spherical building blocks following the Texiera model [57, 58] as [57]:

$$\begin{aligned} I(q) &= P(q)S(q) + background \\ P(q) &= scale \times V(\rho_{block} - \rho_{solvent})^2 F(q_0 R_0)^2 \\ F(x) &= \frac{3[sin(x) - xcos(x)]}{x^3} \\ V &= \frac{4}{3}\pi R_0^3 \\ S(q) &= 1 + \frac{D_f \Gamma(D_f - 1) sin[(D_f - 1)tan^{-1}(q\chi)}{[1 + 1/(q\chi)^2]^{(D_f - 1)/2}(q_0 R_0)^{D_f}} \end{aligned} \tag{2.45}$$

The scale parameter is the volume fraction of the building blocks, $R_0$ is the radius of the building block, $D_f$ is the fractal dimension, $\chi$ is the correlation length, $\rho_{solvent}$ is the scattering length density of the solvent, and $\rho_{block}$ is the scattering length density of the building blocks.

In the absence of significant micellar interactions, the flexibility of the micelles can be approximated by using a Holtzer plot. The $q^{-1}$ dependence characteristic of the persistence length $l_p$ in flexible macromolecules is highlighted in a $q \cdot I(q) vs\, q$ plot, referred to as Holtzer or bending plot. When the type of microstructure presented in the media is unknown, some indirects methods can be applied. For instead, the separation of inter and intra-particle effects from scattering data can be performed by using generalized indirect Fourier

transforms (GIFT) method. In GIFT method a structure factor is considered for interacting systems.

The GIFT method transforms the scattering spectra into real-space in the form of pair-distance distribution function, $p(r)$. The pair-distance distribution function (PDDF) is related to the particle form factor by [57]:

$$P(q) = 4\pi \int_0^\infty p(r) \frac{sin(qr)}{(qr)} dr \tag{2.46}$$

The GIFT method approximates $p(r)$ by a linear combination for cubic B-splines $\phi_v(r)$ as

$$p(r) = \sum_{v=l}^{n} c_v \phi_v(r) \tag{2.47}$$

and requires no other parameters other than the maximum dimension of the particle. The expansion coefficient $c_v$, are only the unknown parameters. Hence, in the absence of interparticle interactions, the approach provides a model-free determination of the shape and size of the particle. Spherical particles exhibits a symmetric PDDF with a maximum dimension diameter at $p(r) = 0$. Cylindrical particle exhibits similar maximum value, however, beyond the maximum an inflection point is observed followed by linear decay. The inflection point defines the cylinder diameter, and the length is given by the point at which $p(r) = 0$. Further, The GIFT method also accounts for particle interactions ($S(q)$) as:

$$I(q) = P(q)S(q,d) = 4\pi S(q,d) \int_0^\infty p(r) \frac{sin(qr)}{qr} dr \tag{2.48}$$

Where $d$ is the set of parameters that specifies the structure factor, which must determined simultaneously with $p(r)$. The structure factor is related to the total correlation function, $h(r)$:

$$S(q) = 1 + 4\pi n \int_0^\infty h(r) r^2 \frac{sin(qr)}{(qr)} dr \tag{2.49}$$

where $n$ is the particle density. The total correlation function is determined by the radial distribution function $g(r)$, as $g(r) = h(r) + 1$.

Small-angle neutron scattering (SANS) and ultra small angle neutron scattering (USANS) measurements were performed on the same samples at the National Institute of Standards and Technology (NIST) Center for Neutron Research (NCNR) in Gaithersburg, Maryland. SANS was performed using a standard configuration to cover a wide range of wave vector values. In addition, ultra-small angle neutron scattering (USANS) measurements were performed by using a perfect crystal diffractometer BT5 at the NCNR [60]. USANS increases the scattering range, so that sub-micron and micron sized features of the FISP could also be probed. The samples were tested at different temperatures 25 °C, 30 °C, 45 °C and 60 °C. Analysis and model fitting was performed using the DANSE SansView software [57]. Note that only smeared data was fitted, and the models were modified to account for the line-collimation of the system using the tools available in the software package. Both precursor and FISP were prepared by volume in deuterated water containing 99.9% $D_2O$ (Cambridge Isotope Laboratories, Andover, MA). The scattering contrast was determined from the scattering length density (SLD) of the deuterated solvent ($6.39\times10^{-6}$ Å$^{-2}$) and the precursor ($-1.54\times10^{-7}$ Å$^{-2}$) by using SANSview tool bar [57, 58].

### *2.2.5 Electron Microscopy*

TEM samples were imaged by the Tecnai G2 F20 transmission electron microscope (FEI Co., Hillsboro, OR) at 200 kV and equipped with a field emission gun. Images were recorded under low dose conditions at a magnification of 50,000 and a pixel size of 2.2 Å on a 4k CCD camera (4k Eagle Camera, FEI). The freeze-plunging method was used for the cryo-sample preparation. Approximately 5 $\mu$L of the sample was applied on Quanti-foil R-2/2 grids (Electron Microscopy Sciences, Hatfield, PA). The sample was allowed to adhere to the grids for 30 s before being blotted on a filter paper to remove excess solution. The sample was then immediately plunge frozen by immersing into a reservoir with liquid ethane cooled by liquid nitrogen. The grids with the frozen sample were transferred under liquid nitrogen to the Gatan 626 cryo-holder (Gatan, Inc., Pleasanton, CA), using the cryo-transfer station. After inserting the cryo-holder to the transmission electron microscope, the temperature was maintained below $\sim -178$ °C at all times during the cryo-imaging.

### *2.2.6 UV-Visible Spectroscopy*

A Varian Cary 5000 UV-Vis-NIR Spectrophotometer coupled with a temperature controller at 25 °C. A wave spectrum scan from 200 nm to 800 nm was performed to identify the resonance peaks of the solutions analyzed in the present work.

# Chapter 3

# FORMATION OF FISP BY USING NASAL/CTAB MICELLAR SOLUTION

## *3.1 Effect of salt on ionic branched wormlike micelles*

For semi-dilute wormlike micellar solutions made with ionic surfactants, the addition of salt can lead to significant structural and rheological transitions [6]. Multi-connected and branched micellar networks have been observed at equilibrium. Porte *et al.* [6] reported the formation of branched and multi-connected wormlike micellar network in ionic micellar solutions with high salt concentrations (CPyCl/hexanol with [NaCl=0.2 M]). They proposed that multi-connections in the network can slide against each other, yielding high fluidity. Candau *et al.* performed rheological measurements of wormlike micellar solutions of [CTAB] = 0.35 M and found the zero-shear viscosity and stress relaxation time to reach a maximum, followed by a reduction with increasing salt concentrations ([KBr= 0.1-2 M]) [9]. This behavior is related to the transition from entangled linear micelles to multi-connected structures with salt addition [9]. Similar trends in the zero-shear viscosity and stress relaxation time with changes to salt concentration were observed in a semi-dilute wormlike micellar solution with [CTAB = 0.3 M] and [$NaNO_3$= 0.0-4.0 M] by Cappelare and Cressely [11]. The plateau modulus $G_0$ was not found to vary much until after the salt concentration reached the level at which the zero-shear viscosity and stress relaxation time peak. They proposed that the branching of the micelles (with sliding connections) or the shortening of the micelles might lead to the reduction of the zero-shear viscosity. Cappelare and Cressely [12] subsequently studied the salt ($NaNO_3$) effect on surfactant CPCl and showed that plateau modulus decreases with increasing salt content. One possible mechanism is that the micellar network junctions might break at higher salt concentration, leading to shorter micellar length and, hence, a drop in the plateau modulus. Schubert *et al.* [16] used rheology, flow birefringence and SANS to quantify important micellar length scales of a wormlike micellar solution of CTAT/SDBS with the addition of salt. Both the zero-shear

viscosity and stress relaxation time were found to decrease with addition of hydrotropic salt NaTosylate, which is potentially related to the presence of branched micelles.

The organic salt containing salicylate or alkylbenzoate counter-ions can alter the structural and rheological response in a micellar system differently compared to those of inorganic salts. Double peaks of the zero-shear viscosity have been observed with increasing organic salt concentrations. The first peak has usually been attributed to the emergence of a multi-connected wormlike micellar structure in which the cross-link points have the ability to slide and promote higher fluidity in the network. With further salt addition, the micelles can become negatively charged. The effect of Coulomb interactions might reduce the micellar length, increasing the branching density and, hence, lower $\eta_0$. Kadoma and van Egmond [14] and Kadoma *et al.* [15] investigated [CTAB] = 0.03 M and [NaSal] = 0.06–0.24 M system with rheological measurements and SALS patterns under shear. They observed double peaks in both the zero-shear viscosity and the stress relaxation time. Furthermore, the evolution of the scattering patterns was found to be correlated to the multi-connected micellar networks of cross-linked micelles. Oelschlaeger *et al.* [19] studied the wormlike micellar system of [CPyCl] = 0.1 M and [NaSal] = 0.07–0.5 M by using mechanical rheology and optical microrheology to probe the structural and dynamic changes with increasing salt concentration. They also observed double peaks of the zero-shear viscosity with increasing salt concentrations and related the persistence length and cross-link density to the rheological responses of the micellar system.

### *3.2 Flow-induced structures in ionic micellar solutions*

Flow-induced structure (FIS) formation has been reported in solutions of wormlike micelles; however, until now these structures were all temporary and would deteriorate upon cessation of the flow [5]- [25]. These transient structures were first reported by Rehage and Hoffmann [5], who found that a wormlike micellar solution (aqueous solution of the cationic surfactant cetylpyridinium chloride ([CPyCl = 15–100 mM]) and the organic salt sodium salicylate ([NaSal = 11–60 mM]) form a gel-like structure under shear flow above a critical shear rate. They referred to this gel-like structure as *shear-induced structure* **(SIS)** because upon cessation of the flow, the SIS would disintegrate. Pine *et al.* [24, 25] also observed the

appearance of SIS which form "gel-like" fingers in wormlike micellar solutions ([0.1–7]/[0.1–7] mM CTAB/NaSal and 7.5/7.5 mM of TTAA/NaSal) sheared in a Couette cell. The increase in the shear viscosity of the micellar solution was found to coincide with the onset of the SIS formation. In addition, they predicted the existence of wormlike micellar bundles with a diameter of ∼200 nm based on small angle light scattering (SALS) patterns [24]. The relaxation time of the SIS was found to range from several seconds to a couple of hours [25]. Similarly, others observed birefringent SIS formation in a solution of surfactant and salt under shear and subsequent disappearance of the birefringent structures after the flow was stopped [28]. Kadoma and van Egmond [13] showed that CTAB/NaSal (0.03/0.24 M) based SIS consist of highly elongated and locally-concentrated micellar strings from time-dependent SALS studies under a simple shear flow. SIS has since been widely studied using birefringence, light scattering, neutron scattering, x-ray scattering, and nuclear magnetic resonance [4].

Stable flow-induced structures from wormlike micelles were first reported by Vasudevan *et al.* [30]. A semi-dilute [CTAB] = 50 mM/[NaSal] = 16 mM shear-thickening solution formed a stable "gel-like" *flow-induced structured phase* (**FISP**) after traversing a microfluidic tapered channel packed with glass beads (20–100 $\mu$m in diameter). This stable "gel-like" FISP occurred from a combination of high strain rates ($\dot{\epsilon} \sim 5{,}000\ \mathrm{s}^{-1}$) and extensional features of the flow. The FISP remained stable for more than a year at room temperature, even after the cessation of flow. Using the same wormlike micellar solution, Dubash *et al.* [47] formed the FISP using micropost arrays with a 7 $\mu$m gap size and found the rheological properties of the FISP to be at least one order of magnitude larger than those of the precursor. Cheung *et al.* [48] extended this work by adding Nile Red dye (a fluorescent dye whose intensity is related to the CTAB concentration) to the precursor and tracked the local micellar concentrations during flow. The micropost configuration allows for variations of the local micellar concentration of up to 25%, which were found to be correlated with the FISP formation. Whereas the majority of direct observation of transient flow-induced structures have involved purely shear flows, flows which results in stable structure formation such as FISP includes both shear and extensional flows and the rates of strain are generally several orders of magnitude larger than those in the pure shear flows.

### *3.3 Flow conditions for FISP formation*

Both precursors used are semi-dilute and consist of CTAB and NaSal in an aqueous solution. The shear-thickening (precursor$_{50}$, [CTAB] = 50 mM) and shear thinning (precursor$_{100}$, [CTAB] = 100 mM) solutions have concentration ratio [NaSal]/[CTAB] = 0.32 to maintain proportionality of the electrostatic interaction. The PDMS-glass microfluidic device is a channel height of 75 $\mu$m containing a hexagonal array of microposts with diameter 100 $\mu$m and spacing 15 $\mu$m. The experiments were conducted on an inverted Leica microscope at 23±2°C. Harvard Apparatus digital pumps were used to pump the precursors through the device at a constant flow rate (15 mL/h). Once the precursors passed through the micropost arrays the FISP began to emerge. Fig. 3.1(a,b) shows schematics for the FISP formation. Fig. 3.1(c) shows the actual device with finger-like FISP. Fig. 3.1(d) shows a SEM image of the FISP$_{50}$, exhibiting entangled, branched, and multi-connected networks.

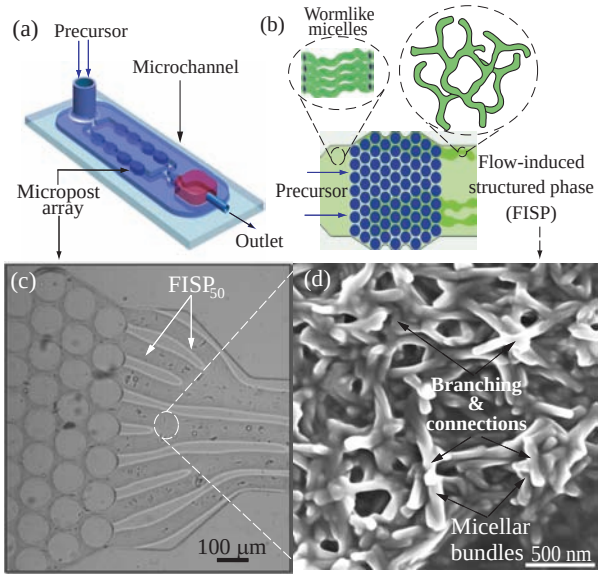


Figure 3.1: (a,b): Schematics of the microdevice. When the precursor passes through the micropost array it undergoes high strain rates of $\sim 4.4\times10^4 s^{-1}$ and total strain $\sim 1.6\times10^3$, leading to the FISP formation. (c): A snapshot showing the "finger-like" FISP formation. (d) A high resolution SEM image of FISP$_{50}$ at a magnification of 50,000× under HV 3.00 kV.

At a flow rate of 15 mL/h, we estimate a maximum rate of strain of $\dot{\gamma}_{\text{total}} \sim 4 \times 10^4\,\text{s}^{-1}$ and a total strain in the arrays of $\gamma_{\text{total}} \sim 1600$. Also, the onset of FISP was found to require a minimum strain rate of $\dot{\gamma}_{\text{total}} \sim 650\,\text{s}^{-1}$ and a total strain of $\sim 10^3$. Even though stable FISP differs from reversible SIS, making quantitive comparisons on the critical strain rates required to form these structures should shed insight on the FISP formation mechanism. To generate reversible SIS with gel-like shear thickening behavior from a CTAB/NaSal micellar solution, the critical shear rate has been reported to be around 10-20 $\text{s}^{-1}$, with [CTAB] = 0.08–7.0 mM and 1:1 salt to surfactant molar ratio [24]. More recently, Takahashi and Sakata [61] applied a step planar elongation flow to wormlike micellar solutions of [CTAB] = 0.03 M and [NaSal] = 0.03–0.27 M and observed both transient SIS and elongation-induced structures (EIS) at extension rates of 0.1–1 $\text{s}^{-1}$ and elongation strains of $\sim 1 - 10$. Moss and Rothstein [62] studied a shear thinning CTAB/NaSal (both 50 mM) solution passing through a periodic array of cylinders with diameter 10 mm and gap size 40 mm, a configuration is three orders of magnitude larger than ours. Elastic instabilities and strain hardening were observed but no FISP was reported.

Modeling wormlike micelles under extensional flow, Turner and Cates [63] predicted a critical extension rate where the solution undergoes a transition to a "gel" phase consisting of extremely long aligned micellar chains. They assumed a simple reaction scheme in which two micelles fuse only if they are collinear. Again, this gel phase only persists while the flow is active. On the basis of their model, for wormlike micelles with length $\sim$80 nm, a critical strain rate of $\sim 10^3$ $\text{s}^{-1}$ is required for extensional flow-induced gelation. This strain rate has the same order of magnitude as the one present in our micropost array ($\dot{\epsilon}_{\text{ext}} \sim 3.5 \times 10^3\,\text{s}^{-1}$) and is similar to our strain-rate threshold for the FISP formation.

The comparisons described above indicate that high extension rates and spatial confinement are critical for FISP formation. We now propose a potential mechanism for the FISP formation (see Fig. 3.2). The high stretching and flow alignment in the micropost array increase the flexibility of the micelles and hence lower the bending modulus of the micelles [64–66]. The free energy of surfactant molecules in the end-cap therefore increases relative to the curvature energy in the cylindrical body of the micelle, lowering the work required to form junctions [7, 8, 16, 17, 67, 69]. As flexible adjacent micelles flow through the

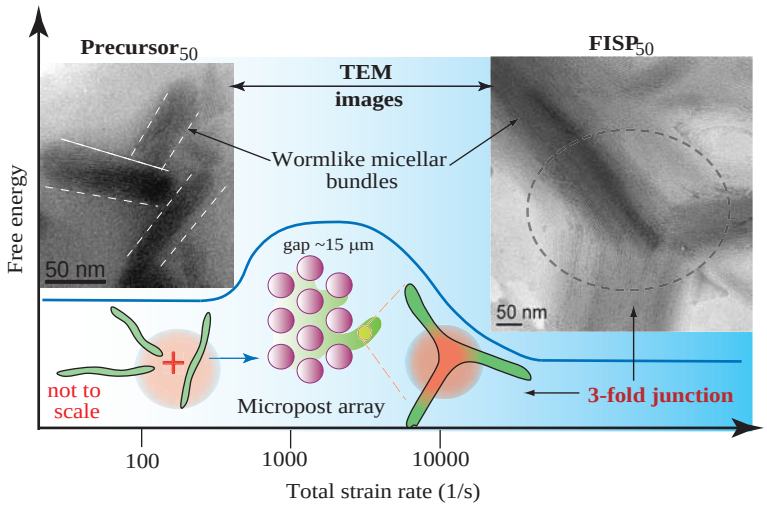


Figure 3.2: The micropost configuration enables the high strain rates and strain in the flow, accompanied by the concentration fluctuations in both CTAB and Sal ions. The free Sal ions in the bulk solution can penetrate to the cores of micelles, making wormlike micelles more flexible. It becomes energetically favorable for a pair of adjacent micelles to merge when they flow through the confined microposts, promoting the formation of junctions and cross-links, leading to entangled, branched and multi-connected FISP.

confined micropost array, it becomes energetically favorable to minimize the number of end caps while promoting the formation of cross-links, yielding highly entangled, branched, and multi-connected wormlike micellar bundles (FISP) [10, 67, 68]. The presence of spatial confinement and high extension in our microfluidic device also induces entropic fluctuations, making it easier to cross the energy barrier between states and, thus, increasing transition frequencies between states, enabling the formation of entangled and branched micellar bundle networks.

### *3.4 Microstructural analysis*

We used a combination of electron-microscopy techniques (Cryo-EM, TEM and SEM) to conduct extensive microstructural characterizations of the precursor solutions and their corresponding FISP. Since the carbon and other light element based makeup in CTAB/NaSal samples has very low electron density, we employed a negative staining procedure with

NanoW© to enhance imaging contrast. Cryo-TEM imaging is desirable because it can capture the true microstructure of a given sample in its native hydrated environment. However, the resolution of cryo-TEM tends to be sacrificed due to the vitreous ice layer within the sample. Taking these factors into consideration, we performed both Cryo-TEM and TEM microscopy of the $FISP_{50}$, shown in Fig. 3.3. From the morphological comparison of frozen but hydrated (image a) and gradually air-dried (image b) samples by cryo-TEM and TEM, we found excellent ultra-structural correlation in both methods. On these grounds, to avoid the decreased resolution caused by imaging through the vitreous ice layer (shown in Fig. 3.3a as a gray background) with cryo-TEM, we proceeded with room temperature TEM imaging. In Fig. 3.3, $FISP_{50}$ consists of branched and entangled electron-dense branches. Since an individual wormlike micelle has a diameter of $\sim 5$ nm and each bundle has a diameter of $\sim 100 \pm 15$ nm and a length of $\sim 350 \pm 45$ nm, each bundle represents $\sim 20$ parallel wormlike micelles. The electron-dense branches represent wormlike micellar bundles and electron-transparent areas are the pores in the microstructure. Both $FISP_{50}$ and $FISP_{100}$ exhibit entangled, branched, and multi-connected bundles with distinct junctions and cross-links shown in Fig. 3.4. The triple junctions shown in (Fig. 3.5) are consistent with those predicted from theoretical and numerical approaches [10, 67, 68].

Fig. 3.4 shows the structural evolution of wormlike micelles from within the precursors to the FISP. Both precursors also exhibit the existence of wormlike micellar bundles with similar diameters (see top row in Fig. 3.4(a, c)). The interspacing between bundles in the $precursor_{50}$ is almost 6 times larger than those in the $precursor_{100}$ (Fig. 3.4(a, c)). Also, the linear micellar bundles are densely entangled in the $precursor_{100}$ (Fig. 3.4(c)). Similarly, Shikata *et al.* [10] observed entangled and elongated wormlike micelles from TEM imaging on a shear-thinning solution of [CTAB] = 0.1 M and [NaSal] = 0.3 M. Li *et al.* [71] performed cryo-TEM microscopy of a shear-thinning solution of [CTAB] = 0.25 M and [NaSal] = 0.15 M and also showed entangled wormlike micelles. Fig. 3.4 also exhibits distinct structural transitions from the precursors to their FISP. $Precursor_{50}$ shows a less entangled, linear bundle structure; while $FISP_{50}$ has highly entangled and branched bundles with open pores. $Precursor_{100}$ shows dense and entangled linear bundles; while $FISP_{100}$ has less entangled and branched porous structure.

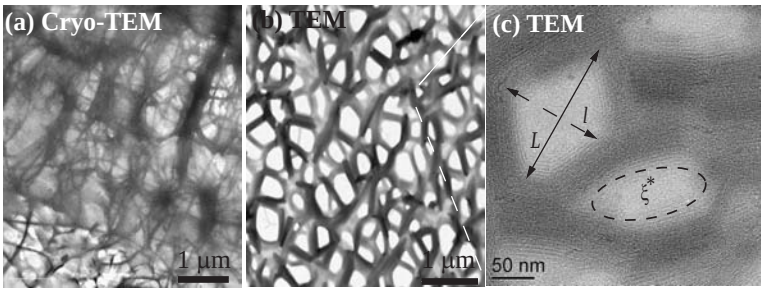


Figure 3.3: (a): Cryo-TEM image of $FISP_{50}$; (b,c): TEM images of the $FISP_{50}$. The electron dense (dark) branches are the wormlike micellar bundles while the bright areas correspond to the pores in the structure. Conducted by TEM model Tecnai T-12. (c) The averaged mesh size $\xi^*$ was determined from the geometric mean $\sqrt{lL}$ of the smallest ($l$) and largest ($L$) distances in the pore.

We can estimate the degree of entanglement of the precursor and FISP samples to quantify their structural transitions [70]. Assuming all samples have flexible Gaussian chains that are entangled or cross-linked, we can approximate the degree of entanglement in these materials as $\nu^* = \xi^{*-3}$, where $\xi^*$ is the mesh size in the sample, which can be determined from the geometric mean $\sqrt{lL}$ of the smallest ($l$) and largest ($L$) distances in the pore, as obtained from TEM images (see Fig. 3.3c). We averaged up to 500 pores in ten different samples for each material to yield the average mesh size $\xi^*$. Table 1 shows the resulting values of $\xi^*$ and $\nu^*$. The mesh size $\xi^*$ from the $precursor_{50}$ is nearly 4 times larger than that of $FISP_{50}$, with the degree of entanglement $\nu^*$ being 2 orders of magnitude lower than that of the $FISP_{50}$. While the mesh size $\xi^*$ of the $precursor_{100}$ $\xi^*$ is about half that of $FISP_{100}$, the degree of entanglement $\nu^*$ of the $precursor_{100}$ is around 6 times higher than that of the $FISP_{100}$.

### *3.5 Bulk rheometry*

Fig. 3.6(a) shows the shear viscosity of the precursors as a function of the shear rate. The zero-shear viscosity $\eta_0$ of $precursor_{100}$ is four orders of magnitude larger than that of the $precursor_{50}$. $Precursor_{50}$ exhibited a distinct viscosity jump above a critical shear-rate

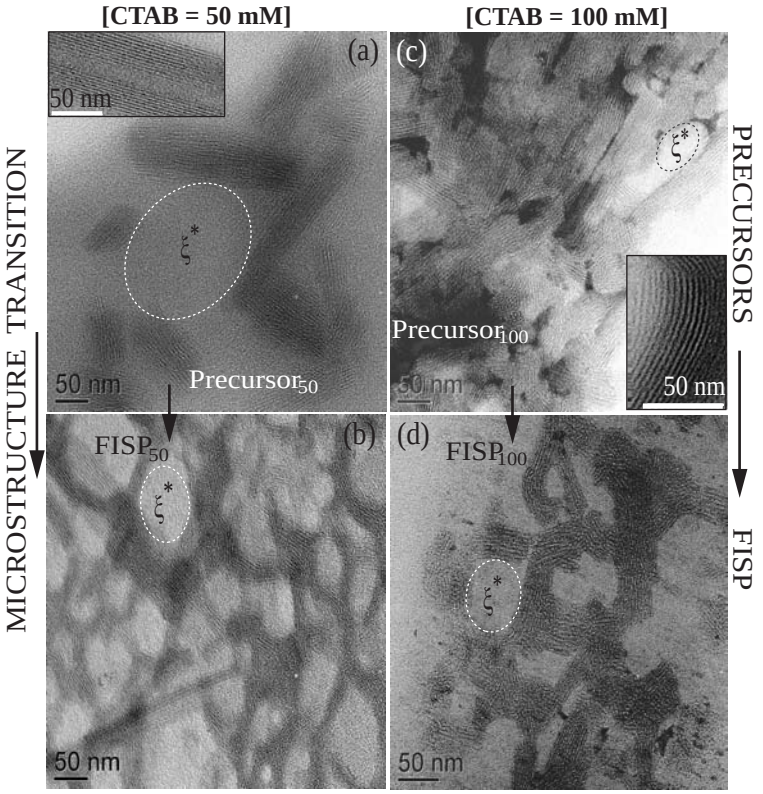


Figure 3.4: Each column shows the microstructural transition from the precursor→FISP. (a): TEM image of the precursor$_{50}$. (b) TEM image of entangled and branched micellar bundles of FISP$_{50}$; (c): TEM image of the precursor$_{100}$; (d): TEM image of entangled and branched network of FISP$_{100}$; The insets are zoomed-in micellar bundles . Conducted by TEM, Tecnai T-12, FEI Co, 120 kV.

($\dot{\gamma}_c \sim 50$ s$^{-1}$). This jump in the apparent viscosity has been attributed to the formation of transient SIS created by entangled wormlike micellar networks under shear flow [3,22–25,29]. When the shear rate is increased further ($\dot{\gamma} \sim 100$ s$^{-1}$), the wormlike micelles align in the flow direction, leading to a viscosity drop. The precursor$_{100}$ showed a shear thinning response above a critical certain shear-rate ($\dot{\gamma}_c \sim 0.085$ s$^{-1}$). Shear banding was also observed for the precursor$_{100}$ (see supplementary material).

Oscillatory-shear experiments were conducted at several strains within the linear viscoelastic regime. The viscoelasticity behavior of the precursors was correlated with a Maxwellian relationship using a single-dominant relaxation time. This stress relaxation time

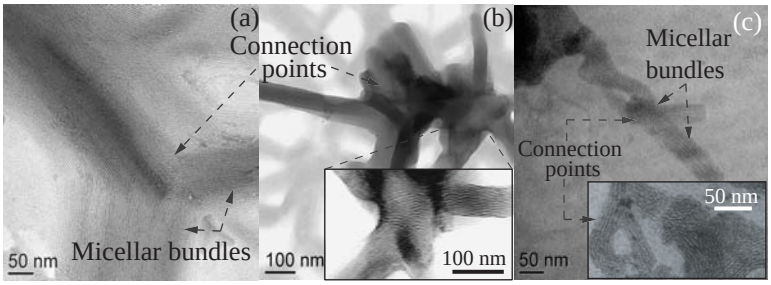


Figure 3.5: (a,b): TEM images of the $FISP_{50}$ show branched, entangled, and multi-connected micellar bundles. (c): TEM image of the $FISP_{100}$ shows entangled, branched, and multi-connected micellar bundles. The insets in (b) and (c) are zoomed-in images where branching points and connection points are presented. Conducted by TEM, Tecnai T-12, FEI Co, 120 kV.

$\lambda_{\text{eff}}$ can be extracted from the first cross-over between the viscous modulus ($G''$) and the elastic modulus ($G'$). The plateau modulus $G_0$ is the value at which $G'$ reaches a plateau at high frequencies. The frequency was varied from 0.01 to 100 Hz. Since our stress-controlled rheometer is not sensitive enough to extract the stress relaxation time $\lambda_{\text{eff}}$ for the weakly viscoelastic $\text{precursor}_{50}$, microrheometry was used to obtain both the stress relaxation time and plateau modulus. Fig. 3.6(c) shows good agreement between the bulk rheometry and the microrheometry of the $\text{precursor}_{50}$ within the frequency range of the bulk measurements. Several shear-oscillatory studies of CTAB based micellar solutions have shown that at low frequencies (0.01–30 Hz) they closely follow a Maxwellian trend [3, 22, 27, 74]. As the frequency increases the micellar solution starts to deviate from the Maxwell model, presenting a spectrum of relaxation times in the micellar solution where Rouse or Zimm models can be used to describe their dynamical behavior [75, 76].

### *3.6 Microrheometry*

We performed passive microrheology on the $\text{precursor}_{50}$, $FISP_{50}$, and $FISP_{100}$ [51, 52]. The volumes of FISP produced in the microdevice were small ($\sim 150\mu$L), so rheological properties were measured with microrheology. To facilitate these measurements, the precursor solution was seeded with 1 $\mu$m diameter polystyrene microspheres, with 0.01 wt% in the

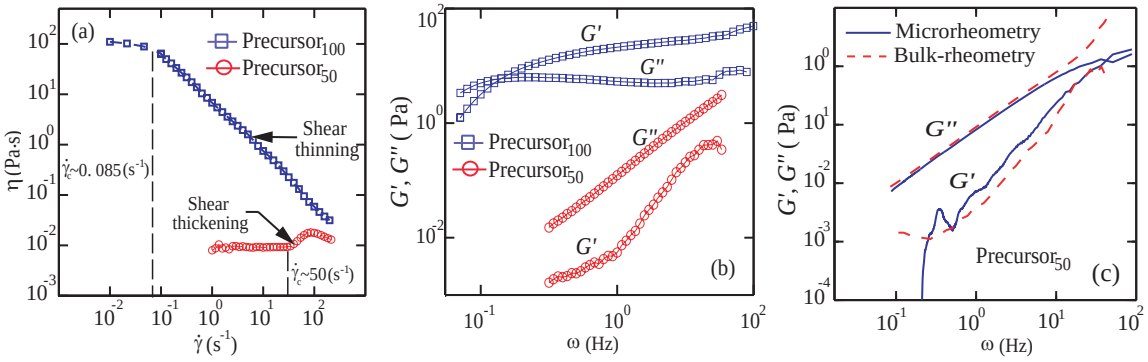


Figure 3.6: (a): Shear viscosity versus shear rate for both precursors. (b): G' and G" are plotted against the angular frequency $\omega$, under 0.5% strain. (c) G' and G" versus $\omega$ from precursor$_{50}$'s bulk rheometry and microrheometry data.

total solution. The seeded solution was then pumped into the microdevice at 15 mL/h. The two-dimensional mean-square displacement (MSD = $\langle \Delta r^2(t) \rangle$) of the embedded microbeads in the FISP was calculated and plotted. Some light smoothing using a moving average filter (windows size of 51 frames) was performed on the MSD data prior to further analysis. The MSD was then related to the complex modulus $G^*(\omega)$ of the FISP, with $\omega$ the frequency. The complex modulus comes from the Stokes–Einstein relation, which shows that the shear-stress relaxation in the locality of the particle is identical to that of the bulk fluid subjected to a shear strain [52]. This approach is valid when the length scale of the heterogeneity of the sample is much smaller than the probe particle size, which can be verified by our TEM images, see Table 1. Fig. 3.7a shows the MSD of the precursors and their corresponding FISP. For precursor$_{50}$, the mobility of the probe particles decreased for the FISP$_{50}$ (red solid curve below the dotted curve). However, the mobility of the probe particles increased for the FISP$_{100}$ (solid blue curve) as compared to the precursor solution (dotted blue curve). This behavior can be explained based on the microstructural evolution by reviewing the TEM images in Fig. 3.4(c,d) and their degrees of entanglement: precursor$_{100}$ exhibits more entangled wormlike micelles with smaller mesh size than those of the FISP$_{100}$. This structural transition, from smaller mesh size and more entangled wormlike micelles to larger

mesh size with connected and branched structures, leads to rheological variations between the precursor and FISP.

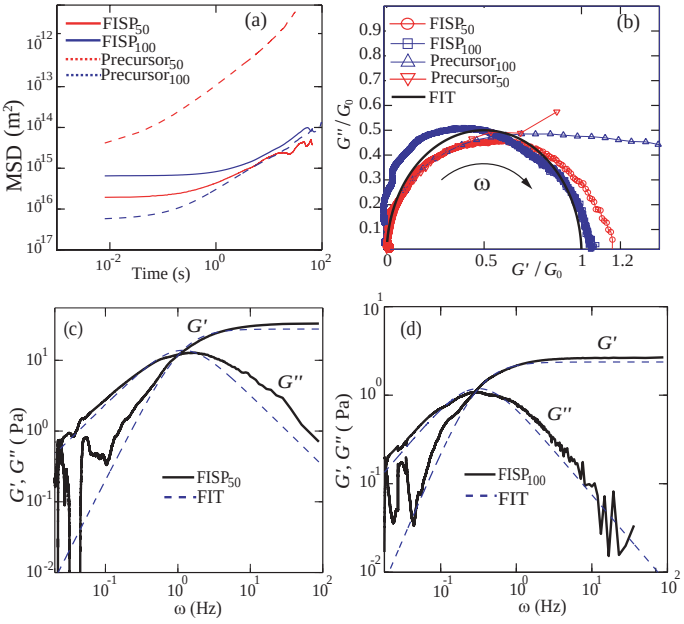


Figure 3.7: (a): The mean-squared displacement (MSD) versus time for two precursors and their FISP. The red and blue dash lines belong to the precursors whereas the red and blue solid lines correspond to the FISP; (b): Cole–Cole plots of the precursors and their FISP based on the microrheology measurements. The black semi-circle corresponds to the single mode Maxwell fit; (c): G' and G" versus $\omega$ for $\text{FISP}_{50}$ measured from microrheometry. The data is plotted against the dotted curves from single mode Maxwell fit; (d): G' and G" versus $\omega$ for $\text{FISP}_{100}$ measured from microrheometry. The data is plotted against the dotted curves from single mode Maxwell fit.

The microrheology data was further fitted to a single-mode Maxwellian linear viscoelastic model. Plots of $G'$ and $G''$ are versus the frequency $\omega$ for $\text{FISP}_{50}$ and $\text{FISP}_{100}$ appear in Fig. 3.7(c & d). While the blue-dash line follows the Maxwellian fit, the solid black lines correspond to the experimental data. The noise at low frequencies is caused by movement of probe particles in and out of the focus plane during the recording [51]. The plateau modulus

$G_0$ and zero-shear viscosity $\eta_0$ were either measured from the bulk rheometry or calculated based on $\eta_0 = G_0\lambda_{\text{eff}}$ from the microrheology. The rheological data of the precursors and FISP were also presented in Cole–Cole plots with normalized $(\frac{G'}{G_0}, \frac{G''}{G_0})$; see Fig.

Table 3.1: Mesh size and degree of entanglement of the precursors and FISP

| Samples | $\xi^*$ (nm) | $\xi = (\frac{k_B T}{G_0})^{1/3}$ (nm) | $\nu^* = \xi^{*-3}$ ($m^{-3}$) | $\nu = \frac{G_0}{k_B T}$($m^{-3}$) |
|---|---|---|---|---|
| $Precursor_{50}$ | 300±110 | 220±50 | $\|3.7 \pm 4.1\| \times 10^{19}$ | $(9.7 \pm 0.48) \times 10^{19}$ |
| $FISP_{50}$ | 80±21 | 70±13 | $(2.0 \pm 1.5) \times 10^{21}$ | $(3.6 \pm 1.9) \times 10^{21}$ |
| $Precursor_{100}$ | 47±12 | 60±18 | $(9.6 \pm 7.4) \times 10^{21}$ | $(4.8 \pm 0.17) \times 10^{21}$ |
| $FISP_{100}$ | 87±32 | 126±8 | $\|1.5 \pm 1.6\| \times 10^{21}$ | $(0.51 \pm 0.097) \times 10^{21}$ |

3.7(b). By conducting numerical simulation and employing a Poisson renewal model, Cates *et al.* [77, 78] proposed that if a wormlike micellar solution follows a semi-circle in a Cole–Cole plot, the solution should follow a single exponential stress relaxation process. However, if the micellar solution exhibits a flattened curve in the Cole–Cole plot (i.e., $precursor_{100}$), a broad distribution of relaxation times incur where the internal micellar dynamics may be dominated by reptation or Rouse breathing. At low frequencies, both precursors and their FISP fit the semi-circle (in solid black) with a mean-square error ∼8–10%. At larger frequencies ($\omega \geq 30$ Hz) both precursors start to deviate from the semi-circle fit, indicating the existence of a spectrum of relaxation times. With branched and multi-connected micellar bundles, both $FISP_{50}$ and $FISP_{100}$ fit the semi-circle in the Cole–Cole plot with a mean-square error of ∼5–12%. Higher deviation is observed at higher frequencies. Such behavior had been reported for CTAB-based micellar solutions [15, 22, 27, 79, 80] and other ionic wormlike micellar solutions [81, 82] due to their branching structures.

Table 2 summarizes the rheological parameters (zero-shear viscosity $\eta_0$, stress-relaxation time $\lambda_{\text{eff}}$, and plateau modulus $G_0$) of the precursors and the FISP. $Precursor_{50}$ is semi-dilute and weakly viscoelastic. While the value of $\eta_0$ for the $FISP_{50}$ is three orders of magnitude larger than that of $precursor_{50}$, the values of $\lambda_{\text{eff}}$ and $G_0$ of $FISP_{50}$ are around 40 times larger than those of $precursor_{50}$. These variations are consistent with structural transitions exhibited in the TEM images: $precursor_{50}$ is a semi-dilute wormlike micellar solution, with mesh size $\xi^* = 300 \pm 110$ nm and degree of entanglement $\nu^* = (3.7 \pm 4.1) \times 10^{19} m^{-3}$; gel-like $FISP_{50}$ shows a highly entangled, branched, and multi-connected micellar network with mesh size $\xi^* = 80 \pm 21$ nm and degree of entanglement $\nu^* = (1.95 \pm 1.54) \times 10^{21} m^{-3}$. Similar

rheological and structural transitions can be achieved by adding salt in the NaSal/CTAB system at equilibrium: excess salt ions enable the elongation and flexibility of the micelles, which promote the formation of branched and multi-connected networks [10, 14].

Precursor$_{100}$ exhibits stronger viscoelastic behavior and consists of densely entangled micellar bundles, with $\xi^* = 47 \pm 12$ nm and $\nu^* = (9.6 \pm 7.4) \times 10^{21}\mathrm{m}^{-3}$. The values of $\eta_0$ and $G_0$ for FISP$_{100}$ are around 10 times smaller than those of precursor$_{100}$, for which $\xi^* = 87 \pm 32$ nm and $\nu^* = (1.52 \pm 1.67) \times 10^{21}\mathrm{m}^{-3}$. For FISP$_{100}$, $\lambda_{\mathrm{eff}}$ is around 1.4 times smaller than that of precursor$_{100}$. Decreases of $\eta_0$, $\lambda_{\mathrm{eff}}$, and $G_0$ accompanying branched and multi-connected micellar networks have been reported for CTAB-based micellar solutions [8, 9, 79, 80] at equilibrium. The micelles can become negatively charged due to the excess of counterions at higher salt concentrations. Coulomb interactions hence become important and induce reductions in the length of micelles [83]. Cappelare and Cressely [12] observed similar trends in the rheological properties of CPCl/$NaClO_3$ solutions with the presence of branched structures. Kadoma and van Egmond [14] and Kadoma *et al.* [15] also reported a reduction in the rheological properties of [CTAB] = 0.03 M and [NaSal] = 0.06–0.24 M system with high salt concentrations. In their study,$\lambda_{\mathrm{eff}}$ decreased from 5.65 s to 2.18 s on increasing the salt to surfactant ratio from 5.5 to 8. Porte *et al.* [6], Appell *et al.* [7], and Khatory *et al.* [8] proposed that the multi-connections formed in the micellar solutions could slide against each other, yielding high fluidity and lower the zero-shear viscosity $\eta_0$ in the micellar structure. Even though this sliding mechanism might be present for both FISP$_{50}$ and FISP$_{100}$, variations in the rheological properties from the precursor to the FISP are found to correlate with the degree of entanglement (Table 1).

Drye and Cates [67] developed a theoretical framework to describe the formation of cross-links and multi-connections in wormlike micellar solutions at equilibrium. They predicted that unsaturated wormlike micelles with no connections or cross-links can evolve into cross-linked or multi-connected wormlike micellar structures under entropic fluctuations. They proposed that micellar cross-links lower the viscosity of wormlike micellar solutions. In equilibrium, entropic fluctuations can be enhanced by adding salt to the micellar system. At salt concentrations three times lower than those required at equilibrium, entropic fluctuations can be enhanced by spatial confinement and high extension (as present in our setup),

making it easier to cross the energy barrier between states and, thus, increasing transition frequencies between states, enabling the formation of entangled and branched micellar bundle networks. This flow-induced structural formation is highlighted in Fig. 3.8.

### *3.7 Mesh size*

To determine mesh size, we can either directly measure $\xi^*$ from TEM images or use an estimate $\xi$ based on polymer molecular theory. Shikata *et al.* [73] proposed that the elasticity of an aqueous wormlike micellar solution of CTAB/NaSal originates from the excess entropy caused by the orientation of some micellar chains between entangled points. Assuming that the wormlike micelles have Gaussian chains, rubber elasticity relates the elastic modulus and the thermal energy to the hydrodynamic correlation length (or the network mesh size $\xi$) as $\xi = (\frac{k_BT}{G_0})^{1/3}$, with $k_BT$ the thermal energy [84]. The plateau modulus $G_0$ can be obtained from our rheological measurements. For TEM-based predictions of the mesh size, sample preparation and image analysis can cause errors. On the other hand, limitations of the molecular theory and errors in the measurement of plateau modulus $G_0$ can also introduce difficulties. Despite these factors, Table 1 shows the same general trend for both approaches to determining the mesh size: for precursor$_{50}$, the mesh size is about 4 times larger than that of the FISP$_{50}$; for precursor$_{100}$, the mesh size is about half of that of FISP$_{100}$. Similar trends also hold for the degree of entanglement: $\nu^*$ (or the corresponding theoretically-determined quantity $\nu$) of precursor$_{50}$ is two orders magnitude lower than that of FISP$_{50}$; $\nu^*$ (or $\nu$) of precursor$_{100}$ is around six times higher than that for FISP$_{100}$. Note that TEM yields similar values of $\xi^*$ FISP$_{50}$ and FISP$_{100}$ have similar values. For FISP$_{100}$, $\xi$ is larger than $\xi^*$. One possible explanation is that $G_0$ measured from the microrheology might be lower than the actual value because some precursor can become trapped in the FISP$_{100}$ sample, leading to an overestimate of the mesh size.

### *3.8 Conclusions*

In summary, we show that stable flow-induced structures (FISP) can be formed from semi-dilute wormlike micellar solutions. We highlight three key results: (1) FISP are stable and can form from both shear-thickening and shear-thinning micellar solutions; (2) FISP contain highly entangled, branched and multi-connected micellar bundles, formed at low salt

Table 3.2: Rheological properties of the precursors and FISP

| Fluid | $\eta_0$(Pa·s) | $\lambda_{\text{eff}}$(s) | $G_0$(Pa) |
|---|---|---|---|
| Shear thickening Precursor$_{50}$ | $(8.0\pm0.40)\times10^{-3}$ | $(2.0\pm0.10)\times10^{-2}$ | $(4.0\pm0.20)\times10^{-1}$ |
| **FISP**$_{50}$ | 13±5.0 | 0.86±0.20 | 15±8.0 |
| Shear thinning Precursor$_{100}$ | $(1.2\pm0.034)\times10^{2}$ | 5.9±0.18 | 20±0.70 |
| **FISP**$_{100}$ | 8.4±1.1 | 4.1±0.70 | 2.1±0.40 |

concentrations (∼three times lower than those formed at equilibrium [6–8]), enabled by the spatial confinement and flow conditions. Micropost arrays allow for high extension and shear rates, which promote flow alignment and high stretching of the wormlike micelles, decreasing their bending rigidity. The free energy of surfactant molecules in end-caps therefore increases relative to the curvature energy in the cylindrical micellar body, leading to a decrease in the work required to form junctions. As flexible adjacent micelles flow through the confined microposts, it becomes energetically favorable to minimize the number of end caps while concurrently promoting the formation of cross-links, yielding highly entangled, branched, and multi-connected bundles (FISP); (3) Transitions of the rheological properties (zero-shear viscosity, stress-relaxation time, and plateau modulus) are associated with structural evolution from the precursor to the FISP, which can be correlated with the mesh size and the degree of entanglement in each system.

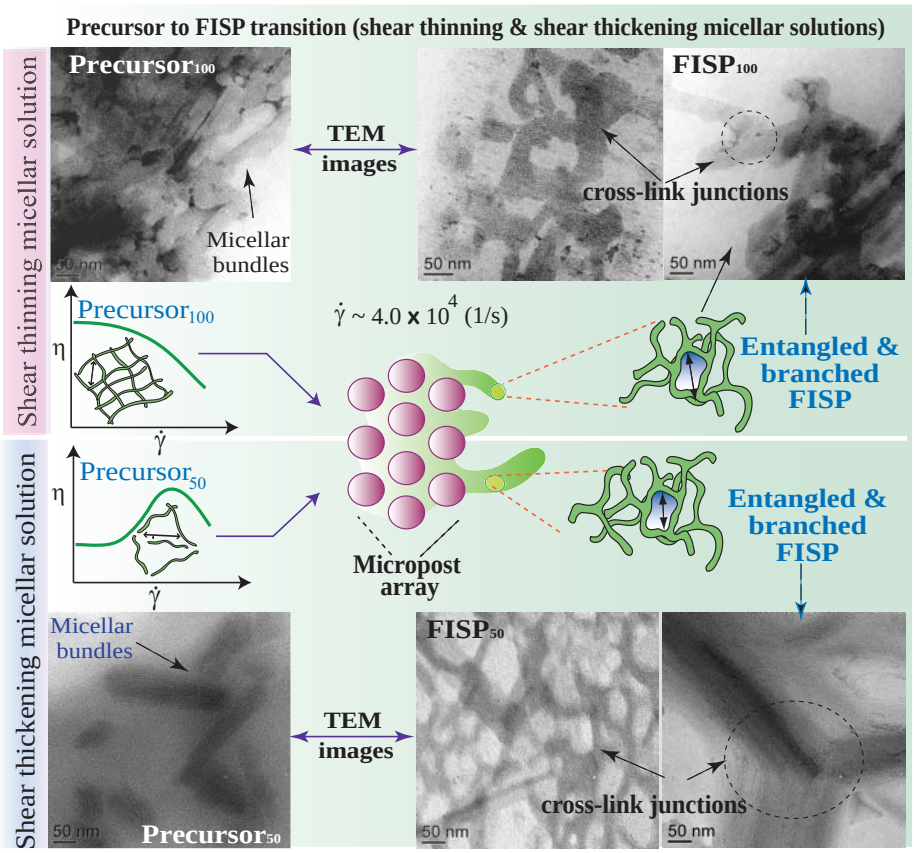


Figure 3.8: Schematics of the structural transition from the precursor to FISP of both shear thinning (top panel) and shear thickening (bottom panel) wormlike micellar solutions. This phase diagram highlights the transition from semi-dilute, entangled linear micelles to entangled, branched and multi-connected micellar bundles under flow conditions, at low salt concentrations.

Chapter 4

# FORMATION OF FISP BY USING SHNC/CTAB MICELLAR SOLUTION

## *4.1 Introduction*

Surfactants molecules spontaneously self assemble in aqueous solutions above a critical micellar concentration (cmc). The addition of inorganic salts (e.g., sodium chloride, NaCl) or organic salts (e.g., 3-hydroxynaphthalene-2-carboxylate, SHNC) to cationic surfactants reduces electrostatic forces within surfactant head groups and induces micellar growth. [1, 19, 22, 26, 86, 99]. Hydrotropic salts (e.g., SHNC) have gained attention due to similar structure to surfactant molecules (hydrophilic-hydrophobic configuration). SHNC has very similar molecular structure compared with sodium salicylate (NaSal, another hydrotropic salt), but with an extra benzene tail as shown in Fig. 4.1. SHNC is thus considered as an anionic surfactant similar to SDS but with a shorter hydrophobic tail [90, 91, 95].

The chemical structure of the SHNC is the main reason to form precipitates in equimolar CTAB/SHNC micellar solutions. Since a closer proximity and better interactions between carboxyl (position 2) and hydroxyl (position 3) groups exist in SHNC molecules, stronger bonds could be formed in wormlike micelles (see Fig. 4.1). Therefore, it is proposed that the specific geometry in SHNC is responsible for the phase transition difference in SHNC-cationic surfactant solutions when compared with other organic salts (e.g., NaSal). SHNC reduces cmc of cationic surfactants, as well as, decreases micellar charge density and promotes micellar growth (formation of wormlike micelles) [19,100,103]. SHNC based wormlike micellar solutions exhibits viscoelastic properties similar to polymer solutions [102, 111]. Nevertheless, SHNC based wormlike micelles constantly break and recombine under different conditions, such as, increasing SHNC concentration, changing temperature or flow conditions. When the kinetic process of micellar breaking and reforming dominates, the fluid shows a Maxwellian behavior with a single exponential decay of stress function and

a single relaxation time [2]. On the other hand, when the micellar breakup time is long compared with reptation time, dynamic properties of these micellar solutions are dominated by reptation processes [2, 67].

SHNC has been extensively used to form other surfactant aggregates (e.g., vesicles). For instead, Mishra *et al.* [108,109] investigated the phase behavior of a mixture of CTAB/SHNC by fixing the CTAB concentration at 60 mM and increasing the SHNC/CTAB molar ratio. They observed the transition of small micellar aggregates to a positive charged gel phase. Further increase of the SHNC induced the formation of a liquid crystallization lamellar phase, followed by a precipitate multi-lamellar vesicles phase at equal molar CTAB/SHNC concentration. They reported that the excess $Na^+$ (from SHNC) and $Br^-$ (from CTAB) ions in solution screened the electro-repulsive forces between vesicles and collapsed them into a sticky and thick precipitate [91]. Furthermore, micelles in cationic-SHNC solutions are very sensitive to temperature variations. Kalur *et al.* [106] observed an unusual increase of viscosity and relaxation time of a mixture of 280 mM SHNC and 60 mM EHAC at elevating temperatures. Verma *et al.* [92] reported the formation of elongated micelles and vesicles CTAB micellar solutions with exessive amount of SHCN by using bulk rheometry and light scattering techniques. They proposed that the $HNC^-$ ions can desorb from the micelles and decrease the surface charge of micelles with elevating temperatures or dilution, promoting further growth of wormlike micelles and enhancing the viscoelasticity of the solution.

Recently, we reported the formation of a flow-induced structured phase (FISP) by using low concentrations of the organic salt sodium salicylate ([NaSal=16 mM]) and [CTAB=50 mM] [167]. We suggested that the formation of NaSal-based FISP was induced by spatial confinement along with local micellar concentration fluctuations and entropic fluctuations during flow [14,48,69]. Motivated by the formation of NaSal-based FISP, we explored the formation of SHNC-based FISP by using low concentrations of the aqueous mixture of SHNC/CTAB ([CTAB=45 mM] and [SHNC=14.4 mM]). We used a microfluidic device consisting of hexagonal micropost arrays (same device used in Cardiel *et al.* [167]) to form the FISP (see Fig. 4.1 and Figure 4.2). We performed bulk rheological characterization of the original liquid precursor, as well as, two point passive microrheology of the FISP. We used small-angle neutron scattering (SANS), transmission electro microscopy (TEM) and scanning electron

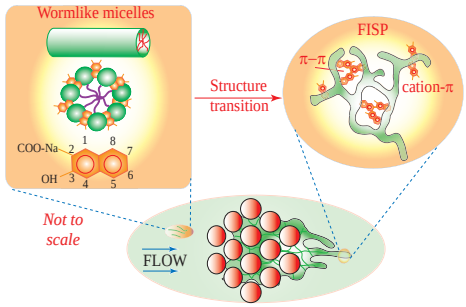


Figure 4.1: The naphthalene structure presented in SHNC favors curvature change and ion pairing of CTAB micelles and induces a uni-dimensional growth of wormlike micelles (precursor). When the precursor is subjected to high strain rates of ~3.7 x $10^4$ $s^{-1}$ and total strain of ~2.1 x $10^3$ $s^{-1}$ the formation of micellar networks (FISP) begins to happen.

microscopy (SEM) to observe the structure of the FISP. The strong binding affinity (cation-$\pi$ and $\pi-\pi$) between hydrophobic naphthalene structures in SHNC micelles greatly faciles the formation of nanoporous FISP with strong viscoelastic properties under spatial confinement in microfluidics.

### *4.2 Microrheology*

Due to the small volumes of the FISP produced in the microdevice (~150 $\mu$L), rheological properties of the FISP were measured by passive two point microrheology [54]. Two point passive microrheology (2PPM) relates the thermal motion of tracer particles embedded in a fluid to approximate its rheological properties. 2PPM does not depend on the shape and size of the tracer particles; most importantly, it is independent of the coupling medium and particle tracers. In other words, 2PPM is a good approximation to measure rheological properties of highly inhomogeneous materials [54,120,121]. From the TEM and SEM images, we observed that the FISP exhibited highly inhomogeneous microstructure with large range of pore size. In the FISP's structure some particles could be inside cages while others could be surrounded by the micellar network, making the two point microrheology a good technique to approximate the FISP's rheology. 2PPM correlates the strain field of one tracer particle to a second tracer particle [54]. To facilitate these measurements, the precursor solution was seeded with 1 $\mu$m diameter polystyrene tracer particles, with ~0.3 wt % in

the total solution. The experiments were conducted on an inverted Leica microscope at 23 ±0.8 °C. Harvard Apparatus digital pumps were used to pump the precursor through the device at a constant flow rate (15 mL/h). After a sufficient amount of FISP was produced in the microchannel, we waited for ∼2 h before conducting the 2PPM measurements. Then, a region of the FISP containing more than 200 tracer particles per video was imaged at a magnification of 150× (PL Fluotar 100× 1.30 oil objective with a 1.5× tube lens), and videos consisting of 2048 frames were taken at 60 fps with a high-speed camera (Photron FASTCAM). To avoid wall effects, the focal plane was set at ∼30 $\mu$m from the bottom and top parts of the microchannel. A total of 25 videos were analyzed to approximate the rheological properties of the FISP.

From the cross-correlated thermal motion of pairs particles, we determined the complex modulus $G^*(\omega)$ of both precursor and FISP. The complex modulus comes from the Stokes–Einstein relation, which shows that the shear stress relaxation in the locality of the particle is identical to that of the bulk fluid subjected to a shear strain [52]. The complex modulus is defined as $G^*(\omega) = G'(\omega) + iG''(\omega)$, where $\omega$ is the frequency, $G'(\omega)$ is the elastic modulus and $G''(\omega)$ is the viscous modulus. We used multiparticle tracking video-microscopy to measure the two-dimensional mean-square displacement (MSD = $\langle \Delta r^2(t) \rangle$) of the embedded microbeads in the FISP [55]. We then calculated the tensor of pairwise cross-correlated bead displacements as a function of separation distance $r$ and lag time $\tau$, and the component in the direction of bead separation, $D_{rr}(r, \tau)$ was used to extract $G^*(\omega)$ [52,54]. The correlated displacement of two tracer particles was driven by those modes with wavelengths greater than their separation distant $r$ rather than $a$ (radius of the tracer particles), since the shorter wavelength modes did not move the tracer particles in phase. Hence, the correlated motion (in Laplace space) of two tracer particles can be defined as [54]:

$$\tilde{D}_{rr}(r, s) = \frac{k_B T}{2\pi r s \tilde{G}(s)}, \tag{4.1}$$

where the MSD is related to $D_{rr}$ through

$$\langle \triangle r^2(\tau) \rangle_D = 2\frac{r}{a} D_{rr}(r, \tau), \tag{4.2}$$

and the complex modulus ($G^*(\omega)$) can be obtained by Fourier transform $\tilde{G}$(s) such as [52]:

$$\tilde{G}(s) = |G^*(\omega)| \approx \frac{2k_BT}{3\pi a\langle\triangle r^2(\frac{1}{\omega})\rangle\Gamma(1+\alpha(\omega))}, \tag{4.3}$$

where $k_B$ is the Boltzmann constant, $T$ is the absolute temperature, $a$ is the radius of the tracer particle, $\Gamma$ is the gamma function, and

$$\alpha(\omega) = \frac{d(ln(\triangle r^2(\omega^{-1})}{d(ln(\omega^{-1}))}, \tag{4.4}$$

is the logarithmic slope of the MSD, finally from the complex modulus the viscoelastic response ($G'(\omega)$ and $G''(\omega)$) of the FISP can be approximated. Two point passive microrheology process approximates $\langle\triangle r^2(\tau)\rangle$ locally by a second order polynomial in the logarithmic scale to extract $G^*(\omega)$ [54]. Hence, this process has the advantage that it does not require the experimental data to be fit to an analytical model, nor does it suffer from truncation errors of numerical integrations.

### *4.3 Formation of FISP*

By using similar devices reported by Cardiel *et al.* [167], we suggested that the same mechanism to form NaSal based FISP can be used to form SHNC based FISP. The high stretching in the micropost array (O($10^4$ $s^{-1}$)), entropic fluctuations and flow alignment enables SHNC ions to penetrate to the core of wormlike micelles at high frequency, increase flexibility of wormlike micelles, therefore reduce the curvature of the cylindrical part of the micelle [13–15, 48, 69]. As a result, the free energy of surfactant molecules in the end-cap relative to the curvature energy in the cylindrical body of the micelle becomes larger, hence the energy required to interconnect wormlike micelles will decrease [8,16,67,100]. Thus it becomes energetically favorable for flexible adjacent micelles to merge when they flow through the confined microposts, promoting the formation of FISP (see Fig. 4.2) [10, 67–69]. Fig. 4.2 (c) exhibits the formation of FISP-like fingers, the inset in Fig. 4.2 (c) qualitatively gives a sense of the high viscoelastic properties of the FISP. The inset in Fig. 4.2 (c) shows long sheet-like filaments (∼420 $\mu$m of length, ∼75 $\mu$m of height and ∼5 $\mu$m in width) before rupture, indicating, the high stretchability of the FISP structure.

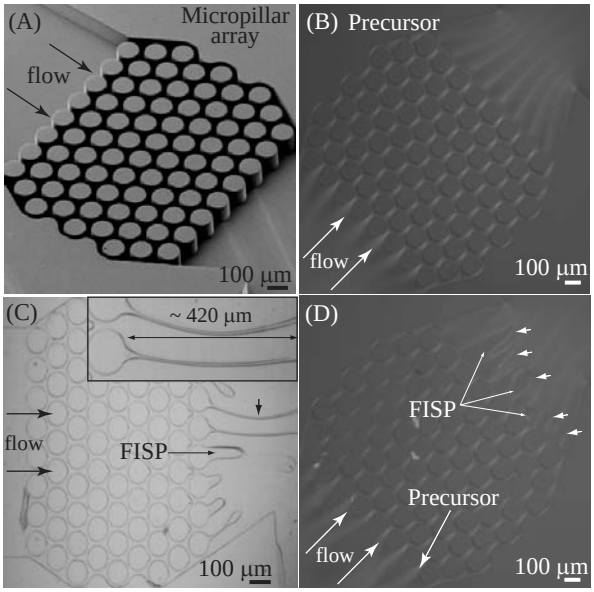


Figure 4.2: (a) SEM image of the hexagonal micropost array to produce FISP. (b) Flow birefringence of the precursor, bright bands were observed indicating the formation of anisotropic micellar structures. (c) Snapshot of the FISP formation showing FISP-like fingers. The inset in (d) shows the formation of long FISP filaments giving a qualitative sense of the viscoelastic properties of the FISP; (d) The FISP does not exhibit birefringence behavior, the white arrows in (d) point FISP-like fingers.

For a hexagonal array with posts of diameter $100\,\mu$m and a spacing of $15\,\mu$m, $\phi = 0.31$ (see Fig. 4.2 (a)). So for a flow rate of 15 mL/h and the channel dimensions given in the materials and methods section, equation (2.38) gives $\hat{\dot{\gamma}}_{\text{total}} \approx 3.7 \times 10^4\,\text{s}^{-1}$. The average velocity can be calculated as $\hat{U}_{\text{avg}} \approx 0.21$ m/s, while the average residence time of a fluid element is $\hat{L}/\hat{U}_{\text{avg}} \approx 0.057$ s. Hence the total strain was estimated as $\hat{\gamma} \approx 2100$.

We observed that the precursor showed flow birefringence before and after passing through the micropost array, indicating the formation of anisotropic structures, also known as, shear induced structures [4, 46, 108, 109] (see Fig. 4.2 (b)). The microstructural origin of flow–birefringence is that, when an isotropic entangled micellar network is sheared, segments of the wormlike micelles disentangle and align with the flow direction [4, 46]. We did not notice flow birefringence in the FISP structure. We implied that the highly inhomogeneous structure of the FISP, high entanglement density of wormlike micelles in the FISP, and the thickness of the FISP ($\sim$75 $\mu$m) in the microchannel were the main reason to not observe

birefringence behavior (see Figure 4.2 (d)). Nevertheless, we noticed flow birefringence at the interface of the FISP and precursor (white arrows in Figure 4.2 (D)). We suggested that this interface birefringence might be induced by the precursor or some alignment of the micellar bundles of the FISP at the precursor-FISP's interface. There have been reported that SHNC based wormlike micelles exhibit flow birefringence at high salt concentrations (>80 mM) [46, 108, 109]. Frounfelker *et al.* [46] reported persistence birefringence in samples containing 40 mM EHAC and 80–240 mM NaHN. They attributed the persistence birefringence to the $\pi - \pi$ interactions presented in HNC aromatic salt. Further, Mishra *et al.* [108, 109] studied an aqueous mixture of the cationic surfactant CTAB([60 mM]) and SHNC ([100 mM]) and observed that a mild tilt or tapped could induce pronounced birefringence lasting for milliseconds.

### *4.4 Rheometry of precusor and FISP*

Fig. 4.3 shows the shear viscosity of the precursor as a function of the shear rate. The precursor solution showed a shear thinning response once a critical shear rate is reached ($\dot{\gamma}_c \sim 0.85\ \mathrm{s}^{-1}$). The inset in Fig. 4.3 suggests the presence of shear banding in the precursor, based on the shear stress versus shear rate curve (highlighted flat region in the curve $\tau\ vs\ \dot{\gamma}$). Shear banding behavior has been related to the presence of aligned wormlike micellar structures with flow birefringence response [4]. Oscillatory-shear experiments were conducted at several strains to ensure the linear viscoelastic regime. The viscoelasticity behavior in the precursor was correlated with Maxwellian relationship with a single-dominant relaxation time. This stress relaxation time $\lambda_{\mathrm{eff}}$ can be extracted from the first cross-over between the viscous modulus ($G''$) and the elastic modulus ($G'$). The range of frequencies were varied from 0.01 to 100 Hz. Fig. 4.4 shows good agreement between the bulk rheometry and the two point passive microrheometry of precursor within the $\omega$ limit from the bulk rheometry.

Two point passive microrheometry was performed due to the highly inhomogeneous structure of the FISP (see Fig. 4.9). We calculated the pairwise cross-correlated tracer particle displacement as a function of the separation $r$ and the lag time $\tau$, and the component of the separation of the tracer particles $D_{rr}$, was used to approximate $G^*(\omega)$ [54]. This process

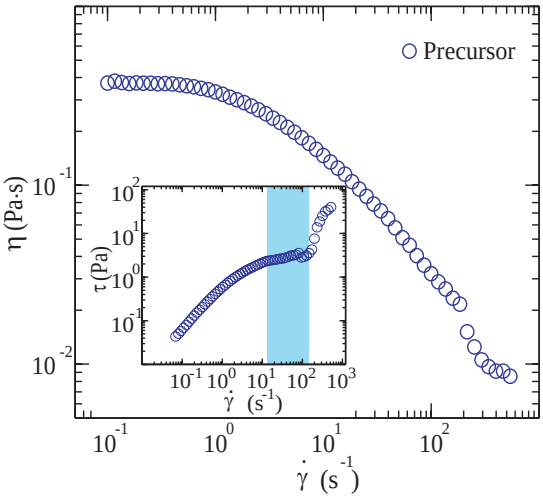


Figure 4.3: Shear viscosity versus shear rate for precursor solution exhibiting shear thinning behavior above a critical shear rate ( $\dot{\gamma} \sim 0.855\ s^{-1}$). The inset shows the non-monotonic behavior of the stress versus shear rate, suggesting the presence of shear banding (blue area).

has been previously used to obtain the viscoelastic response of highly inhomogeneous biological fluids [120, 121]. We determined the correlated displacements of particles separated by a distance, 5 $\mu m < r <$ 100 $\mu m$. Fig. 4.4 also shows the frequency dependent behavior ($G'(\omega)$ and $G''(\omega)$) of the FISP approximated by two point microrheology. The two point passive microrheology method has the advantage that it does not require the experimental data to be fit to analytical model due to the power law approximation of the mean-square displacement [52, 54]. From the crossover between $G'(\omega)$ and $G''(\omega)$ we approximated the value of the relaxation time ($\lambda_{\text{eff}}$) of both precursor and FISP. The plateau elastic modulus $G_0$ is the value at which $G'$ showed a constant plateau at high frequencies, and the zero shear viscosity ($\eta_0$ was either measured from the bulk rheometry for the precursor, or calculated based on $\eta_0$=$G_0\lambda_{\text{eff}}$ for the FISP [84]. $G_0$ of the precursor was obtained by relating the $\lambda_{\text{eff}}$ from microrheology or bulk rheometry and the $\eta_0$ from bulk rheometry, yielding $G_0$=$\eta_0/\lambda_{\text{eff}}$ [84]. Table 1 summarizes the rheological properties of both precursor and FISP. The zero shear viscosity, $\eta_0$, and the elastic modulus $G_0$ of the FISP are one order of magnitude larger than those of the original precursor. Interestingly, the relaxation time $\lambda_{\text{eff}}$ of both precursor and FISP was not strongly affected, maintaining the same order

of magnitude after the structural transition from precursor to FISP. It has been reported that structural transitions in micellar solutions (e.g., formation of branches) are attributed to rheological changes in micellar solutions [4, 6, 67].

It is important to mention that microrheology techniques could underestimate the rheological properties of viscoelastic fluids due to dynamic and static errors during the particle tracking [118], compressibility effects [210], and most importantly, the correct determination of the maximum separation distance ($r$) within the tracer particles to obtain their cross-correlation motion [119]. For instance, Fu *et al.* [210] reported that microrheology techniques tended to under-estimate the elastic modulus in polymer networks. They studied the effects of slip condition and compression effects on the tracer particle used in the microrheology. When the sliding condition and compression effects are present at the same time, the elastic modulus in the polymer networks can decrease $\sim$43% from the true value. Further, they observed that at low frequencies ($<$ 1 rad/s), the discrepancy between the bulk rheology and microrheology could be caused by the sliding and compression effects. In two point passive microrheology the motion of the tracer particles induces the propagation of waves which are generated at the particle–fluid interface, and then those waves reflect back and forth within the tracer particles [54, 119]. Hence, the cross-correlations of two tracer particles is determined by the nature of those waves. Levine and Lubensky [56] have showed that the cross-correlation function proposed by Crocker *et al.* [54] was valid when the distance between two tracer particles was larger than the radius of the particle. It has been reported that if the separation distance between beads is large enough, the reflected waves decay significantly before reaching other tracer particles. However, if the separation distance is short enough, reflected waves would have important contributions on the motion of particle tracers. Hence, the viscoleastic response of the material is affected by the separation distance of the tracer particles. Therefore, all these factors (video-tracking particles, compressibility effects and correct separation distance within tracer particles) might be presented in the rheology of the FISP, nevertheless, this study provides an approximation of the rheological properties of the FISP.

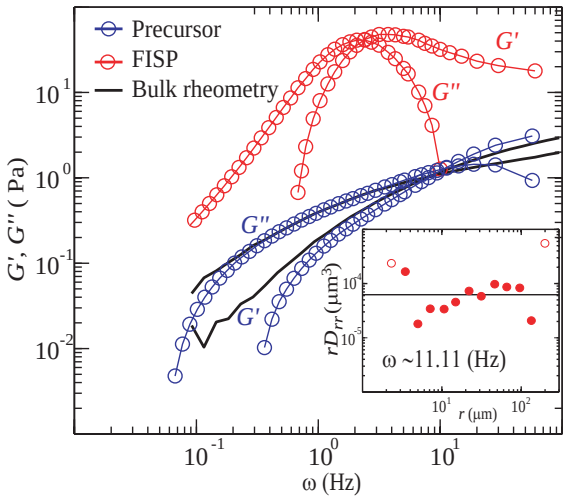


Figure 4.4: Viscoelastic response of the precursor and FISP. The bulk rheometry (black solid line) and the two point microrheometry (blue circles) exhibit similar linear viscoelastic response. Red circles show the viscoleastic behavior of the FISP obtained by two point microrheometry. The inset shows the $r$ dependence of $rD_{rr}$ for $\omega\sim$11.11 Hz.

Table 4.1: The longest relaxation time $\lambda_{\text{eff}}$, plateau modulus $G_0$, and the zero-shear viscosity $\eta_0$ for the precursor and FISP

| Materials | $\eta_0$ (Pa· s) | $\lambda_{\text{eff}}$ (s) | $G_0$ (Pa) |
|---|---|---|---|
| precursor | 0.41±0.02 | 0.11±0.01 | 3.6±0.18 |
| FISP | 4.6±0.26 | 0.42±0.08 | 11±3.3 |

### *4.5 Behavior of the FISP and precursor at different temperature*

We have performed SANS and USANS in both precursor and FISP at different temperatures (25, 30, 45, and 60 °C). We observed a clear structural transition from the precursor to the FISP at 25 °C (see Figure 4.5). At high-$q$ we fitted both precursor and FISP spectrum to a cylinder model [58]. The fitting of the FISP provided a cylinder radius and length of ∼2.4 nm and ∼24 nm respectively. Whereas, the fitting of the precursor gave a cylinder radius and length of ∼2.4 nm and ∼18 nm respectively. We observed that at high-$q$ the cross sectional area of the wormlike micelles of both FISP and precursor maintains constant, however, the length of the micelles in FISP is larger than that of the precursor, indicating that the wormlike micelles slightly growth after passing through the micropost array. The SANS spectra at low-$q$ of the FISP (red-squares in Figure 4.5) differs significantly from that of the precursor (blue-circles in Fig. 4.5) at low-$q$. At $q < 0.03$ Å$^{-1}$, the spectrum of the FISP begins to increase, indicating the presence of larger structures. We fitted the low-q spectra of the FISP to a fractal model based on Teixeira model to evaluate the network scale structure of the FISP [58]. This is primarily reflected in the USANS spectra ($q < 10^{-3}$Å$^{-1}$). From the fitting, we obtained a fractal dimension ($D_f$) of 2.95±0.05 and correlation length ($C_l$) of ∼500±136 nm. The value of $D_f$ is representative of gel-like networks with characteristic size on the order of several nanometers ($C_l$) [58]. Our TEM images (see inset in Figure 4.5 and Figure 4.9) exhibits the formation of micellar networks with dimensions of ∼ 200–700 nm. The fitting and our microscopy techniques imply the formation of micellar networks with size ranging from several nanometers to hundreds of nanometers. The SANS data exhibit a drastic transition upon passing the precursor through the microchannel that induces the appearance of a gel-like scattering pattern with large domains at low-$q$ [58] . The SANS data at low-wave vector shows a representative scattering pattern similar to that of gel-like structures with fibrin networks. However, the SANS data is not able to prove unequivocally that the FISP is composed just by wormlike micelles because of the lack of a structure factor suitable to describe the FISP. From the spectra comparison, we cannot conclude that the FISP is solely composed by wormlike micelles. Hence, we have to combine all the techniques (SEM, TEM, microrheology, and SANS) presented in this paper to suggest that the FISP

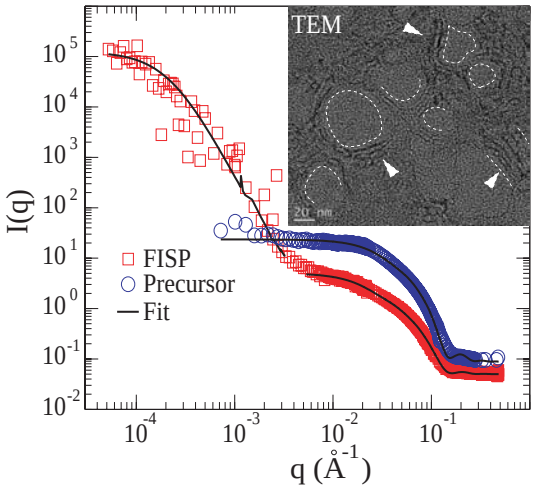


Figure 4.5: Combined SANS and desmeared USANS spectra of the FISP (red squares), compared with the precursor SANS scattering (blue circles). The low-q spectrum was fitted to a fractal model (solid black line). The fit yields a fractal dimension of $D_f$=2.95±0.05 and correlation length $C_l$=500±136 nm. $D_f$ suggests the formation of network structure. The inset is a TEM image of the FISP showing network-like structures. The high-q spectra of both FISP and precursor were fitted to cylinder model (black solid line). The fit of the FISP shows a cylinder diameter of ∼2.4 nm with length of ∼24 nm. Whereas, the fit of the precursor shows a cylinder diameter of ∼2.4 nm with length of ∼18 nm.

is formed by highly entangled and multi-connected micellar networks. Our SEM images and TEM images present highly entangled and multi-connected wormlike micelles and the rheology of the FISP exhibits similar response as those reported for branched micelles [6,67].

### *4.6 Behavior of the FISP and precursor by changing temperature*

Fig. 4.6 shows the SANS spectra of the precursor at higher temperatures. We fitted the precursor's spectra to a cylinder model to approximate the dimensions of the wormlike micelles at higher temperatures. From the SANS fitting, we noticed that the radius of the cylinder keeps constant (∼2.4 nm) for all the temperatures analyzed. However, the length of the cylinder monotonically decreases as the temperature increases, being ∼18 nm at 25 °C, ∼17 nm at 30 °C, ∼16 nm at 45 °C, and ∼12 nm at 60 °C. Normally, when wormlike micellar solutions are heated, the micellar contour length $L$ decreases exponentially with

temperature [106]. At higher temperatures, the end-cap of wormlike micelles is energetically unfavorable over the body, thus, because the end-cap constraint is less severe at higher temperatures, the wormlike micelles become shorter. The shortening of the wormlike micelles leads to an exponential decrease in the rheological properties ($\eta_0$, $G_0$, and $\lambda_{\text{eff}}$). The inset in figure 4.6 shows the zero shear viscosity behavior of the precursor at different temperatures. The zero shear viscosity $\eta_0$ of the precursor decreases as the temperature increases. Hence, the drop of $\eta_0$ is related to the shortening of the wormlike micelles. Kalur *et al.* [106] observed that EHAC/SHNC ([SHNC = 360 mM], high salt concentration) wormlike micelles growth as the temperature increased from 25 °C to 65 °C. By fitting the SANS spectra of their EHAC/SHNC micelles, they found that the radius of the wormlike micelles maintained constant (∼2.6 nm) for the range of temperatures studied. However, they observed a structural transition from spherical micelles (∼2.6 nm) to cylindrical micelles (length∼60 nm) as the temperature was increased.

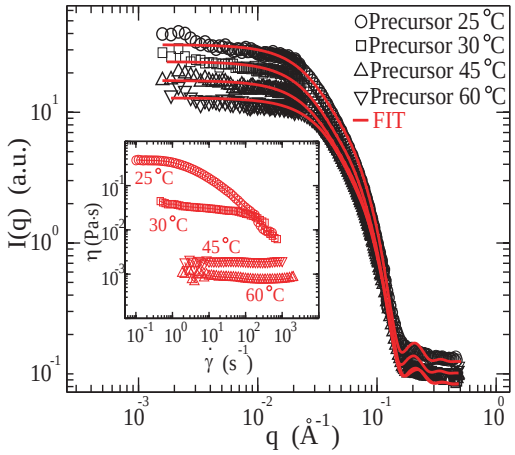


Figure 4.6: SANS spectra of the precursor at different temperatures. The inset presents the zero shaer viscosity of the precursor at different temperatures.

Fig. 4.7 presents the high-$q$ SANS spectra of the FISP at higher temperatures. We observed a monotonic decrease in the SANS spectra of the FISP by increasing temperature at $q > 10^{-2}\text{Å}^{-1}$, indicating the re-structuration of the FISP at the sub-nanometer scale. We found that the FISP's spectra can be fit to a cylinder model for the temperatures 25,

30, and 45 °C. Whereas, the FISP's spectra at 60 °C fit well to a spherical model. From the cylindrical fitting, we observed that the radius of the cylinder remains constant (∼2.4 nm) for all the three temperatures (25, 30, 45 °C); while the length of the cylinder ($L$) become shorter by increasing the temperature, being $L$=25 nm at 25 °C, $L$=19 nm at 30 °C, and $L$=17 nm at 45 °C. We noticed a drastic structural transition from 45 °C to 60 °C in the FISP spectra at $q > 10^{-2}$Å$^{-1}$. From the SANS fitting at 60 °C, we found that the best fit was obtained by using spherical model with a radius of ∼3 nm. It is important to mention that we attempted to fit the spectra of the FISP at 60 °C by using an ellipsoid model and elliptic-cylinder model, however, we sphere model gave the less squared-error in the fit. At $q < 10^{-2}$Å$^{-1}$, we noticed that the FISP's spectra exhibited the same trend for all the temperatures studied (25, 30, 45, and 60 °C), indicating the no disintegration of the large structures of the FISP as the temperature is increased. We fitted the spectra at low-$q$ for all the temperatures studied to a power law model and find a power index of ∼3.5±0.05. Such power index implies the presence of large domains with similar dimensions in all the temperatures studied. It is remarkable that the large structures of the FISP does not disintegrate at high temperatures, even more, the dimension of such large domains of the FISP maintain similar as the temperature increases. We suggested that the high entanglement density ($\nu = \frac{G_0}{k_B T} \approx 27.5 \pm 1.5 \times 10^{21}$ (m$^{-3}$) [84]) of the FISP was one the reasons to keep together the FISP's structure at high temperatures, inducing no changes in SANS spectra. We also suggested that the strong non-covalent interactions (e.g., hydrophobicity and counterions effects) was the other reason to maintain the FISP structure at high temperatures [46]. The naphthalene base of SHNC induces higher aromatic interactions ($\pi - \pi$ and cataion–$\pi$) within micelles, enhancing attractive potential in wormlike micelles [46, 116, 117]. Such noncovalen interactions may be sufficient to counteract the tendency of wormlike micelles to dissociate at high temperatures. Nevertheless. it might be possible that at high temperatures some wormlike micelles become shorter or some micellar bundles begin to dissociate. It has been suggested that upon increasing temperature, the HNC$^-$–counterions reduced the binding tendency onto CTAB micelles [94, 95, 106]. This induced weakly bound counterions to desorb from the micelles and release into solution. Hence, the wormlike micellar surface charge is reduced, therefore leading to a growth of cylindrical micelles with increasing tem-

perature. Further, Hassan *et al.* [94,95] reported that strong hydrophobicity (e.g., SHNC) induces high stability of micelles toward temperature. Narayanan *et al.* [113] reported that in equimolar $CTA^-$–HNC micellar solutions, vesicle evolved into wormlike micelles by increasing temperature. They suggested that $HNC^-$–counterions remained bound onto the micellar surface at low temperature. The low surface charge lead to the formation of vesicles. However, at high temperatures, they suggested a desorption of $HNC^-$–counterions from the vesicles, inducing an increased charge and thereby a transition from vesicles to wormlike micelles [113]. Verma *et al.* [92] also reported that for a given surfactant to hydrotrope ratio, an increase in entanglement density does not alter the microstructure significantly.

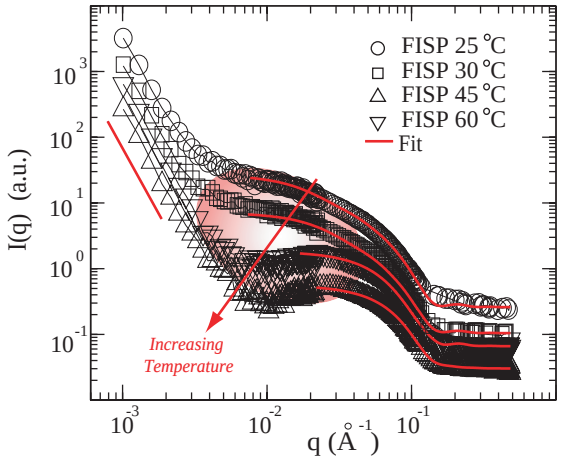


Figure 4.7: SANS spectra of the FISP at different temperatures. At low-$q$ the structure of the FISP is not affected by increasing temperature. At low-q we used a power law fitting for the FISP structure and found an index power of ∼3.5±0.05. At high-$q$ and for the temperatures of 25 °C, 30 °C and 45 °C, we fitted the FISP's spectra to a cylinder model. The length (L) of the wormlike micelles become shorter by increasing temperature, L=25 nm (25 °C), L=19 nm (30 °C) and L=17 nm (45 °C). Whereas, the radius maintained constant at ∼2.4 nm for the three temperatures. At 60 °C and high-$q$, the best fit was obtained by using a sphere model. The radius obtained from the fit was ∼3.0 nm.

### *4.7 Localized temperature behavior of the FISP*

We have built a gold-microcheater (see materials and methods section) to study the localized behavior of the FISP at different temperatures (see Fig. 2.1). We formed the FISP at room temperature, once sufficient amount of FISP was generated and located onto the

microheater, we increased the temperature and observed the behavior of the FISP at 25, 30, 45, and 60 °C (see Fig. 2.1 (B)). We recorded videos of the FISP at higher temperatures by using a magnification of 100×/1.30 oil objective with a 1.5× tube lens. Qualitatively, we did not observed any change in the FISP structure from 25 °C to ∼45 °C. We observed the breaking, but not complete melting, of the FISP structure at ∼47±1.5 °C, noticing that precursor droplets started to appear inside the FISP structure. Fig. 4.8 exhibits snapshoots of the structural evolution of the FISP at ∼47±1.5 °C. The white stars in Figure 4.8 highlight some precursor droplets formed in the FISP structure. We observed a constant cycle of formation-disintegration of precursor droplets inside the FISP's structure for long periods of time (> 10 hours), nevertheless, we did not observed a complete disintegration of the FISP. Further, the cycle formation-disintegration of precursor droplets inside the FISP was also observed at ∼60 °C with no complete disintegration of the FISP structure either. The breaking behavior observed from the microheater might be correlated to the SANS spectra of the FISP at 45 °C and 60 °C. The formation of precursor droplets inside the FISP at high temperatures (precursor at 45 °C→short wormlike micelles and precursor at 60 °C→spherical micelles) might induce the changes in the FISP's spectra at high-$q$. It is important to mention that we attempted to perform two point microrheology of the FISP at high temperature to correlated the SANS spectra of the FISP with the rheological properties of the FISP. However, the constant formation of precursor droplets inside the FISP structure at high temperatures induced motion in the tracer particles, making the motion of the tracer particle no more thermal induced. Hence, the principle of passive micrhorheology is violated, then, the rheology of the FISP obtained from two point passive microheology would be incorrect.

### *4.8 Microstructure of the FISP*

Based on higher contrast SEM and TEM images (see Fig. 4.9), the thickness and length of the micellar bundles range between ∼10–300 nm and ∼80-400 nm respectively, indicating that a single micellar bundle consists of several individual wormlike micelles. From the TEM images, we obtained that the diameter of the wormlike micelles in the FISP has a value of ∼4±0.9 nm, being in good agreement with the wormlike micellar diameter obtained from

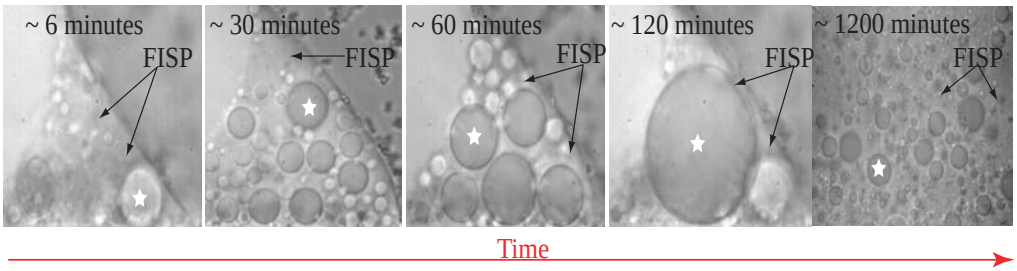


Figure 4.8: Inside of the FISP structure the formation of precursor droplets begins to occur at ∼47± °C. The most notorious precursor droplets are formed after ∼6 minutes. A cycle of formation and breaking up of precursor droplets is observed for long periods of time. No complete disintegration of the FISP was observed even after ∼1200 minutes.

SANS studies (∼4.8 nm). The existence of ionic micellar bundles was possibly related to the electrostatic interactions from the counter-ions present in the ionic surfactant solution [64,135]. Barentin and Liu [135] proposed that electrostatic attractions could lead to micellar bundles formation from an ionic surfactant solution. They showed that the energy required to form micellar bundles was linearly dependent on the thickness of the bundle and the micellar bundles might be a metastable phase in the micellar solution. Barentin and Liu also proposed that the shear induced structures [4] may be formed by micellar bundle networks. We observed two distinct structural domains in the FISP structure. Fig. 4.9 (top row) exhibits highly entangled and multiconnected micellar bundles, similar to the structure observed by Cardiel *et al.* [167] for NaSal based FISP. However, we also noticed a more ordered structure with well defined circular pores (see Fig. 4.9 bottom row). Fig. 4.9 (D) is an SEM image showing a region with the well ordered FISP structure. Fig. 4.9 (E&F) are TEM images showing well difined circular pores (micellar loops) in the FISP. The micellar loops ranges from 10 nm to 40 nm. The determination of the mesh size ($\xi$, diameter of the micellar loops in the FISP) in wormlike micellar structures has been extensively studied. Shikata *et al.* [10] proposed that the elasticity of an aqueous wormlike micellar solution of CTAB/NaSal was originated from the excessive entropy caused by the orientation of some micellar chains between entangled points. This mechanism is similar to those observed in the concentrated rubber systems [84]. Assuming a Gaussian distribution of the wormlike micelles, rubber elasticity relates the elastic modulus and the thermal energy

to the hydrodynamic correlation length (or the network mesh size $\xi$) as follows:

$$\xi^3 = \frac{k_B T}{G_0}. \tag{4.5}$$

$G_0$ was obtained from the microrheology of the FISP data.

The estimated ($\xi \approx 70$ nm) from equation 4.5 and the mesh size obtained from TEM images ($\xi^* \approx$10-40 nm) are around the same order of magnitude, despite the error introduced from the TEM sample preparation, artifacts and system errors.

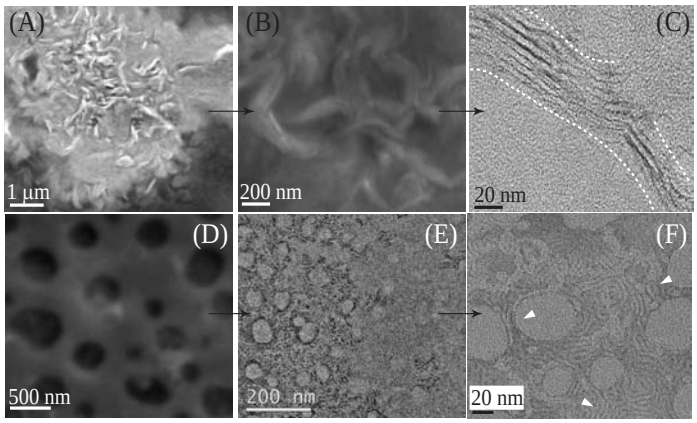


Figure 4.9: (a&b) SEM images of the FISP showing highly entangled micellar bundle-like structures. (c) TEM image of one of the bundles observed in (b). The bundle is formed by individual wormlike micelles with diameter ∼5 nm. (d) SEM image of the FISP exhibiting mesh-like micellar structures with pore wide range of pore size (∼50–800 nm). (e&f) TEM images of one of the regions observed in (d), (e&f) presents the formation of bundle-like micellar loops. The diameter of the loops ranges on 10–50 nm with a bundle-like diameter of ∼20 nm.

Horbaschek *et al.* [91] and Abdel-Rahem *et al.* [86] studied microstructures for equal molar 100 mM CTAB and SHNC system, they observed densely packed vesicles and multi-lamellar vesicles with 100 – 800 nm in diameter and 60 nm in thickness under FF-TEM electron micrograph, where some of the vesicles can reach up to a diameter of $\sim 20\mu$m. They proposed that since SHNC behaves similar to anionic surfactant but with a shorter tail, the mixture at equal molar concentration with cationic surfactant are able to form bilayers and vesicles [104]. In addition, the excess salt ions ($Na^+$ from SHNC) shield the charge of the bilayers and screen the charges between vesicles. As a result, smaller vesicles collapse and

form thick precipitates with larger dimensions. We are not necessarily claiming vesicles formation in the FISP, but similar argument can apply: the closely packed microposts induces concentration fluctuations in the precursor under flow, where $HNC^-$ penetrated into CTAB micelles and the $\pi$–$\pi$ and cation–$\pi$ interactions come to play between adjacent micelles, as a result, formation of circular porous bilayer structures are induced. Due to the screening effects of the free salt ions on the charges between bilayers, smaller pores collapse with each other and end up with a widely range size distribution. Additionally, since we are in the semi-dilute region with excess amount of CTAB, which has been reported to reverse the screen effects by positively charging the micelles, the majority of the micelles still exhibit as bundles and form branched micellar networks reported previously.

### *4.9 Comparison between NaSal based FISP and SHNC based FISP*

Notice that with very similar CTAB concentration (50 mM in CTAB/NaSal system, 45 mM in CTAB/SHNC system) and the same salt/surfactant ratio (R = 0.32), two precursor systems show distinguish rheological behaviors. The $\eta_0$, $\lambda_{\text{eff}}$ and $G_0$ in 45 mM CTAB/SHNC are all one order of magnitude higher than 50 mM CTAB/NaSal system [167]. Further, the SHNC precursor exhibited pronounced shear thinning behavior, whereas, the NaSal precursor showed shear thickening response [167]. Compared with NaSal, SHNC serves as a much stronger hydrotropic salt with naphthalene rings by $Sal^-$ ions, in which case, the surface activity of CTAB micelles is greatly reduced from decreased spontaneous curvature of micelles, accompanied by strong binding affinity naphthalene structures $\pi - \pi$ between $HNC^-$ s and interactions between adjacent hydrophobic cation groups in CTAB and $HNC^-$ (cation - $\pi$).

Despite the difference in precursors, we are able to produce highly viscoelastic flow induced structures (CTAB/NaSal FISP ($FISP_{NaSal}$) and CTAB/SHNC FISP ($FISP_{SHNC}$)) from both weakly viscoelastic precursors CTAB/NaSal and CTAB/SHNC respectively by using microfluidics approach. However, we noticed that even though the plateau modulus $G_0$ is close for both system (11 Pa for $FISP_{SHNC}$ and 15 Pa for $FISP_{NaSal}$), the $\eta_0$ and $\lambda_{\text{eff}}$ are larger in $FISP_{NaSal}$ than $FISP_{SHNC}$ (see Table 2). Previously, we showed that $FISP_{NaSal}$ mainly consists of branched and entangled micellar bundles, with a diameter of

$\sim$ 100$\pm$15 nm and a length of $\sim$ 350$\pm$45 nm, with a mesh size $\xi \sim$ 70$\pm$13 nm. In the FISP$_{SHNC}$, not only similar structures of highly intertwine micellar bundles were observed (see Fig. 4.9 (a&b)), there were also large amount of mesh-like micellar bundle loops formed in the FISP$_{SHNC}$ (see Fig. 4.9 (e&f)). Based on EM images, the miecellar networks has a wide range size distribution $\sim$500 – 800 nm, the diameter of the bundle loops ranges on 10–40 nm with a bundle width of $\sim$20 nm.

| Materials | $\eta_0$ (Pa·s) | $\lambda$ (s) | G$_0$ (Pa) | $\xi^* = \nu^{*-1/3}$ (nm) |
|---|---|---|---|---|
| FISP$_{SHNC}$ | 3.1$\pm$0.26 | 0.28$\pm$0.08 | 11$\pm$3.3 | 10 – 40 |
| FISP$_{NaSal}$ | 13$\pm$5.0 | 0.86$\pm$0.20 | 15$\pm$8.0 | 80$\pm$21 |

Table 4.2: The longest relaxation time $\lambda$, plateau modulus G$_0$, and the zero-shear viscosity $\eta_0$, mesh size $\xi^*$ from TEM, ($\nu^*$ represents degree of entanglement of the FISP) for FISPs made in CTAB/SHNC and CTAB/NaSal system

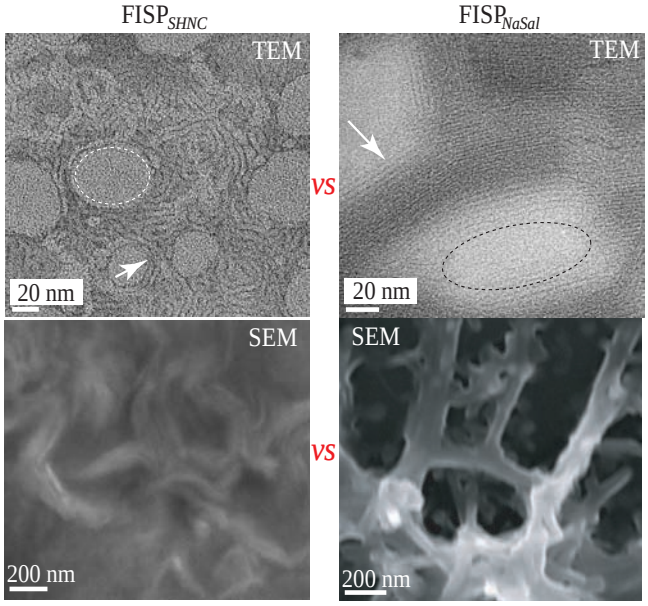


Figure 4.10: First column, TEM and SEM image of the FISP$_{SHNC}$ showing micellar loops (TEM) and highly entangled micellar bundles (SEM). TEM and SEM images of the FISP$_{NaSal}$ presenting micellar bundles.

### *4.10 Conclusions*

In summary, we observed the formation of stable micellar network (FISP) by using a $\pi - \pi$ hydrotropic organic salt (SHNC), by simply tuning flow conditions and micro-spatial confinement under room temperature. We proposed that the formation of FISP follows the same mechanism by that suggested by Cardiel *et al.* [167], where spatial confinement from the micropost array, entropic and local micellar fluctuations in the micropost array induces the formation of branched micellar networks. We noticed that the precursor exhibits flow birefringence, however, we did not observe birefringence response in the FISP. We implied that the thickness and high entanglement micellar density of the FISP are the reasons to not observe birefringence behavior in the FISP. The rheological properties of the FISP are larger than those of the liquid precursor. We observed that the FISP can coexists at relatively high temperatures (30, 45, and 60 °C) by using SANS. However, we noticed that the structure of the FISP begins to re-organize at temperature ∼47 °C by the formation of precursor droplets inside the FISP structure. Nevertheless, we did not observe a complete disintegration of the FISP at high temperatures. We also showed that a weakly viscoelastic micellar precursor could transition to more viscoelastic micellar network structure. The zero shear viscosity of the precursor is around one order of magnitude smaller than that of its FISP. This rheological variation can be correlated with the microstructural evolution from semidiluted wormlike micelles to an entangled and multi-connected micellar network, FISP.

# Chapter 5

# NON-IONIC FLOW-INDUCED STRUCTURED PHASE (NI-FISP)

## *5.1 Introduction*

Although some nonionic surfactant solutions can form wormlike micelles [34–45], the majority of studies have focused on ionic surfactant solutions [4,123]. In views of biomedical as well as biotechnological applications, nonionic micellar solutions are preferred over ionic surfactant systems due to their electrolyte-free environment, biocompatibility, and less eco-toxic properties. The nonionic surfactant solution used in this work contains polyoxyethylene(20) sorbitan monooleate (Tween-80) and co-surfactant monolaurin (ML). Polyoxyethylene(20) sorbitan monooleate (Tween-80) is an amphipathic, nonionic surfactant composed of fatty acid esters of polyoxyethylene sorbitan, which is frequently used in protein biopharmaceutical formulations and cosmetic industries [124–126]. For example, Tween-80 based carrier delivered substantial tocopherols and carotenoids simultaneously without any damage to human colonic adenocarcinoma (CaCo-2) cells [127]. Radomska *et al.* [128] reported that Tween-80 was able to emulsify retinol and retinol esters in an ocular drug preparation, with stability up to 6 months at 20 °C. In addition, it has been well documented that the binary and ternary mixture of Tween-80 with other co-surfactants showed a synergistic effect on lowering the critical micelle concentration (CMC), improving its solubility and surface activity as well as modifying its viscosity compared to individual Tween-80 solutions [129–131]. For example, the aqueous mixture of Tween-80 and nonionic co-surfactant Brij30 was shown to be more effective in forming isotropic dispersion and liquid crystalline structures than the mixture of Tween-80 and Brij58 in water. Brij30 is a smaller molecule which can coexist in Tween-80 molecules, favoring micellar aggregation [131].

Recently, Varade *et al.* [34] studied the viscoelastic properties of wormlike micelles in Tween-80 solution with trioxyethylene alkyl ether ($C_mEO_3$, $m = 12, 14, 16$) by performing bulk shear rheometry and small-angle X-ray scattering (SAXS) measurements. By

fixing the concentration of Tween-80 (15 wt%) and varying the weight fraction $\chi$ ($\chi$ = $C_mEO_3$/($C_mEO_3$+Tween-80)), they observed that the zero shear viscosity $\eta_0$ and plateau elastic modulus $G_0$ of their nonionic micellar solutions increased by increasing $\chi$; however, as $\chi$ reached a critical value, the $\eta_0$ and $G_0$ started to decrease. This non-monotonic changes in $\eta_0$ and $G_0$ were caused by the microstructural transition from linear to branched wormlike micelles [6,81]. Varade *et al.* [34] also observed that micellar growth could be enhanced by increasing temperature with fixed surfactant concentrations.

Monolaurin, a lipophilic surfactant, is the most powerful antiviral and antibacterial fatty acid found in coconut oil. It has been reported that the addition of the monolaurin (ML) facilitates the formation of nonionic wormlike micelles [39, 40]. The incorporation of ML decreases the effective area of micelles, thus reducing the interfacial curvature of the micelles, yielding further micellar growth [39, 40]. Sharma *et al.* [39] showed that wormlike micelles could be formed by adding ML to Tween-80 in an aqueous solution. By fixing the concentration of Tween-80 at 25 wt% and varying the weight ratio $\chi$ ($\chi$ = ML/(ML+Tween-80)) from 0.0 to 0.16, they observed shear thinning behavior when $\chi > 0.085$. They suggested that the shear thinning response was correlated with the ordered micellar structures formed in the nonionic micellar solutions. Sharma *et al.* [39] also noticed that the rheological properties $\eta_0$, $G_0$, and stress relaxation time $\lambda_{\text{eff}}$ of their micellar solutions increased by increasing $\chi$, reaching a maximum around $\chi \sim 0.12$. They attributed these rheological property changes to the transition from linear wormlike micelles to multi-connected micellar networks in the solution. Sharma *et al.* [40] also studied the nonionic wormlike micelles formed from aqueous mixtures of polyoxyethylene phytosterol ($PhyEO_{30}$) with ML, focusing on the temperature effect. Fixing the concentration of $PhyEO_{30} = 10$ wt% while varying the weight ratio $\chi$ from 0.0 to 0.29, they observed that micelles became shorter when the temperature increased to 45 °C, with cross-links formed in the micellar solution. They also noticed that the $\eta_0$, $G_0$, and $\lambda_{\text{eff}}$ increased when the temperature increased from 35 °C to 45 °C. The initial increase of $G_0$ was correlated with the increase in micellar network density. $G_0$ started to decrease after the temperature reached around 70 °C, due to the shortening of the wormlike micelles at high temperatures. Meanwhile, the $\eta_0$ decayed after the temperature went beyond 45 °C, related to the formation of micellar cross-links with high

fluidity. Sharma *et al.* [40] argued that high temperature would decrease the spontaneous curvature in their micellar solutions and increase the energy cost to form hemispherical end-caps, which would favor one dimensional micellar growth, and finally leading to the formation of micellar networks. Sharma *et al.* [36] also reported the formation of wormlike micelles and their viscoleastic properties in an aqueous solution consisting of sodium dodecyl trioxyethylene sulfate (SDES) and ML. When the ML concentration reached a critical value, $\eta_0$ of the solution started to decline, which is related to the formation of wormlike micellar junctions where the micellar junctions could slide against each other, yielding to high fluidity in the micellar solution. Sharma *et al.* also showed a monotonic increase of $G_0$ as a function of temperature and related the increase of $G_0$ with an increase in the entanglement density of wormlike micelles. Similar argument was proposed for ionic micellar solutions with high salt concentrations [6, 81].

### *5.2 Flow-induced structures*

Microstructural transitions of nonionic micellar solutions have been mostly studied under temperature and surfactant concentration changes, under quiescent conditions [34–42,44,45]. However, transient and permanent micellar structures under flow have been extensively studied for ionic surfactant solutions. Transient ionic micellar networks were first reported by Rehage and Hoffman [3], where an ionic wormlike micellar solution formed a gel-like structure under shear flow above a critical shear rate. They referred to this gel-like material as shear-induced structured phase (SIS), because upon cessation of the flow, the structure would disintegrate. The appearance of SIS has been correlated with the increase of shear viscosity in wormlike micellar solutions [24]. Furthermore, the structure of SIS has been associated with the formation of micellar bundles [24], birefringence, and fluctuating local micellar concentration [13].

Vasudevan *et al.* [30] first reported permanent gel-like micellar structures from a semi-dilute ionic wormlike micellar solution. The precursor containing cetyltrimethylammonium bromide (CTAB) and sodium salicylate (NaSal) formed a stable *flow-induced structured phase* (FISP) after the precursor flowed through a microfluidic tapered channel packed with glass beads (20-100 $\mu$m in diameter). It is believed that this irreversible "gel-like"

FISP occurs from a combination of the high rates of strain ($\dot{\epsilon} \sim$ 5,000 $s^{-1}$) and from the extensional characteristics of the flow [30, 47, 48]. The FISP maintained stable for more than a year, at temperature $\sim$23$\pm$2 °C subsequent to the cessation of the flow. More recently, Cardiel *et al.* [167] reported the formation of FISP in both ionic shear thinning and shear thickening wormlike micellar solutions in a microfluidic device containing microspost arrays. The electron microscopy shows that the FISP consists of highly entangled, branched, and multi-connected micellar bundles. They proposed that the high stretching and flow alignment in the micropost enhanced the flexibility and lowered the bending modulus of the wormlike micelles. As flexible micelles flow through the microposts, it becomes energetically favorable to minimize the number of end caps while concurrently promoting the formation of cross-links.

Of note is that the transient flow-induced structures has only involved shear flows. In contrast, the flow which results in irreversible structure formation such as FISP has both shear and extensional flow components and the rates of strain are generally several orders of magnitude larger than those in the shear flows. To our best knowledge, permanent gel-like nonionic micellar structures formed at room temperature and relatively low surfactant concentrations have not been reported. In this paper, we showed that a nonionic flow induced structured phase (NI-FISP) could be formed from a nonionic micellar solution (an aqueous solution with nonionic surfactant Tween-80 and ML) by using a microfluidic device consisting of hexagonal micropost arays. We studied the bulk shear rheology and the microrheology of its corresponding NI-FISP. Additionally, the microstructures of the precursor and its NI-FISP were characterized by small-angle neutron scattering (SANS) measurements, transmission electron microscopy (TEM) and cryo-electron microscopy (cryo-EM). We observed highly entangled and multi-connected micellar networks and closed-looped micellar bundles in the NI-FISP. The nontoxic, biodegradable, nanoporous structures created by Tween-80/ML mixture provides a promising scaffold platform for applications in biosensing and drug delivery [125–127].

### *5.3 NI-FISP formation*

Once the nonionic precursor passed through the micropost arrays at a constant flow rate of 15 mL/h, the NI-FISP began to emerge. Even though NI-FISP can be formed under a wide flow rate range (5-30 mL/h), a constant flow rate of 15 mL/h was used here to be consistent with the experimental conditions employed in our previous work with ionic wormlike micellar solutions [167] for future comparison purposes. Fig. 5.1 (a) shows schematics for the NI-FISP formation. Fig. 5.1 (b) shows the actual device with finger-like NI-FISP. Fig. 5.1 (c) is a cryo-EM image of the NI-FISP, exhibiting entangled, branched, and multi-connected networks. The PDMS-glass microfluidic device has a channel height of 75 $\mu$m and a width of $\sim$1260 $\mu$m, containing hexagonal arrays of microposts with diameter 100 $\mu$m and spacing of 15 $\mu$m. At a flow rate of 15 mL/h, we estimate a maximum rate of strain of $\dot{\gamma}_{\text{total}} \sim 3.7 \times 10^4\,\text{s}^{-1}$ and a total strain in the arrays of $\gamma_{\text{total}} \sim 2114$. Modeling wormlike micelles under extensional flow, Turner and Cates [63] predicted a critical extension rate where the solution could undergo a transition to a "gel" phase consisting of extremely long aligned micellar chains. They assumed a simple reaction scheme in which two micelles fuse only if they are collinear. This gel phase only persists while the flow is active. On the basis of their model, for wormlike micelles with length $\sim$30 nm, a critical strain rate of $\sim 10^3$ s$^{-1}$ is required for extensional flow-induced gelation. This strain rate has the same order of magnitude as the one present in our micropost array ($\dot{\epsilon}_{\text{ext}} \sim 3.0 \times 10^3\,\text{s}^{-1}$). The comparisons described above indicate that high extension rates and spatial confinement are critical for the NI-FISP formation.

We propose that the potential mechanism to form NI-FISP is similar to that of the ionic FISP formation [167] (Figure 1 (A)). Even though the electrostatic interactions are absent in the nonionic precursor, the formation of the NI-FISP is enabled by the spatial confinement, high strain rates ($\sim 10^4$ s$^{-1}$), and entropic fluctuations generated in the micropost arrays. Our nonionic precursor contains primarily spherical micelles, with small amount of wormlike micelles (see cryo-EM image in Figure 3(A)). When the precursor flew through the micropost array, the high stretching and flow alignment could fuse the spherical micelles to form larger spherical micelles and wormlike micelles. The structural transition from spherical mi-

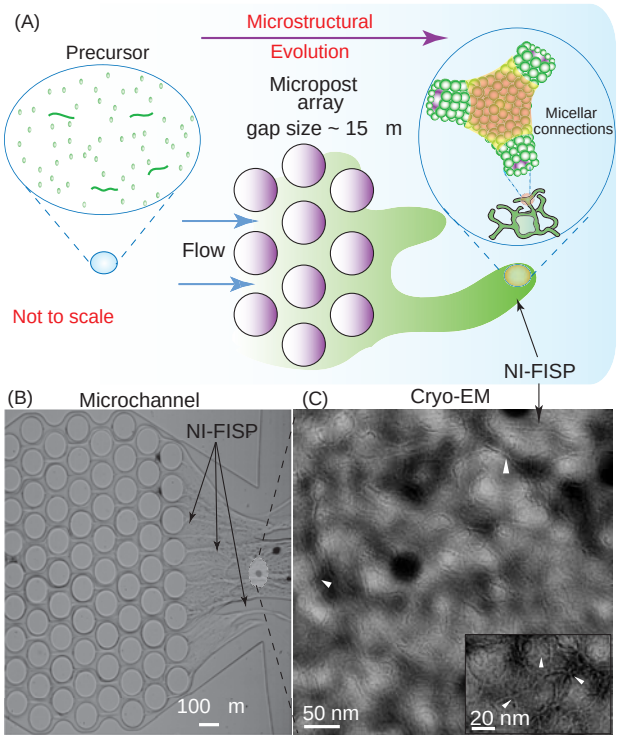


Figure 5.1: (a) Schematics of the hexagonal micropost array. When the precursor passes through the micropost array it undergoes high strain rates of $\sim 3.7\times10^4\ s^{-1}$ and total strain $\sim 2.1\times10^3$, leading to the NI-FISP formation. (b) A snapshot showing the finger-like NI-FISP formation after the precursor passing through the micropost array. (c) A cryo-EM image of NI-FISP showing entangled and multi-connected micellar network; the white triangles highlight the micellar connections. The inset in (c) shows the "three-fold" junctions in the NI-FISP.

celles to wormlike micelles has been investigated in both nonionic surfactant and polymer solutions [132, 133]. Rharbi *et al.* [132] studied the structural transition in nonionic Triton X-100 solutions by using a combination of T-jump experiments, stopped-flow fluorescence time-scan measurements, and light scattering techniques (DLS). They suggested that two spherical micelles could fuse to form a super-micelle with sufficient activation energy. Landazuri *et al.* [133] studied the structural transition from spherical to rodlike micelles in a pluronic triblock copolymer by using T-jump and DLS experiments. They concluded that the spherical micelles could evolve into rodlike micelles due to random fusion fragmentation (RFF) mechanism, in which spherical micelles can fuse with other micelles independent of their sizes and can break into two micelles of any size. For the nonionic precursor, we spec-

ulate that the high rate of strain and the micro-spatial confinement provide the activation energy to induce both sphere-to-wormlike and super-micelles transitions at room temperature. In addition, the small amount of wormlike micelles in the precursor can also act as nucleus to form longer wormlike micelles during the flow. The spatial confinement and high strain rates from the microposts can stretch the wormlike micelles and make them more flexible with lower bending modulus. Hence, the free energy of surfactant molecules in the end-cap increases relative to the curvature energy in the cylindrical body of the micelle, lowering the work required to form junctions (see Fig. 5.1 (a)) [1, 41–43, 67]. Further, the spatial confinement in the micropost array also promotes local concentration fluctuation of micelles, shown in our recent studies [48] and suggested in previous work [13]. As a consequence, it becomes energetically favorable for flexible adjacent wormlike micelles to fuse when they flow through the micropost array, promoting the formation of cross-links, and finally, leading to micellar networks [10, 41, 67, 69].

Drye and Cates [67] developed a theoretical framework based on Flory-Huggins-type theory formulated for living rigid-rod networks. Their model described the formation of cross-links and multi-connections in wormlike micellar solutions under equilibrium by assuming the end-cap energy being much higher than the energy required to form micellar cross-links. They predicted that unsaturated wormlike micelles, with no connections or cross-links, could evolve into cross-linked or multi-connected wormlike micellar structure under entropic fluctuations. May *et al.* [134] developed a molecular model to predict the free energy in micellar networks, where the contributions of the head-group repulsion forces of the surfactant, the hydrocarbon-water interfacial energy, and the chain conformational free energy of the surfactant were taken into account. They concluded that the micellar branches (e.g., three-fold junctions) were energetically unfavorable but may appear as a metastable structures. However, their model accounted for the electrostatic interactions due to the surfactant head-group charges, which is absent for our nonionic solutions. Dealing with nonionic micellar systems, Dan and Safran [42] predicted how nonionic cylindrical micelles could form branched structures for alcohol ethoxylate surfactants. These amphiphiles with small molecules are usually denoted by $C_iE_j$, where $(i, j)$ defines the number of monomer units in the tail and the head of the surfactant monomer. For a given solvent and system

conditions, the spontaneous curvature is dependent on the ratio of $i$ to $j$, since it determines the relative packing areas of micelles. Low values of $i/j$ indicate relatively large head groups, high spontaneous curvature and a tendency to form spherical micelles [42]; while higher $i/j$ leads to the formation of flatter structures such as bilayers. A mixture of spherical micelles and bilayers can also induce cylindrical micelle formation [44]. Dan and Safran proposed that cylindrical micelles could exhibit two topological defects: end-caps (related to translational entropy) and branch junctions (related to configurational entropy), where the overall entropy gain associated with end-caps is greater than that from branching points. They further related these topological defects to the spontaneous curvature of nonionic amphiphilic molecules and concluded that low spontaneous curvature favored branching formation and network structures. Dan and Safran also demonstrated that the spontaneous curvature of $C_iE_j$ system could be tuned by temperature, with branched structures preferred at high temperatures, where the spontaneous curvature is lower [42]. Tlusty and Safran [43] also reported that the structural evolution (from wormlike micelles to branched micelles) of nonionic micellar solutions would only occur when the curvature energy of the end-caps is similar to the curvature energy of the branches. Safran and co-workers [41–43] concluded that the branching formation in a nonionic surfactant was controlled by a complex balance among mixing entropy at molecular levels, entropy of the topological defects (end-caps and branches), and curvature energy associated with the defect geometry. Note that in Safran *et al.* 's work, the transition from wormlike micelles to branched micelles was enabled by increasing temperature under equilibrium conditions.

Relating Safran and co-workers' argument, the presence of spatial confinement and the flow kinematics in our microfluidic device promotes entropic fluctuations in the nonionic precursor solution even at room temperature, making it easier for the micelles to cross the energy barrier between states and, thus, increasing transition frequencies between states, enabling the formation of entangled and branched micellar networks (NI-FISP) [10, 41–43, 67, 69].

### *5.4 Rheometry of the precursor and NI-FISP*

The rheological properties of the precursor and its corresponding NI-FISP were characterized by a combination of bulk rheometry and microrheometry. The precursor solution shows slightly shear thinning behavior. Fig. 5.2 (a) shows the plot of shear viscosity versus shear rate of the precursor. The zero shear viscosity of the precursor has a value of $\eta_0 = 0.1 \pm 0.02$ Pa·s. Since the spherical micelles could fuse to induce wormlike micelles formation under flow, wormlike micelles can be subsequently aligned in the direction of the flow, forming shear induced structure (SIS) [24]. The slight shear thinning behavior observed beyond $\dot{\gamma}_c \sim 700\ \mathrm{s}^{-1}$ can be contributed to the SIS disintegration at higher shear rates [4, 41, 42, 123].

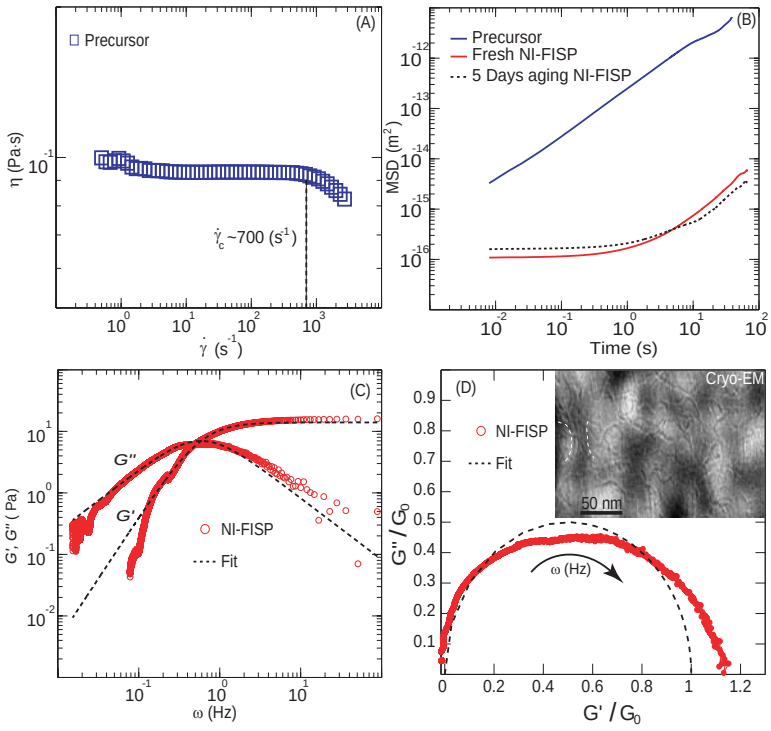


Figure 5.2: (a) Shear viscosity versus shear rate for the precursor solution. (b) Mean square displacement (MSD) of the tracer particles in the precursor and its corresponding NI-FISP (fresh and 5-days old). The MSD of the precursor (blue line) exhibits linear, viscous behavior. The MSD of the NI-FISP (red-dash line) shows the non-linear viscoelastic response. (c) Linear viscoelastic response of the NI-FISP measured from microrheometry. The data is plotted against the dotted curves from single mode Maxwell fit. (d) Cole–Cole plot of the NI-FISP. The black semi-circle curve corresponds to the single mode Maxwell fit; the inset in (d) is a cryo-EM image of the NI-FISP, showing highly entangled, branched and multi-connected micellar network.

| Materials | $\eta_0$ (Pa·s) | $\lambda_{\text{eff}}$ (s) | $G_0$ (Pa) |
|---|---|---|---|
| Precursor | 0.1±0.02 | – | – |
| NI-FISP | 8.6±4.3 | 1.2±0.8 | 7.2±3.0 |

Table 5.1: Rheological properties of the precursor and NI-FISP.

As the NI-FISP was produced in the microdevice, the resulting volumes were relatively small, hence, the rheological properties of NI-FISP were measured by using passive microrheology. To make passive microrheology technique work, the probe particle size needs to be larger than the mesh size of a given sample. Our probe particle's diameter is 1 $\mu$m, which is larger than the mesh size of all the precursor and the NI-FISP solutions from the TEM and cryo-EM measurements. Since NI-FISP is somewhat heterogeneous based on the cryo-EM images, we selected probe particles at different locations within the same NI-FISP sample to obtain the averaged MSD. Each video contains at least 10 probe particles per NI-FISP sample. The microrheology results shown below are based on the averaged MSD values. Fig. 5.2 (b) shows the MSD of the precursor and its corresponding NI-FISP. In a viscous fluid the MSD of tracer particles grows linearly with time. However, in a viscoelastic fluid the MSD follows a non-linear behavior with respect to time, as shown for NI-FISP because the displacement of tracer particles is limited by the elastic component of the fluid. Fig. 5.2 (c) plots the elastic modulus $G'$ and viscous modulus $G''$ versus the frequency $\omega$ for NI-FISP. The microrheology data was further fitted to a single-mode Maxwellian linear viscoelastic model. The black-dash line follows the Maxwellian fit while the red-circles correspond to the experimental data. The noise at low frequencies is caused by some probe particles coming in and out of the focus plane during the recording process [51]. From these experimental data, we obtained the value of the plateau modulus $G_0$ and the stress relaxation time $\lambda_{\text{eff}}$ of the NI-FISP ($\lambda_{\text{eff}}$ is the inverse of the frequency value where the crossover between G′ and G″occurs). Finally, we approximated the zero shear viscosity of the NI-FISP by using $\eta_0 = G_0 \times \lambda_{\text{eff}}$ [84], with $G_0$ = 7.2±3.0 Pa, $\lambda_{\text{eff}}$ = 1.2±0.8 s, and $\eta_0$ = 8.6±4.3 Pa·s (see details in Table 1).

The rheological data of NI-FISP was also presented in the Cole–Cole plot with normal-

ized ($G'/G_0, G''/G_0$), see Fig. 5.2 (d). By conducting numerical simulation and employing a Poisson renewal model, Cates *et al.* [77,78] proposed that if a wormlike micellar solution follows a semi-circle in a Cole–Cole plot, the solution should follow a single exponential stress relaxation process. However, if the micellar solution exhibits a flattened curve in the Cole–Cole plot, a broad distribution of stress relaxation times incur where the internal micellar dynamics maybe dominated by reptation processes or Rouse breathing mechanism. With branched and multi-connected micellar network in NI-FISP, NI-FISP (red circles ∘) fit the semi-circle reasonably well in the Cole–Cole plot with a mean squared error of $\sim 15\%$, with some deviation at higher frequency. Similar deviation at higher frequency had been reported for nonionic micellar solutions [34, 35, 39]. The rheological properties of wormlike micelles have been reported to depend on the micellar volume fraction in the entangled regime [4], in which the scaling laws are valid. The scaling rules for dilute and semi-dilute micellar solutions show that $G_0 \approx \phi^{2.3\pm0.2}$, where $\phi$ is the surfactant volume fraction [**?**]. However, Candau and Oda [142] reported that for saturated micellar networks with no salt, the scaling rules broke down due to the presence of cross-links and sliding connections in the micellar network. As a result, $G_0 \approx \phi^{1.5}$ in wormlike micelles with saturated networks.

In our precursor, with 25 wt% Tween-80 and density $\rho = 1060$ kg/m$^3$, the volume fraction of the surfactants is $\phi \approx 0.24$. By applying the scaling rules for dilute micellar solutions [2], we obtain $G_0 \approx \phi^{2.3} \approx 0.03$ Pa. This estimate is consistent with the bulk rheology and microrheology measurements of the precursor, where the viscous response is dominant. Moreover, if we use the scaling rule proposed by Candau and Oda [142] ($G_0 \sim \phi^{1.5}$) for saturated networks with no salt, at the volume fraction of $\phi = 0.24$, $G_0 \approx 0.11$ Pa, which is lower than the microrheology data we obtained for NI-FISP ($G_0 = 7.2 \pm 3.0$ Pa). We speculate that the discrepancy between our microrheology measurement and the scaling rule prediction is due to the highly entangled and branched microstructures present in the NI-FISP. The increase in the entanglement density in the NI-FISP, evidenced by the cryo-EM images (Fig. 5.4B) increases the value of $G_0$.

It is worth noting that the true value of the elastic modulus of the NI-FISP might be higher than 7.2±0.3 Pa. Fu *et al.* [210] reported that microrheology techniques tended to under-estimate the elastic modulus in polymer networks. They studied the effects of

slip condition and compression effects on the tracer particle used in the microrheology. When the sliding condition and compression effects are present at the same time, the elastic modulus in the polymer networks can decrease ∼43% from the true value. Further, they observed that at low frequencies (< 1 rad/s), the discrepancy between the bulk rheology and microrheology could be caused by the sliding and compression effects. Our nonionic precursor is highly lipophilic where the presence of the sliding condition might have some effects on the tracer particles used. Hence, the elastic modulus reported in the present work might be lower than the true value.

In summary, we observe that a viscous micellar solution (precursor) evolves into a viscoelastic micellar solution due to microstructural changes in the micellar solutions. The zero shear viscosity $\eta_0$ of the precursor is close to two orders of magnitude smaller than that of its NI-FISP (see table 1). The rheological changes from the viscous precursor to the viscoelastic NI-FISP can be correlated with the structural evolution from spherical micelles in the precursor to a highly entangled and multi-connected micellar network in NI-FISP (see Fig.5.4).

### *5.5 SANS and USANS measurements*

We have performed SANS ans USANS in both precursor and NI-FISP. We observe a clear structural transition from the precursor to the NI-FISP in Fig. 5.3. The SANS spectra of the precursor was fitted to a spherical core-shell model with a hard-sphere structure factor [58]. Polidispersity in the radius of the micelles (∼ 0.17) was used in the fitting process. From the SANS fitting in the precursor, the micelles have a core radius of 3.3 nm and a thickness of 1.5 nm, with a total cross-sectional diameter of 9.6 nm. These values are similar to those reported by Varade et. al. [34], where the authors obtained 9 nm for the micellar cross-sectional diameter and 3.6 nm for the core diameter. The inset in Fig. 5.3 is a Cryo-EM image of the precursor. The Cryo-EM image shows dominantly spherical micelles (black dots) with radius of ∼4.5±0.7 nm. This radius is in good agreement with the radius obtained by the the SANS fitting. At $q < 0.03\mathring{A}^{-1}$ the SANS spectra of the precursor shows $q$-independent scattering (e.g., flat response) indicating no presence of large structures (e.g. wormlike micellar networks).

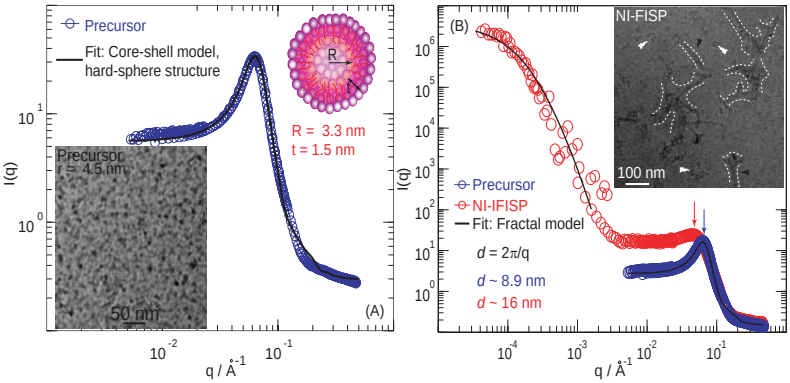


Figure 5.3: (a) SANS spectra of the precursor. The scattering of the precursor was fitted to a core-shell model with form factor for hard-spheres (solid-black line). Polydispersity ($\sim$0.17, with Gaussian distribution) in the radius of the spherical micelles was applied to fit the spectra of the precursor. From the fitting, the micelles have a core radius of 3.3 nm and thickness shell of 1.5 nm, with a total cross-sectional diameter of 9.6 nm. The inset in (a) is a cryo-EM image of the precursor. From the cryo-EM the average radius of the spherical micelles is $\sim$4.5$\pm$0.7 nm. The two techniques SANS and Cryo-EM exhibit similar cross-sectional dimensions of the spherical micelles in the precursor. (b) Combined SANS and desmeared USANS spectra of the NI-FISP. The comparison between the precursor and NI-FISP scattering. At high $q$ the NI-FISP spectra shows a shifted peak similar to that presented in the precursor. The characteristic dimension of the precursor and NI-FISP are 8.9 nm and 16 nm respectively. At lower $q$ the spectra of the NI-FISP exhibits similar scattering as those observed for gel-like materials with fibrin networks [58]. The low-q spectra was fitted to a fractal model (solid-black line). The fit yields a fractal dimension of $D_f$=2.7$\pm$0.13 and correlation length $C_l\sim$731$\pm$76 nm . $D_f$ implies the formation of networks structures. The inset in (c) is a cryo-EM image of the NI-FISP structure. The inset shows micellar network structures with dimensionS on the order of hundreds of nanometers ($\sim$ 500 nm).

The SANS spectra of the NI-FISP (red-circles in Fig. 5.3 (c)) differs significantly from that of the precursor (blue-circles in Fig. 5.3 (c)). At high $q$ the spectra of the NI-FISP shows a characteristic peak similar to that of the precursor. However, the peak of the NI-FISP is slightly shifted to a lower $q$. An estimation of the characteristic dimension in both precursor and NI-FISP can be done by using $d\sim 2\pi/q$, where $q$ is the wave-vector at which the peak occurs. For the precursor, a characteristic dimension of $\sim$ 8.9 nm was found, while the NI-FSP exhibits a characteristic dimension of $\sim$ 16 nm. This dimension variation suggests two potential scenarios: (1) the interaction distance of the spherical micelles becomes larger

after passing through the micropost, or (2) the formation of potential micellar bundles formed by 2 micelles (each micelle has $\sim$ 9.6 nm in diameter). At $q < 0.03\mathring{A}^{-1}$, the spectra of the NI-FISP begins to increase, indicating the presence of larger structures. We fitted the low-q spectra of the NI-FISP to a fractal model based on the work of Teixeira to evaluate the network scale structure of the NI-FISP [58]. This is primarily reflected in the USANS spectra ($q$<$10^{-3}$Å$^{-1}$). From the fitting, we obtained an fractal dimension ($D_f$) of 2.7$\pm$0.13 and correlation length ($C_l$) of $\sim$731$\pm$76 nm. The value of $D_f$ is representative of gel-like networks with characteristic size on the order of several nanometers ($C_l$) [58]. Our Cryo-EM images and TEM images exhibits the formation of micellar networks with dimensions of $\sim$ 500 nm. The fitting and our microscopy techniques imply the formation of micellar networks with size ranging from several nanometers to hundreds of nanometers.

The SANS data exhibit a drastic transition upon passing the precursor through the microchannel that induces the appearance of a gel-like scattering pattern at low-$q$ with large domains. However, the SANS data is not able to prove unequivocally that the NI-FISP is composed just by wormlike micelles because of the the lack of a structure factor suitable to describe the NI-FISP. Nevertheless, we were able to eliminate the possibilities that the NI-FISP was composed by spherical micelles, lamellar phases, vesicles or wormlike micelles. Assuming that the surfactant used in the present work maintains the same cross-sectional dimensions (i.e., the radius of a sphere should be approximately the same as the radius of a cylinder and the thickness of a lamellar sheet). From the precursor spectra (SANS), we obtained the cross-sectional dimension of the spherical micelles (3.3 nm for core radius and 1.7 nm for the thickness of the micelles) and fixed these dimensions to calculated the spectra of different shapes. We calculated the spectra of lamellar phases, core-shell micelles with hard-sphere structure factor, core-shell with no structure factor, spheres, vesicles, and wormlike micelles and compared those spectra with the NI-FISP's spectra at high $q$ ($q > 0.03\ \mathring{A}^{-1}$) (see supporting information). From the spectra comparison, we cannot conclude that the NI-FISP is solely composed by wormlike micelles but also we can conclude that the NI-FISP is not composed by lamellar phases or vesicles. Hence, we have to combine all the techniques (Cryo-EM, TEM, microrheology, and SANS) presented in this paper to suggest that the NI-FISP is formed by highly entangled and multi-connected

micellar networks. Our Cryo-EM and TEM images present highly entangled and multi-connected wormlike micelles. The microrheology exhibits Maxwellian viscoleastic behavior characteristic of wormlike micellar solutions [4]. The SANS data at low-wave vector shows a representative scattering pattern similar to that of gel-like structures with fibrin networks.

### *5.6 Microstructure of the precursor and NI-FISP*

We conducted extensive microstructural characterizations of the precursor and its corresponding NI-FISP, by using a combination of electron-microscopy techniques (cryo-EM and TEM). Cryo-EM imaging is desirable because it can capture the true microstructure of a given sample in its native hydrated environment. In order to avoid any artifacts in the NI-FISP's structure, we did not stain the cryo-EM samples. Whereas all the TEM samples were stained with NanoW© to improve the imaging contrast [167]. Consistent with the ternary phase diagram presented by Sharma *et al.* [39], the cryo-EM of the precursor shows largely spherical micelles with a diameter of $\approx 9.2 \pm 0.8$ nm and some wormlike micelles (see Fig. 5.4(a)). These results are consistent with our SAXS measurements and similar to the values reported by Varade *et al.* [34].

We observed very similar morphology and geometric dimensions between cryo-EM and TEM samples of the NI-FISP, indicating that the potential drying or sample preparation artifacts did not strongly alter the microstructure from the regular TEM imaging. For example, we observed micellar bundles in both cryo-EM and TEM of NI-FISP samples (see Fig. 5.4). In the cryo-EM images, the ice-layer made it more difficult to obtain high contrast features of the micellar bundles. Based on higher contrast TEM images, the thickness and length of the micellar bundles range between ∼8-30 nm and ∼30-300 nm respectively, indicating that a single micellar bundle consists of several individual wormlike micelles. We recently observed micellar bundles formed in both ionic semi-dilute micellar solution and its corresponding ionic FISP [167], with the characteristic bundle thickness 4-5 times larger than the nonionic micellar bundles reported in this work. The existence of ionic micellar bundles was possibly related to the electrostatic interactions from the counter-ions present in the ionic surfactant solution [64, 135]. Barentin and Liu [135] proposed that electrostatic attractions could lead to micellar bundles formation from an ionic surfactant solution. They

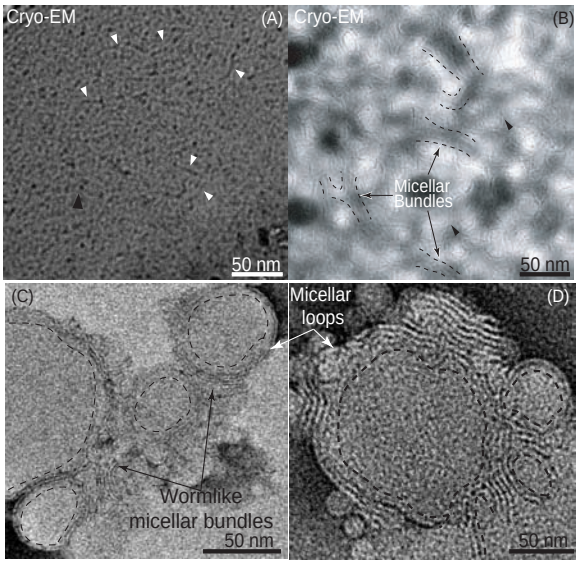


Figure 5.4: (a,b) Cryo-EM images of the NI-FISP; (c and d): TEM images of the NI-FISP. (a) shows the structure of the precursor composed of spherical micelles (black triangle) and wormlike micelles (white triangles) with diameter of ≈4.2±0.8 nm. (b) exhibits the formation of highly entangled and multi-connected micellar network; "three fold" junctions and closed-looped micelles (black triangles) are shown. (c and d) present inter-connected micellar bundles and closed-looped micellar bundles; the diameter of the micellar loops is ∼ 20-70 nm (black dash lines are guide-lines). The branches are the wormlike micellar bundles while the grey areas correspond to the pores in the structure.

showed that the energy required to form micellar bundles was linearly dependent on the thickness of the bundle and the micellar bundles might be a metastable phase in the micellar solution. Barentin and Liu also proposed that the shear induced structures may be formed by micellar bundle networks. In the present work, we only observed the formation of micellar bundles in the NI-FISP but not in the precursor solution. In addition, the micellar bundles formed in ionic FISP are usually straight due to the electrostatic attractions [135] from the charged head groups, while the bundles shown in the NI-FISP tend to be curved with closed-loops. Qualitatively, the number of nonionic micellar bundles in the NI-FISP are much less compared to the amount of micellar bundles observed in the ionic FISP [167], possibly due to the absence of electrostatic interactions in the nonionic micellar solution. Since van der Waals interactions are weak in the nonionic micelles, we speculate that the interplay between entropy and curvature energy which are coupled through microspatial confinement and flow could produce an effective attraction between some wormlike micelles to form bundles in

the NI-FISP. However, future work is required to understand the mechanism underlying the bundle formation in the NI-FISP.

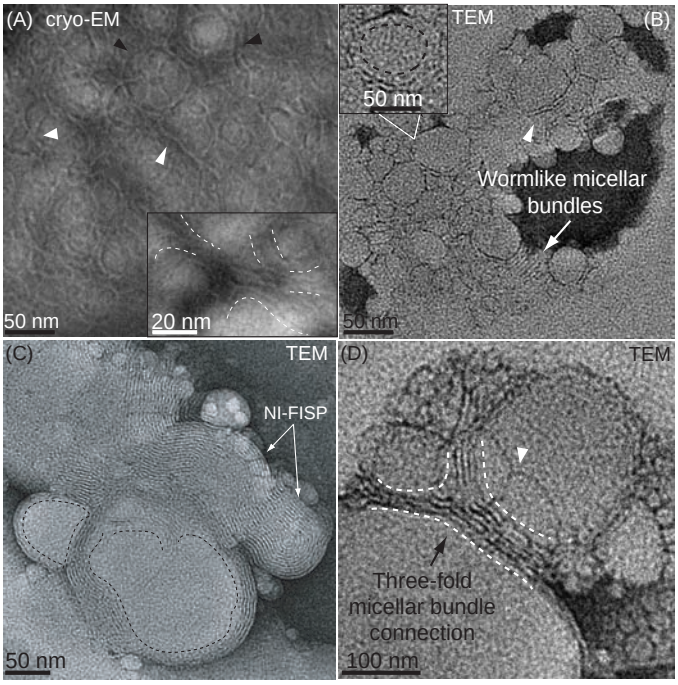


Figure 5.5: (a) cryo-EM image; (b, c and d): TEM images of the NI-FISP. (a) shows the formation an entangled and multi-connected micellar network with closed-looped micelles (black triangles) and "three fold" junctions (white triangles); the inset in (a) exhibits a micellar bundle making a three-fold junction with thickness of $\sim$ 4-28 nm (dash black lines are guide-lines); (b, c and d) also present multi-connected micellar networks with closed-looped micelles; the white triangles in (b) highlight the formation of connections, while the inset in (b) shows the formation of a closed-looped micellar bundle of $\approx$ 50 nm in diameter (dash black line is a guide-line). The darkest regions in (b, c and d) are caused by overly dosed negative stains.

Observing Figs. 5.4 and 5.5, the NI-FISP consists of interwined, entangled, and multi-connected micellar networks with closed-looped micellar bundles. The radius of the close-looped micelles ranges between $\sim$20-70 nm and its thickness $\sim$8-15 nm. Fig. 5.5(d) shows a three-fold micellar bundle junction with thickness of $\sim$20 nm. Interestingly, these three-fold junction structures were predicted theoretically [41,134] in the past. Fig. 5.5(a) is a cryo-EM image of the NI-FISP, showing several micellar bundles loops. These interconnected micellar bundle loops can lead to micellar branching structures under spatial confinement and flow, promoting the formation of NI-FISP. Similar micellar bundles and ring-like structures have

been reported previously for nonionic surfactant solutions with temperature and surfactant concentration variations, under quiescent condition [34, 37, 39, 40, 42, 44, 45, 136, 137]. For example, Afifi *et al.* [138] observed nonionic micellar bundles (diameter of 50-100 nm) and ring-like micelles (diameter of ∼10 nm) in a polyoxyethylene cholesteryl ether solution mixed with $C_{12}EO_3$ and ethyl butyrate. Lin *et al.* [45] used $C_{16}E_6/D_2O$ system and observed the formation of closed-looped micelles, ring-like micelles (diameter of ∼50-100 nm) and three-fold junctions. By using nonionic surfactant $C_{12}E_5$ solution, Bernheim-Groswasser *et al.* [41, 137] showed interconnected wormlike micelles formation as a function of temperature and surfactant concentration. At low temperature ∼8-18 °C, spherical micelles and dispersed wormlike micelles with length ∼50-100 nm co-existed. As temperature increased, the spherical micelles transformed into wormlike micelles and evolved into branched micelles with Y-junctions. They argued that the spontaneous curvature of the surfactant aggregates decreased with increasing temperature, prompting the structural evolution from spherical micelles to micellar networks. Similar behavior in polymeric solutions was observed by changing polymer concentrations [139]. In this work, we demonstrated a flow-induced approach to form irreversible nonionic micellar networks at room temperature. By storing NI-FISP in the DI-water at 23±2°C, the NI-FISP remained stable after 5 months without physical disintegration (see more stability studies below).

### *5.7 Stability of the NI-FISP*

To investigate the stability of the NI-FISP after the cessation of the flow, we monitored the possible disintegration of the NI-FISP that has been collected from the microchannel and suspended in DI-water. Macroscopically, we did not notice any disintegration of the NI-FISP over a period of 5 months (see Fig. 5.6). Microscopically, we performed cryo-EM of a NI-FISP sample that has been stored in DI-water for 5 days. The microstructure of the 5-day old NI-FISP still exhibits highly entangled and branched wormlike micelles, along with micellar bundles and micellar loops (see Fig. 5.7), with the morphology being similar to those of the fresh NI-FISP.

In addition, we also performed microrheology measurements on the 5-day old NI-FISP. After we produced the NI-FISP in the microchannel, we sealed the inlet and outlet of the

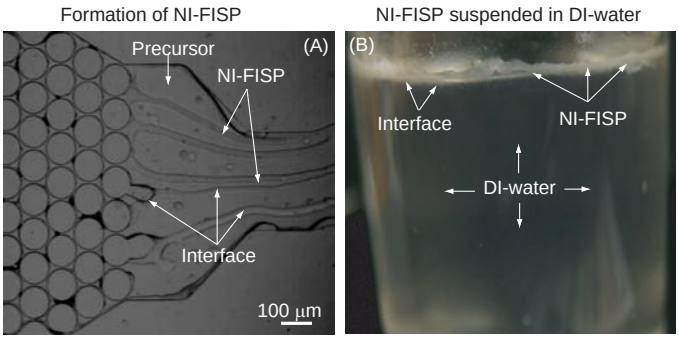


Figure 5.6: (A) Formation of the NI-FISP in the microchannel. A clear phase separation between the precursor and NI-FISP can be observed. (B) NI-FISP stored in DI-water over 5 months, the NI-FISP does not exhibit disintegration.

microchannel, and stored the microchannel containing NI-FISP in DI-water for 5 days before conducting microrheology experiments. We obtained similar rheological parameters in the aging NI-FISP (dashed curve in Figure 2 (B)) when compared to the fresh NI-FISP sample, with elastic modulus $G_0 = 8.3 \pm 3.4$ Pa, relaxation time $\lambda_{\text{eff}} = 1.5 \pm 1.1$ s and zero shear viscosity $\eta_0 = 12.5 \pm 4.8$ Pa·s. These values are within the error percentages compared to those obtained in fresh NI-FISP ($G_0 = 7.2 \pm 3.0$ Pa, $\lambda_{\text{eff}} = 1.2 \pm 0.8$ s, and $\eta_0 = 8.6 \pm 4.3$ Pa·s).

The stability of nonionic surfactant networks has been widely investigated [41, 152, 153]. Tlusty *et al.* [152] proposed a model to describe the stability of nonionic micellar networks whose basic building blocks are cylindrical tubes connected by spherical junctions. They showed that the interplay between entropy and curvature energy which are coupled through the connected topology of the network could produce an effective attraction between the junctions, promoting the stability of the nonionic micellar network structure. Bernheim-Groswasser *et al.* [41] studied the formation and stability of networks in the nonionic surfactant $C_{12}E_5$/water/n-octane at different concentrations by cryo-EM. They concluded that the network was held together due to an effective entropic attraction induced by the network fluctuations. Tlusty and Safran [153] predicted theoretically the formation of networks from disconnected cylinders as the temperature and spontaneous curvature were varied in a nonionic surfactant. They reported that nonionic micelles evolved from spherical globules

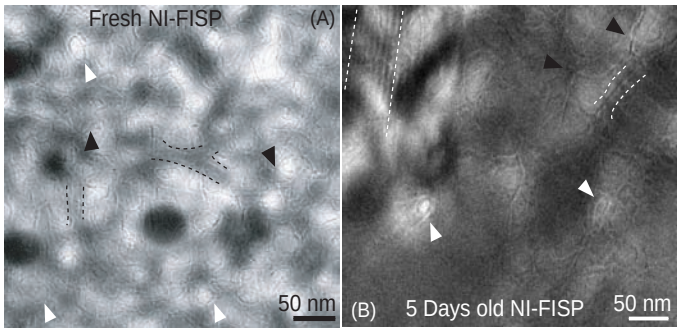


Figure 5.7: (a) Cryo-EM image of fresh NI-FISP. (b) Cryo-EM image of 5-day old NI-FISP. The microstructure of 5-day old NI-FISP presents entangled and branched micelles, as well as micellar bundles (areas enclosed by the white-dash lines), three fold junctions (black triangles), and micellar loops (white triangles). Both fresh NI-FISP and aging NI-FISP show similar structures.

to cylinders, with subsequent interconnection formed via three fold junctions. They conclude that the interplay between curvature energy and the network configurational entropy determines the network topology and the related free energy.

Relating Safran and coworkers argument, micropost arrays in the microchannel in our work enable high extension and shear rates, which promote high stretching of the wormlike micelles and induce entropic fluctuations in the nonionic precursor solution at room temperature. The high stretching and flow alignment increase the flexibility of the wormlike micelles, energetically it becomes more favorable for flexible adjacent micelles to merge when they flow through the microposts, promoting the micelles to form junctions and branches, eventually developing entangled and branched micellar networks.

### *5.8 Conclusion*

In summary, we observed the formation of stable closed-looped micellar bundles and multi-connected micellar networks in nonionic micellar solutions, by simply tuning flow conditions and micro-spatial confinement under room temperature. Two intertwined factors are at play for the NI-FISP formation: (1) the spatial confinement from the micropost arrays allows us to achieve high strain rates and total strain in the flow, enabling fusion and growth of spherical micelles to form both flexible wormlike micelles and super-micelles; (2) within the

spatial confinement, flow alignment increases the penetration frequency from the end caps of the micelles to other aligned micelles, promoting the wormlike micelles to create junctions and branches, eventually developing the NI-FISP. We also showed that a viscous nonionic micellar precursor could transition to viscoelastic micellar network structure. The zero shear viscosity of the precursor is around two order of magnitude smaller than that of its NI-FISP. This rheological variations can be correlated with the microstructural evolution from spherical micelles, to wormlike micelles, and finally to an entangled and multi-connected micellar network (NI-FISP). The formation of NI-FISP at room temperature, with mesh size on the order of ∼10-100 nm can be used for biomolecule encapsulation [125–127].

Chapter 6

# NANOSTRUCTURED TOROIDAL FORMATIONS IN MICELLAR SOLUTIONS

## *6.1 Introduction*

Wormlike micelles are elongated and flexible cylindrical aggregates with radii around 1–3 nm with lengths that may vary from nanometers to microns. The properties of wormlike micelles are similar to those of conventional flexible polymers. [2, 4] However, wormlike micelles can break and recombine in response to changes of ionic strength, temperature, and flow conditions [4]. Clausen *et al.* [45] were one of the first groups to report the formation of micellar torii in a wormlike micellar solution. Working with a solution consisting of the ionic surfactant CTAC, the inorganic salt NaCl, and the organic salt NaSal, they fixed the molar concentration of CTAC (0.05 M) and NaCl (0.1 M) while varying the molar ratio NaSal/(CTAC-NaCl) from 0 to 2.0 and observed toroidal micelles at a molar ratio of 1.0. Irregular and amorphous closed-looped micelles were observed in a cationic surfactant tetramer solution studied by In *et al.* [155]. They found the size distribution of these micelles with respect to contour length to be monomodal, with a distribution peak around 150 nm. Gummel *et al.* [156] inferred the existence of torii in an anionic and zwitterionic surfactant solution from small-angle-X-ray scattering (SAXS) patterns by fitting the scattering spectra to a toroidal form factor and deduced the thickness of toroidal micelles ($\sim$10 nm) with elliptical cross-section. They proposed that wormlike micelles may close off to form torii if the micellar length reaches a critical value. Cates and Candau [154] suggested that micellar rings may induce shear thickening behavior in micellar solutions. They proposed that shear thickening behavior might be caused by the interlinking and delinking of large micellar rings in a process requiring a positive feedback between the strain applied and the linking-delinking of the rings. Padding and Boek [157] used non-equilibrium molecular dynamics simulations to predict that, at fixed micellar concentration, shear flow may induce

the formation of rings from wormlike micelles. They found that shear flow decreases the entropy gain of the system and promotes the formation of micellar rings.

The Helfrich curvature free-energy model and the Poisson–Boltzmann equation have been frequently used to describe the formation, stability, and mechanical properties of membranes, vesicles, and toroidal structures [158–161]. For example, Sakaue [159] used Monte Carlo simulations to capture the formation of multiple torii from weakly charged wormlike chains, finding that, for weakly charged wormlike chains, the thickness of the torus is dictated by the surface energy and bending modulus of the chains. He and Schmid [162] performed mesoscopic field-based simulations to predict complex nanostructured micellar structural formations (e.g., toroidal micelles) in an amphiphilic block copolymer solution, concluding that toroidal micelles may be formed by controlling the copolymer volume fraction, molecular packing parameters and kinetic segregation in the solution.

Although toroidal structures serve as a good model system for nanotemplating and biomolecule encapsulations [163–165], the high-throughput synthesis of these nanostructures with reproducible shape and dimensions has been a key challenge for further exploring their applications. Flow-induced synthesis approach is a promising candidate for the scale-up nanomaterials production with desirable properties. For example, Wang *et al.* [166] reported a new strategy to generate large amount of micron size toroidal particles through solidification of droplets of polymer solution in a microfluidic device. However, the flow-induced formation of nanostructured toroidal micelles has not previously been investigated.

We report the formation of stable nanostructured toroidal micellar bundles (nTMB) in a semi-dilute wormlike micellar solution (precursor) with low surfactant and salt concentrations (see rheological properties in the supporting information). Recently [167], we reported the formation of highly entangled and multi-connected networks of micellar bundles when the same precursor is pumped through a microfluidic device containing hexagonal micropost arrays. In the work described here, we employed a two-step protocol wherein the precursor is pre-strained and then pumped into a microdevice identical to that used in our previous work [167] (see schematics in Fig. 6.2). To examine the structure of the nTMB, we used transmission electron microscopy (TEM) imaging and small angle neutron scattering (SANS). In particular, systematic TEM was applied to over 300 nTMBs from different

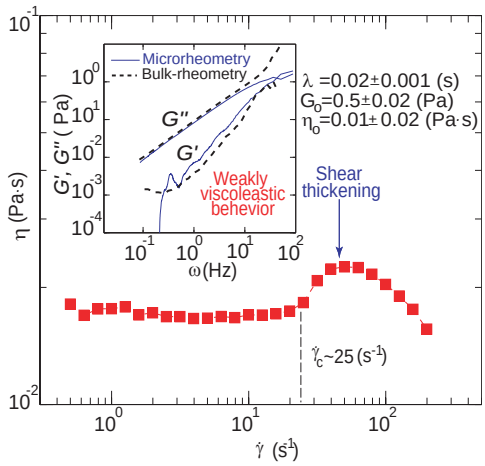


Figure 6.1: Shear viscosity versus shear rate of the precursor. The inset shows the linear viscoelastic behavior of the precursor; the dash black line is the bulk rheometry of the precursor, while, the solid blue line belongs to the microrheometry of the precursor. From the microrheometry we obtained the relaxation time ($\lambda_{\text{eff}}$=0.02±0.001 (s)) and elastic modulus ($G_0$=0.5±0.02 (Pa)) of the precursor. Whereas, we used the shear rheology to obtain the zero shear viscosity ($\eta_0$=0.01±0.02 (Pa·s)) of the precursor.

samples to obtain the size distribution of toroidal radius $R$, as measured from the center to the neutral axis of the nTMB. SANS measurements were used to characterize the structural transition from the precursor to nTMB. nTMB were found to remain stable at room temperature for no less than 5 days (see supporting information).

### *6.2 Results and discussion*

Our semi-dilute wormlike micellar aqueous solution (precursor) consists of cetyltrimethyl ammonium bromide ([CTAB] = 50 mM) and sodium salicylate ([NaSal] = 16 mM), with a molar ratio (NaSal/CTAB) of 0.32. Steady shear rheometry and oscillatory-shear rheometry were performed using a stress controlled rheometer (AR 2000) on the precursor solution. The temperature was fixed at 23°C and a solvent trap was used to avoid evaporation. An acrylic cone-plate geometry (40 mm in diameter and 2° of truncation angle) was used for all measurements. Fig. 7.2 shows the shear viscosity of the precursor as a function of the shear rate. The precursor solution exhibited a distinct viscosity jump once a critical shear rate was reached ($\dot{\gamma}_c \sim 25\ \text{s}^{-1}$). The increment in the apparent viscosity has been attributed to

the formation of transient shear induced structures created by entangled wormlike micellar networks under shear flow [4]. When the shear rate increased further ($\dot{\gamma} \sim 100$ s$^{-1}$) the wormlike micelles would align in the flow direction, leading to a viscosity drop.

Oscillatory-shear experiments were conducted at several strains to ensure the linear viscoelastic regime. The viscoelasticity behavior in the precursor was correlated with Maxwellian relationship with a single-dominant relaxation time. This stress relaxation time $\lambda_{\text{eff}}$ can be extracted from the first cross-over between the viscous modulus ($G''$) and the elastic modulus ($G'$). The Maxwell model can also deduce $G_0$, value at which the elastic modulus $G'$ reaches a plateau at high frequencies. The range of frequencies were varied from 0.01 to 100 Hz. Note that our stress-controlled rheometer is not sensitive enough to extract $\lambda_{\text{eff}}$ for the precursor$_{50}$ due to its weakly viscoelastic nature. Hence, microrheometry was used as an alternative to obtain $\lambda_{\text{eff}}$ and $G_0$ for the precursor (see details in supporting information). The inset in Fig. 7.2 shows good agreement between the bulk rheometry and the microrheometry of precursor within the $\omega$ limit from the bulk rheometry.

A mini-vortexer was used to pre-strain the micellar solution at $\dot{\gamma}_{ps} \approx 6.7\times10^4$ s$^{-1}$ for 15 s [168]. The pre-strained solution was then immediately pumped through the microdevice at a constant flow rate of 15 mL/h (see Fig. 6.2). We used a PDMS-glass microdevice containing a hexagonal array of microposts with diameter 100 $\mu$m, height 75 $\mu$m, and gap size 15 $\mu$m. For the given flow rate and dimensions, we estimated the maximum rate of strain in the microdevice to be $\dot{\gamma}_{microdevice} \approx 4.4\times10^4$ s$^{-1}$ [69]. The total strain rate that induces the nTMB formation is then $\dot{\gamma}_{total} \approx 1.1\times10^5$ s$^{-1}$. The formation of nTMB appears to be strongly dependent on the pre-straining process. A large quantity of nTMB formed for a critical pre-strain rate of $\dot{\gamma}_{ps} \approx 6.7\times10^4$ s$^{-1}$ in the wormlike micellar solution, followed by passing the solution to the micropost arrays (Fig. 6.4(A)). In contrast, at a lower pre-strain rate of $\dot{\gamma}_{ps} \approx 3.5\times10^4$ s$^{-1}$, only bent micellar bundles (Fig. 6.2) were observed.

Transmission electron microscopy (TEM) using a Tecnai F20 microscope at 200 keV was conducted to image the precursor, pre-strained precursor, and nTMB. The electron dose ranged from 1000–3000 electrons/nm$^2$. In the precursor solution, we observed a mixture of elongated and dispersed micellar bundles and single wormlike micelles (Fig. 6.2(b)). The micellar bundles had thickness and length of approximately $50 \pm 16$ nm and $800 \pm 125$ nm,

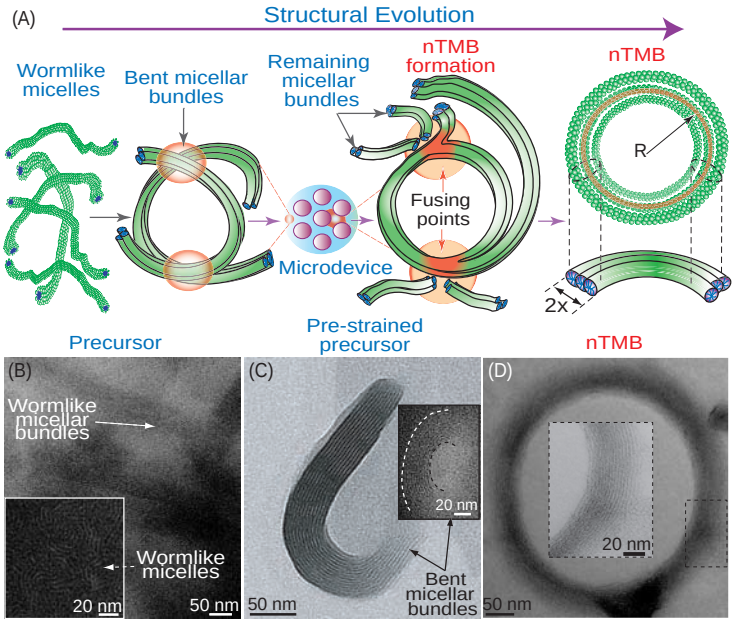


Figure 6.2: (a) Schematic of the microstructural evolution from wormlike micellar bundles to nTMB. When two flexible wormlike micellar bundles are brought together, they fuse at their cylindrical parts, creating a nTMB. The red circle in the schematic of the nTMB represents its neutral axis. (b) TEM images of the precursor, showing a mixture of wormlike micelles and micellar bundles. (c) TEM images of a precursor that was pre-strained at $\dot{\gamma}_{ps} \approx 6.7{\times}10^4$ s$^{-1}$, showing bent micellar bundles. (d) TEM images of a nTMB.

respectively; individual wormlike micelles showed a mean diameter and mean length of 5 nm and 16 nm, respectively, which is consistent with the literature [4]. Hence, each micellar bundle in the precursor consists of approximately 10 parallel wormlike micelles (Fig. 6.2(b)). As Sal ions from NaSal reside at the interface of the wormlike micelle and water, the CTAB micellar core can be effectively neutralized to induce the bundle formation [64, 65]. In the pre-strained precursor, we observed elongated and bent micellar bundles (Fig. 6.2). The bent micellar bundles formed arc segments on the order of microns with similar bundle thickness as those shown in the precursor. The post-flow sample shows the formation of nTMB, with approximately bundle thickness $2\xi \approx 20{\pm}10$ nm and radius $R$ ranging from 20 to 200 nm (Fig. 6.2(d), Fig. 6.3(a), Fig. 6.4 (a,b), and Fig. 6.5). Relative to bundles found in the precursor, the thickness of nTMB tends to be smaller and to have a wider size distribution.

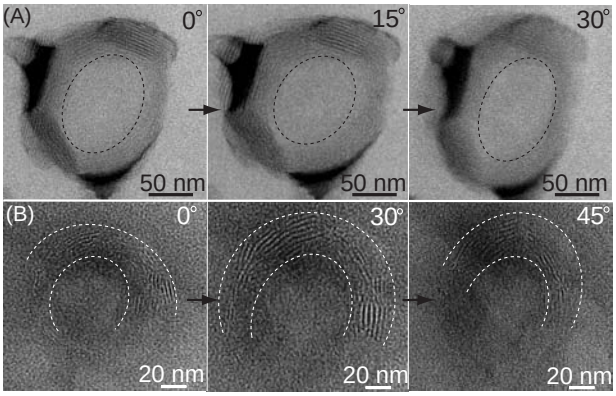


Figure 6.3: nTMB tilted at different angles. (a) nTMB created at $\dot{\gamma}_{ps} \approx 6.7{\times}10^4$ s$^{-1}$ with the pre-straining process. The diameter of the nTMB varies up to 15% when tilted in the direction perpendicular to the tilt axis (0 to 30°C), indicating planarity. (b) Semi-complete nTMB created at $\dot{\gamma}_{ps} \approx 3.5{\times}10^4$ s$^{-1}$ with the pre-straining process. The diameter and the shape of the semi-complete nTMB change with varying tilt angles, verifying the two-dimensionality of the structures. White-dashed and black-dashed lines are guide-lines.

To determine whether the nTMB are two-dimensional or three-dimensional objects (e.g., planar tori or vesicles), the samples were tilted at multiple angles before imaging (see Fig. 6.3). A TEM image is the projection of a sample onto a two-dimensional plane. If the nTMB is three-dimensional, the diameter of the projection should not change when the structure is tilted. However, if the nTMB is two-dimensional, the diameter and the thickness of the projection of the nTMB, in the direction normal to the tilting axis, should change with the tilting angle. Since the diameter and thickness of both nTMB and bent micellar bundles at different tilting angles vary between 5–15% (see Fig. 6.2), we infer that both the micellar bundles and the nTMB are two-dimensional structures (i.e., planar structures).

A histogram of the radius $R$ distribution of the nTMBs was constructed by measuring over 300 nTMB from different TEM samples (see Fig. 6.3 (d)). We obtained a mean radius $R \approx 52 \pm 31$ nm and a mean thickness $2\xi \approx 20 \pm 10$ nm. From the histogram, we observed that the dominant size of the nTMB ranged between 30–40 nm in radius. Jung *et al.* [169] studied the stability and formation of vesicles in a sodium perfluorooctanoate ($FC_7$)/CTAB vesicle solution at high salt concentrations, finding that the radius of the vesicles ranged between 23 nm and 37 nm.

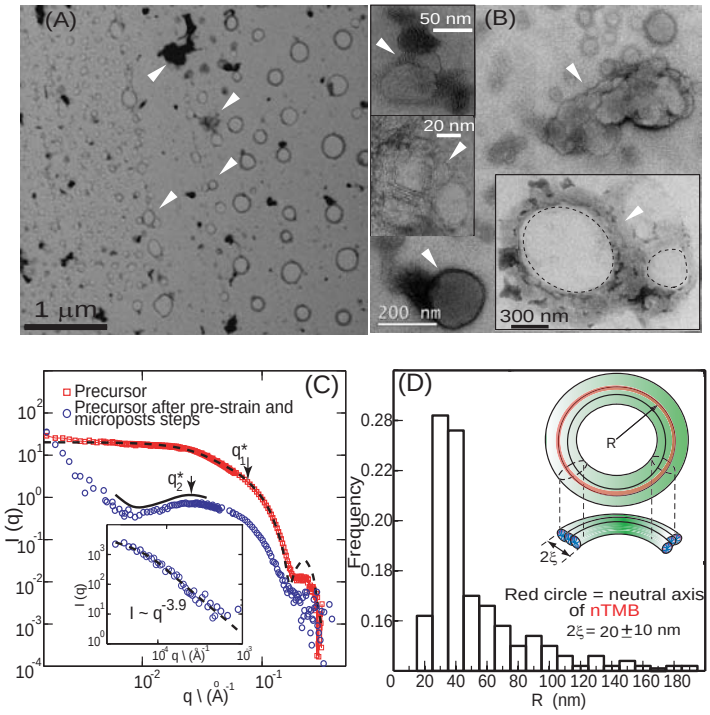


Figure 6.4: (a) TEM image of nTMB with various sizes. (b) TEM images of interlinked nTMB, the insets show the interlinkage of large and small nTMBs (white triangles). Black-dash lines are guide-lines. (c) SANS spectra of the precursor and the post-flow solution. The precursor (red-squares) is fitted to a dispersed cylindrical micellar model (dashed black line) with a mean radius of 2.2 nm and a mean length of 16 nm. The SANS spectra of the post-flow solution exhibits microstructural changes (blue-circles) related to the formation of nTMB and larger micellar aggregates; the solid-black line is a guide-line to show the correlation peak in the SANS data ($q_2^* \approx 25.1$ nm). $q_2^*$ is in good agreement with the thickness of the nTMB measured from TEM images ($\xi \approx 20 \pm 10$ nm). The inset shows the USANS spectra at low $q$ with a power law dependence in the scattering intensity (fitted to a Guinier model). (d) nTMB size distribution of $R$.

SANS experiments were conducted at the National Institute of Standards and Technology Center for Neutron Research (NCNR) in Gaithersburg, Maryland. SANS was performed using a standard configuration to cover a wide range of wave vector values. In addition, ultra-small angle neutron scattering (USANS) measurements were performed by using a perfect crystal diffractometer BT5 at the NCNR [60]. USANS increases the scattering range, so that sub-micron and micron sized features of the nTMB could also be probed. The SANS data of the precursor was fitted to a dispersed cylindrical micellar model [58]. From the data fit, the structures in the precursor were found to have a mean radius of approximately

2.2 nm ($q_1^*$) and a mean length of approximately 16 nm (red symbols in Fig.6.4(c)) [58]. These dimensions are consistent with the size of single wormlike micelles reported in literature. Although our TEM images show a mixture of single wormlike micelles and micellar bundles in the precursor solution (Fig. 6.2), we suspect that single wormlike micelles outnumber micellar bundles in the precursor; the SANS measurements therefore capture only the dimensions of the single wormlike micelles present in the precursor solution.

The SANS data of the post-flow solution (blue symbols in Fig. 6.4(c)) differs significantly from that of the precursor. Due to the presence of individual wormlike micelles, wormlike micellar bundles, and nTMB, no currently available model can be acceptably fit to the SANS spectra. Nevertheless, we estimated some of the characteristic dimensions in the post-flow sample. At intermediate values of the scattering vector ($q_2^*$), we found a correlation peak of $\approx$ 25 nm, which matches well with the thickness of the micellar bundles obtained from TEM images of nTMB ($2\xi \approx 20 \pm 10$ nm). At low values of the scattering vector ($q < q_2^*$), a power law dependence ($I \approx q^{-3.9}$) in the scattering intensity is observed (inset in Fig. 6.4) and is related to the presence of larger micellar structures. Using the Guinier model [58] to fit the SANS spectra at low $q$, we extracted a characteristic dimension of $\approx 1.1$ $\mu$m in the post-flow sample. In our TEM images, we noted the presence of some large aggregates as well as the inter-linking nTMB (white-triangles in Fig. 6.4(a,b)) on the order of microns. Structures like these may generate complex scattering spectra which are difficult to fit. Still, SANS verifies the existence of a dramatic flow-induced structural transition consistent with our TEM results.

The net free-energy of a wormlike micelle includes contributions associated with bending of its centerline, electrostatic interactions, and the presence of end caps. Closing a wormlike micelle eliminates the latter contribution but increases the remaining contributions and, thus, involves overcoming an energy barrier. An activation energy is therefore needed to form nTMBs. The necessary activation energy can be provided by tuning the thermodynamic properties of the micellar solution [45,155,156,162,171] or by subjecting the solution to flow [157]. We employ the second of these strategies via a pre-straining process and flow through a specially designed microfluidic device containing micropost arrays. In the precursor, the penetration of Sal ions in the CTA core [64,65] enhances the flexibility of the

wormlike micelles. During the pre-straining process of the precursor, external energy input bends the flexible wormlike micelles. Subsequently, the presence of micropost arrays in our device enables local concentration gradients of the bent wormlike micelles [14,69] along with high extension and shear rates [30, 47, 167], which promote high stretching of the wormlike micelles and wormlike micellar bundles. High stretching and flow alignment decrease the bending rigidity of the wormlike micellar bundles. The free energy of surfactant molecules in the end-cap therefore increases relative to the curvature energy of the cylindrical body of the micelle, leading to a decrease in the work required to form connections [77]. As adjacent and bent micellar bundles flow through the confined microposts, it becomes energetically favorable to minimize the number of end caps while concurrently promoting the fusion of the bent micellar bundles, yielding nTMB (Figure 1(A)). Interlinked nTMBs (see white triangles in Figure 3(A,B)) were also evident in TEM images. The interlinkage of torus micelles has been related to the shear thickening behavior of micellar solutions [154, 157].

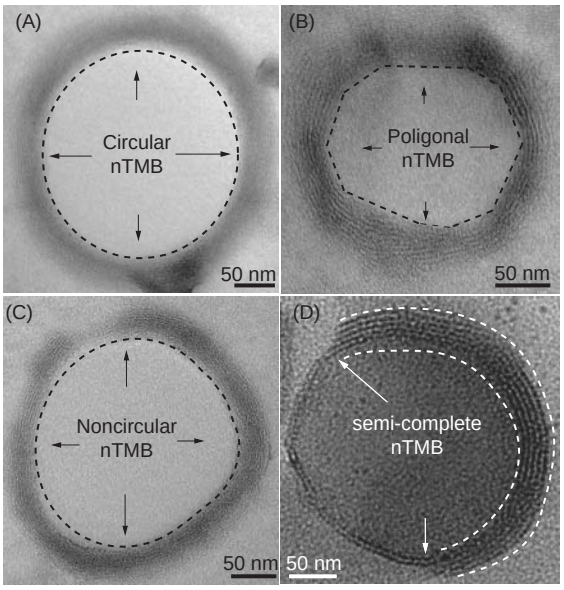


Figure 6.5: Diversity of nTMB. (a) Circular nTMB, (b) polygonal nTMB, (c) noncircular nTMB, and (d) incomplete semi-circular nTMB. Circular nTMBs were the dominant structure observed in the TEM micrographs.

In the post-flow sample, we also observed a wide variety of nTMB shapes: perfectly

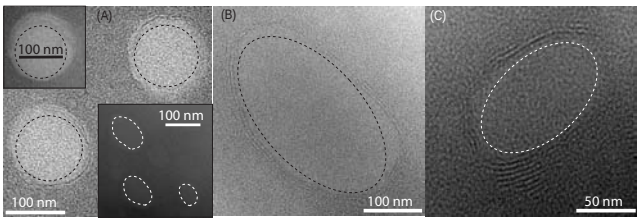


Figure 6.6: TEM images of the nTMBs that have been stored in DI-water for 5 days. (a) circular nTMBs and (b) elliptical nTMBs were observed in the stored samples. The thickness of the bundles is ∼10-20nm.

circular, polygon-like, noncircular, and semi-complete nanostructures (Fig. 6.5). The diverse morphology of toroidal structures has also been reported for toroidal-vesicles by tuning the temperature in the suspending solution [171]. The nTMBs have been shown to be stable; we imaged nTMB that were stored in DI-water at room temperature (see Fig. 6.6). The morphological diversity in our experiments originates from lack of control of the energy input during the pre-straining process. Our ongoing effort is to develop an optimal flow protocol to control the sizes and shapes of nTMB and possibly other micellar nanostructures. For example, a variety of interesting nanostructures were created when the precursor flows through the microdevice (no pre-straining), followed by sonicating the sample at 42 kHz at 100 W. With no sonication, we observed highly entangled and multi-connected micellar bundle networks (Fig. 6.7(a)) [167]. At 5 minutes of sonication, dispersed onion-like micellar structures formed (Fig. 6.7(b) and supporting information). Diat *et al.* reported that shear flow could induce the transition from lamellar to onion-like structures in surfactant solutions [172]. At 10 minutes of sonication, elliptical torus-like micelles were observed (Fig. 6.7(c)). At 15 minutes of sonication, nTMBs were observed. These nTMBs have the thickness ∼10±5 nm and radius ranging from 20-30 nm (Fig. 6.7(d)). The general trend shows that the characteristic dimensions of the observed nano-sized micellar structures decrease with increasing sonication time. Yusof *et al.* [173] studied the effects of sonication (211 kHz) in a wormlike micellar solution consisting of [CTAB]=0.015 M and [NaSal] = 0.015 M. They reported the formation of long threadlike micelles and multi-connected tubular micelles, but they did not observe toroidal structures. These preliminary studies indicate that the flow

procedure and the kinematics of the flow are critical to the structural formation in wormlike micelles.

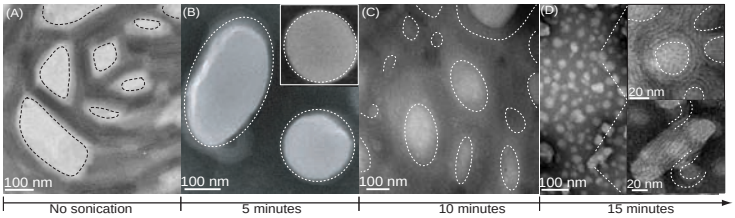


Figure 6.7: TEM images of the post-flow solution (precursor through micropost arrays followed by sonication). The sonication was held at 42 kHz. (a) With no soinication, a highly entangled and multiconnected micellar bundle network is formed; the bright areas are pores in the micellar network, while the darkest regions are inter-connected micellar bundles. (b) At 5 minutes of sonication, onion-shaped micellar structures formed. (c) At 10 minutes of sonication, ellipsoidal torus-like micelles formed. (d) At 15 minutes of sonication, regular sized nTMB (∼20-30 nm in diameter) are formed (see upper inset); some micellar bundles coexist with the nTMB (see lower inset). The lower inset shows the coiling of two wormlike micelles to form a nTMB (white-dashed lines).

An amphiphile consists of a covalently bonded hydrophilic head-group and one or more hydrophobic tails. In aqueous solvents at certain concentrations, noncovalent interactions drive the assembly of amphiphiles into supramolecular nanostructures in which tails are isolated from water and head groups are optimally spaced. These structures include lipid bilayers, vesicles, and spherical micelles [1, 2, 4]. Adding salt to an aqueous suspension of spherical micelles composed of an ionic surfactant screens the electrostatic interactions between adjacent surfactant molecules, causing spherical micelles to elongate into cylindrical and flexible wormlike micelles. A wormlike micelle possesses two hemispherical end caps. However, under certain thermodynamic conditions, it is energetically favorable for wormlike micelles to join at their end caps and form closed wormlike micelles [1]

Closed wormlike micelles of toroidal shape provide a model system for nanotemplating and for encapsulating biomolecules [165]. Clausen et al [170] reported the formation of toroidal micelles in solutions consisting of ionic surfactant cetyltrimethylammonium chloride (CTAC), organic salt sodium salicylate (NaSal), and inorganic salt sodium chloride (NaCl). Gummel *et al.* [156] identified toroidal structures in a mixture of anionic and zwitterionic surfactant solution from small-angle-X-ray scattering (SAXS) patterns. Recently, Cardiel et

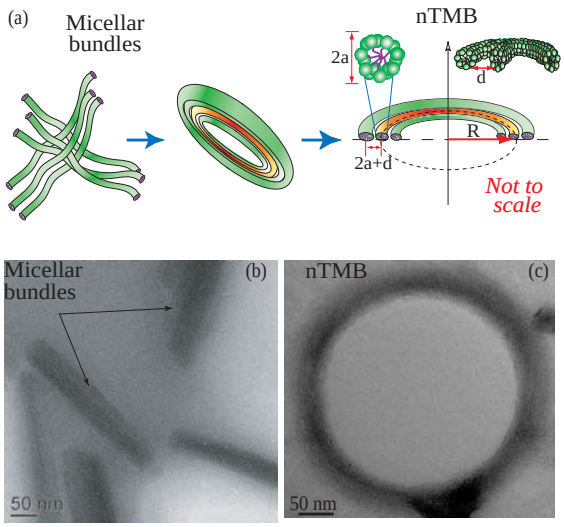


Figure 6.8: (a) Schematic of the microstructural evolution from wormlike micellar bundles to a toroidal bundle. The symbols $a$ and $d$ represent the radius and the interspacing between toroidal wormlike micelles, respectively. (b) TEM image of the precursor, showing a mixture of wormlike micelles and micellar bundles. (c) TEM image of a toroidal bundle.

al. [179] devised a flow-induced guided-assembly process to produce stable nanostructured toroidal bundles in a semi-dilute wormlike micellar solution of cetyltrimethylammonium bromide (CTAB) and NaSal. They observed mixtures of single wormlike micelles, dispersed micellar bundles, and toroidal bundles in the solution, as shown in Figs. 6.8 (b & c). Based on TEM and cryo-EM imaging, they found that the average thickness of a bundle is approximately $24 \pm 9$ nm and that the effective major radius $R$ of a bundle ranges from 30–100 nm (Figs. 6.8c and 6.9b). Cardiel *et al.* [179]. also reported that each bundle embodies approximately 3–6 concentric toroidal micelles (Figure 6.8c).

The present study relies on specializing a model for the free energy of a toroidal bundle. In doing so, Helfrich's [158] bending elasticity theory is used. According to that theory, the free-energy, per unit surface area, of the surfactant aggregate is given by

$$\gamma_\circ + 2\kappa_c(H - H_\circ)^2 + \bar{\kappa}_c K, \tag{6.1}$$

where $\gamma_\circ$ is the surface tension, $H$ and $K$ are the mean and Gaussian curvatures, $\kappa_c$ and $\bar{\kappa}_c$ are the flexural rigidity and the saddle-splay modulus, and $H_\circ$ is the spontaneous cur-

vature of the surface formed by the headgroups. The surface free-energy density (6.1) has been used to study the formation, stability, and mechanical properties of toroidal micelles. Bergström [188] applied (6.1) to a toroidal micelle to investigate the effect of flexural rigidity $\kappa_c$ on the size and shape of such a micelle and to analyze its stability. Proceeding similarly, Lauw *et al.* [189] applied (6.1) to a toroidal micelle comprised of nonionic surfactant molecules. Helfrich's theory (6.1) has been applied in various previous studies on different surfactant aggregates [174–177]. For instance, Jung et al. [178] used (6.1) to estimate the elastic constants of the lipid bilayer and its spontaneous curvature. Seifert [160] used (6.1) to study the stability of vesicles of toroidal topology without taking into account the spontaneous curvature effect. Ou-Yang [161] used (6.1) to study the formation and stability of anchor ring-vesicle membranes. In addition to the surface energy of the tori forming the bundle, the van der Waals interaction energy between the adjacent tori is taken into account. As a consequence, another material parameter, Hamaker constant, is introduced in the model.

The aforementioned material parameters play a significant role in understanding the mechanical behaviour of the bundle. The spontaneous curvature $H_\circ$ describes the natural shape of the bundle and is used as a geometrical parameter to analyze stability [181, 188]. The flexural rigidity $\kappa_c$ represents the resistance against deviations from the spontaneous curvature of the bundle [182]. It further describes the stability and stiffness of the bundle [183–185]. In our model, we rely on a range of representative values for the flexural rigidity for micelles made of ionic surfactants from previous studies [178, 186, 188]. Further, we fit the theoretical size distribution to the available experimental data to find the intervals of values for Hamaker constant and spontaneous curvature.

The paper is organized as follows. In Section 2, a free energy function for a toroidal bundle is proposed. In Section 3, the results of the fit between the model and the data coming from the experiments is reported and discussed.

## 6.3 Energetics of a toroidal bundle

### 6.3.1 Geometry

Let $a$ denote the length, assumed fixed, of a surfactant molecule. Consider a concentrically arranged bundle of $n > 2$ toroidal micelles of minor radius $a$ (Figures 6.8a and 6.9c). For each $k = 1, 2, \ldots, n$, let $R_k$ denote the major radius of torus $k$ and assume that $a < R_1 < R_2 < \cdots < R_n$. Suppose that each pair of tori in the bundle are separated by a gap $d > 0$, so that

$$R_k = R_1 + (k-1)(2a + d) \tag{6.2}$$

for each $k = 1, 2, \ldots, n$. The effective major radius of the bundle, denoted by $R$, satisfies

$$R = \frac{1}{n}\sum_{k=1}^{n} R_k = \frac{R_1 + R_n}{2}. \tag{6.3}$$

Eliminating $R_n$ between (6.2) evaluated at $k = n$ and (6.3) gives $R_1 = R - (n-1)(a + d/2)$, and (6.2) becomes

$$R_k = R + (2k - n - 1)\Big(a + \frac{d}{2}\Big). \tag{6.4}$$

### 6.3.2 Free energy

We consider the free energy of a bundle as the sum of two parts: the surface energy of tori inside the bundle, denoted by $E_s$, and the van der Waals interactions between the adjacent tori denoted by $E_i$. Previous results due to Bergström [188] and Ohshima and Hyono [187] are used to obtain those contributions.

### 6.3.3 Surface contribution to the free energy

To obtain the surface energy of a single toroidal micelle, Bergström [188] integrated Helfrich's free-energy density (6.1) over the surface of a torus. When applied to $n$ toroidal micelles arranged as described in Section 6.3.1, Bergström's result yields a surface energy $E_s$ of the form

$$E_s \;=\; \frac{2\pi n R}{a}(\beta k_B T \;-\; \pi\kappa_c) \;+\; \frac{2\pi^2\kappa_c R}{a}\sum_{k=1}^{n}\frac{R + (2k-n-1)(a+\frac{d}{2})}{\sqrt{(R + (2k-n-1)(a+\frac{d}{2}))^2 - a^2}}, \tag{6.5}$$

where $k_B$ is Boltzman's constant, $T$ is the absolute temperature, and $\beta$ is given by

$$\beta = \frac{\pi\kappa_c}{k_B T}(1 - 4aH_\circ + 4a^2 H_\circ^2) + \frac{2\pi\gamma_\circ a^2}{k_B T}. \tag{6.6}$$

Setting $n = 1$ in (6.5) gives the free-energy of a single toroidal micelle derived by Bergström [188] in equation 11 of his article.

### *6.3.4 van der Waals contribution to the free energy*

Ohshima and Hyono [187] derived an expression for the van der Waals interaction energy between a pair of tori with the same minor radius $a$, and major radii $r_1$ and $r_2$, and centers separated vertically by a distance $h$. For concentric adjacent tori with major radii $R_k$ and $R_{k+1}$, their result specializes to

$$4\pi^2 a^4 A \frac{R_k R_{k+1}}{(R_{k+1}^2 - R_k^2)^3}\Big(1 + \frac{6R_k^2 R_{k+1}^2}{(R_{k+1}^2 - R_k^2)^2}\Big), \tag{6.7}$$

where $A$ is the Hamaker constant. Summing (6.7) over $k$ from $k = 1$ to $k = n - 1$ gives the total van der Waals energy,

$$E_i \quad = \quad 4\pi^2 a^4 A \sum_{k=1}^{n-1} \frac{R_k^2 + (2a + d)R_k}{[(2a + d)(2R_k + 2a + d)]^3}\Big(1 \; + \; \frac{6R_k^2(R_k + 2a + d)^2}{[(2a + d)(2R_k + 2a + d)]^2}\Big), \tag{6.8}$$

of the bundle.

### *6.3.5 Total free-energy of a bundle*

On dividing both sides of (6.4) by $a$ and defining $r_k = R_k/a$, $r = R/a$, and $s = d/a$, we obtain

$$r_k = r + (2k - n - 1)\Big(1 + \frac{s}{2}\Big). \tag{6.9}$$

In view of (6.9), the surface energy $E_s$ in (6.5) and the van der Waals contribution $E_i$ to the free-energy in (6.8) can be expressed in terms of the dimensionless parameters $r$, $r_k$, and $s$ as

$$E_s \quad = \quad 2\pi n r(\beta k_B T \; - \; \pi\kappa_c) \; + \; 2\pi^2\kappa_c \sum_{k=1}^{n} \frac{2r^2 + (2k - n - 1)(s + 2)r}{\sqrt{(2r + (2k - n - 1)(s + 2))^2 - 4}}, \tag{6.10}$$

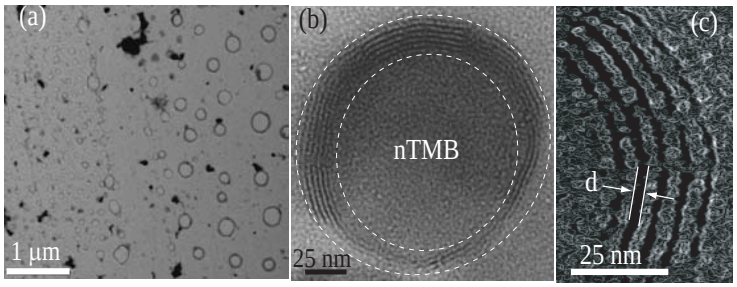


Figure 6.9: (a,b, and c) TEM images of toroidal bundles. (a) Low magnification cryo-EM image showing several toroidal bundles; (b) High magnification TEM image which exhibits multiple parallel toroidal micelles forming a bundle; (c) High magnification TEM image of a part of the bundle, processed by using the commercial software imageJ, exhibiting the edges of individual toroidal micelles in the bundle.

and

$$E_i \quad = \quad 4\pi^2 A \sum_{k=1}^{n-1} \frac{r_k^2 + (s+2)r_k}{[(s+2)(2r_k+s+2)]^3}\Big(1 \quad + \quad \frac{6r_k^2(r_k+s+2)^2}{[(s+2)(2r_k+s+2)]^2}\Big). \quad (6.11)$$

### *6.4 Size distribution*

According to Bergström, [188] the volume fraction density (or size distribution function) $\Phi$ of an aggregate of $N$ surfactant molecules is given in terms of its total free-energy $E$ by

$$\Phi = \frac{dN}{dr} \exp\Big(-\frac{E}{k_B T}\Big). \quad (6.12)$$

Following Bergström, [188] the quantity $N$ can be obtained by setting the volume of the tails of $N$ surfactant molecules equal to that occupied by the aggregate. On denoting the volume of the tail of a single surfactant molecule by $v$, the volume of $N$ surfactant molecules forming the bundle is $Nv$. The volume of a bundle of $n$ toroidal micelles each of minor radius $a$ arranged as described in Section 2 is obtained by using the second Pappus–Guldinus theorem [190]. Therefore,

$$Nv = \sum_{k=1}^{n} 2\pi^2 a^2 R_k. \quad (6.13)$$

In view of (6.4) and the relation $R = ra$, (6.13) yields

$$N = \frac{2\pi^2 a^3 nr}{v}. \quad (6.14)$$

Consequently $dN/dr = 2\pi^2 a^3 n/v$, and (6.12) becomes

$$\Phi = \frac{2\pi^2 a^3 n}{v} \exp(-\frac{E}{k_B T}). \tag{6.15}$$

### *6.5 Results and discussion*

Systematic TEM was applied to over 300 different samples of bundles (Fig. 6.9a). High magnification TEM images exhibit multiple parallel toroidal micelles forming each bundle (Fig. 6.9b). Also, adjacent tori in a bundle are separated by a gap of $1.2 \pm 0.2$ nm (Figure 6.9c). TEM images were analyzed to obtain the experimental size distribution of bundles based on the effective major radius $R$ of the bundles. To do so, we plotted the frequency of the bundles with a specific number of tori in terms of the effective major radius $R$ of the bundles. This yields a series of bar graphs called histogram which can be observed in Figure 6.10c. According to the TEM images, the majority of the observed bundles include four tori.

Next, the histogram of the experimental data is fit to the theoretical size distribution function (6.15). The range of values for flexural rigidity $\kappa_c$ of CTAB-based aggregates has been reported in previous studies. For instance, Abillon and Perez [186] reported $\sim 5.5 \pm 3\ k_B T$ for CTAB-based lamellar phases. Jung *et al.* [178] reported in the range of 0.7–8 $k_B T$ for CTAB-based vesicles. More specifically, Bergström [188] chose the flexural rigidity of a single toroidal micelle made of ionic surfactants to be 2–5 $k_B T$. Following Bergström, [188] and consistent with the observation that the tori within a bundle are separated, the value of $\kappa_c$ for a toroidal bundle is considered in the range of 1–10 $k_B T$. Fitting the expression (6.15) to the histogram (Fig. 6.10c), while considering the flexural rigidity within the aforementioned range yields ranges of values for spontaneous curvature $H_\circ \sim 0.202$–$0.215\ \text{nm}^{-1}$, and for Hamaker constant $A \sim 0.1$–$5\ k_B T$ (see Fig. 6.10a).

The spontaneous curvature $H_\circ$ describes the preferred, natural, local shape of the bundle. Based on a set of curve fits, $\beta \sim 0.0007$–$0.0055$, which is close to zero, consistent with Bergström's [181] predictions for a single toroidal micelle. Given the value $\kappa_c$ in the range of $1$–$10\, k_B T$ and $\beta$ in the range of 0.0007–0.0055, (6.6) can be used to determine $H_\circ$. In so doing, the value $\gamma_\circ = 7.8\, k_B T/\text{nm}^2$ of the surface tension of CTAB/NaSal has been

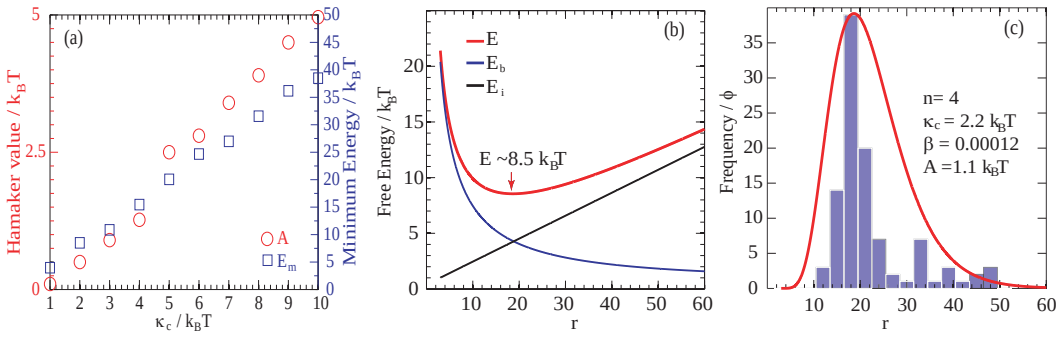


Figure 6.10: (a) The fitted values $A/k_BT$ and the associated minimum value of the energy $E/k_BT$ based on the chosen range of $\kappa_c/k_BT$; (b) presents the energy curves of the bundle; (c) shows a fit of the model to the size distribution histogram determined from the TEM images, by using the a fixed value $\kappa_c = 2.2\,k_BT$.

used. [1,179,191] This value is on the same order of magnitude as those previously reported by Bergström [188] for CTAB $\sim 12\ k_BT/\text{nm}^2$. The spontaneous curvature $H_\circ$ is found to be in the range of 0.202–0.215 $\text{nm}^{-1}$. According to Bergström, [181] a toroidal micelle is stable only if its spontaneous curvature exceeds $1/4\xi$, with $\xi$ being half the thickness of the cross-section. Granted this, the minimum spontaneous curvature that a stable bundle may adopt is $1/4\xi$. For the effective measure of the cross-sectional thickness of a bundle consisting of $n$ tori, separated by gaps $d$, we choose $2\xi = 2na + (n-1)d$. For $n = 4$, the resulting minimum allowable spontaneous curvature for the bundle is approximately 0.022 $\text{nm}^{-1}$, which is an order of magnitude lower than the value $H_\circ$ in the range of 0.202–0.215 $\text{nm}^{-1}$ obtained by the fit. This suggests that, at least on average, the obtained bundles by Cardiel *et al.* [179] are metastable.

Various studies have been carried out to estimate values for the Hamaker constant of CTAB-based micellar solutions. Goyal *et al.* [192] used small-angle neutron scattering techniques and found the value of the Hamaker constant for CTAB/potassium chloride (KCl) spherical micelles to be $\sim 12.5\ k_BT$. Using light scattering techniques, Dorshow *et al.* [193] found a Hamaker constant value of $\sim 15\ k_BT$ for CTAB/sodium bromide (NaBr) spherical micelles. Granted that the major radius $R_1$ of the inner torus is much larger than the minor radius $a$, two concentric adjacent tori may be approximately considered as two long parallel

cylinders. According to Israelachvili, [1] the Hamaker constant $A$ for a symmetric system of cylinder–cylinder is given by

$$A = \frac{3}{4} k_B T \Big( \frac{\epsilon - \epsilon_\circ}{\epsilon + \epsilon_\circ} \Big)^2 + \frac{3h\nu}{16\sqrt{2}} \frac{(\zeta^2 - \zeta_\circ^2)^2}{(\zeta^2 + \zeta_\circ^2)^{3/2}}, \tag{6.16}$$

where $\epsilon$ and $\epsilon_\circ$ are the dielectric constants of the solvent and the solute, $\zeta$ and $\zeta_\circ$ are their refractive indices, $\nu$ is the absorption frequency, and $h$ is Planck's constant which is $6.63 \times 10^{-34}\ Js$. According to Sonin *et al.* , [194] the dielectric constant $\epsilon$ for CTAB is in the range 2.1–3, and its counterpart $\epsilon_\circ$ for water is in the range 75.5–80. According to Spalla and Kekichef, [195] the refractive index $\zeta$ for CTAB is in the range 1.34–1.43 and its counterpart $\zeta_\circ$ for water is 1.33. The absorption frequency for CTAB-based solution is $3 \times 10^{15}\ s^{-1}$ (Israelachvili [1]). Thus, the Hamaker constant for two long parallel cylinders forming the CTAB-water-CTAB system (neglecting the effects of NaSal for simplicity) lies within the range of $\sim 0.68$–$1.3\ k_B T$. From the curve fits, the Hamaker constant of a toroidal bundle ranges from 0.1–5 $k_B T$, as shown in Figure 6.10a. It is important to mention that the studies of Goya *et al.* [192] and Dorshow *et al.* [193] were done with inorganic salt and spherical micelles. Cardiel *et al.* [179] used the organic salt, NaSal, which deeply penetrates the core of the wormlike micelle [64, 65].

The model considered here incorporates competition between the surface energy of individual tori and the van der Waals interaction energy between the adjacent tori comprising the bundle. The geometry of the resulting supramolecular structure is therefore the result of the balance between those two opposing interactions. At equilibrium, since the van der Waals interaction between two adjacent tori cannot exceed the surface energy of each torus, the adjacent tori remain separated by the distance $d$. Fig. 6.10b provides plots of the total free-energy $E$ (red line), surface energy $E_s$ (blue line), and the van der Waals interaction $E_i$ (black line) with respect to the dimensionless radius $r$, as determined by (6.10) and (6.11). As shown in Fig. 6.10b, the surface energy decreases monotonically with increasing $r$; however, the van der Waals energy exhibits what appears to be linear growth with $r$. At a particular value $r^*$ of $r$ the total free-energy exhibits a minimum which represents the equilibrium state. For $r < r^*$, surface energy exceeds that accounting for van der Waals interactions, indicating that forces associated with bending must dominate the process of

forming a bundle. However, for $r > r^*$ the energy associated with van der Waals interactions between the adjacent tori exceeds the surface energy.

As shown in Fig. 6.10a, the total free-energy of a bundle attains a minimum of 3.9–38.4 $k_BT$ for $r^* \sim$ 15–20. From Bergström's [188] work, the minimum energy required to form a single toroidal micelle is 15 $k_BT$. The energy for a bundle is on the same order of magnitude, but higher than the predictions for a single torus which only includes the surface energy. The presence of bundles indicates that the processing path allows the system to find metastable equilibria involving bundles with higher energies than single torus.

### *6.6 Conclusion*

We report a simple and novel flow-induced procedure (pre-straining process with microfluidic flow) to generate nanostructured toroidal micellar bundles (nTMB) in a semi-dilute micellar solution (CTAB/NaSal). These nTMB, which consist of regular sized and shaped micellar bundles, were found to form at low salt concentrations and to remain stable for no less than 5 days. The dimensions of the nTMB were visualized by TEM imaging and are consistent with the structural transition trend illustrated by SANS measurements. Our work also suggests that other flow-induced approaches such as sonication can generate and control the emergence of onion-shaped and nano-toroidal structures useful for nanotemplating [163–165]. Our nanostructured toroidal micellar bundles provide a potential platform as nanoreactors, encapsulation and drug carriers with tunable shapes, sizes, and structural rigidities. Our work also shows that flow-induced approach is a promising candidate for the scale-up nanomaterials synthesis with desirable properties. The present study was the first attempt to derive a model for the free energy of such bundles. The derived free-energy incorporates a combination of surface energy of the toroidal micelles comprising the bundle, and the van der Waals interactions between adjacent tori. The surface contribution to the free energy was found based on the results of a previous study on toroidal micelles [188]. The van der Waals contribution to the free energy was obtained using the results of a recent study on the van der Waals interaction between two colloidal tori [187]. Following a previous study by Bergström, [188] the theoretical size distribution of the bundle was found in terms of the derived free-energy. Using a range of representative values for the flexural

rigidity for micelles made of ionic surfactants, [178, 186, 188] and fitting the theoretical size distribution to the available experimental data, the intervals of values for Hamaker constant and spontaneous curvature were obtained. The range of values for spontaneous curvature indicates that the bundles are energetically metastable. The obtained range of Hamaker constant for the system covers the calculated range of the Hamaker constant for a similar system of long parallel cylinders. According to the presented model, the formation of a toroidal bundle is determined by a competition between the surface energy of the tori and the van der Waals interactions between them. While the van der Waals interactions tend to merge the tori to a single surface, the surface energy of each torus tends to keep it separated from its adjacent tori. At equilibrium, the surface energy dominates the van der Waals attraction. As a consequence, the tori inside the bundle are separated by a very small gap observed in TEM images. The obtained range of the minimum free-energy of a bundle is on the same order of magnitude, but higher than the predictions for a single toroidal micelle, indicating that the system finds metastable equilibria including bundles with higher energies than single tori. The presented model in this study is capable of quantifying observations of toroidal bundles in other similar surfactant solutions.

Chapter 7

# ENCAPSULATION OF SINGLE-WALLED CARBON NANOTUBE INSIDE OF THE FISP STRUCTURE

## *7.1 Introduction*

Single-walled carbon nanotubes (SWCNTs) are cylindrical structures with diameters of 1–2 nm and lengths ranging from a few nanometers to tens of microns [196–199]. SWCNTs possess attractive properties (e.g., high electrical and thermal conductivity) for novel technological applications, such as in biosensors and field effect transistors [197, 199]. The dispersion of SWCNTs in cationic, anionic and non-ionic surfactant solutions has been widely studied [200–206]. Surfactant molecules get absorbed onto the SWCNT surface to alter electrostatic interactions among SWCNTs, subsequently enhancing uniform dispersion of SWCNTs in solvents [207–211]. Factors such as the electric-charge, the size of the hydrophilic group, and concentration of the surfactant all affect the dispersion quality of SWCNTs. Anionic surfactant sodium dodecyl sulfate (SDS) has demonstrated good results in dispersing SWCNTs [200, 203, 206–208, 210]. Richard *et al.* [207] observed that SDS molecules were absorbed on the surface of SWCNTs, creating negatively distributed charges to prevent SWCNTs aggregations. They reported that SDS molecules could be adsorbed perpendicular to the surface of SWCNTs, organizing into half-cylinders either along or perpendicular to the SWCNTs. Similarly, O'Connell *et al.* [208] reported that SDS molecules could bend and turn in radial position on the SWCNTs surface, forming concentric cylindrical structures. O'Connell *et al.* also showed that the orientation of SDS molecules promoted the formation of SWCNTs bundles. More recently, Calvaresi *et al.* [211] studied the effects of surfactant concentration on the self-assembly of surfactant molecules around SWCNTs by using dissipative particle dynamics simulations. Their simulation results showed that the mixture of SWCNTs and surfactant molecules could generate complex self-assembled morphologies.

In an aqueous pH buffer solution, the electronic properties of SWCNTs have displayed considerable changes due to the amount of hydroxide ions ($OH^-$) present in the solution, implying that SWCNTs can be potentially integrated into a pH sensor to detect chemical or environmental changes [213–219, 244]. In fact, individual SWCNTs and SWCNT networks have been used to fabricate pH sensors [196–198, 210, 214–216, 218, 244]. SWCNT based pH sensors such as SWCNT-glass electrodes [214], polymer-SWCNT networks [215], and SWCNT nano-bridges electrodes [216] showed increasing conductivity in the sensor as the pH value of the buffer solution increased. The complexity to isolate and interconnect individual SWCNTs in a device makes SWCNT network-based device more attractive. SWCNT networks possess large surface areas, are simple to fabricate, and readily scalable for industrial applications. For example, encapsulating SWCNTs in a scaffold carrier (e.g., polymers or gels) facilitates the formation of SWCNT networks for pH and other sensing applications [196, 197, 210, 214–216, 218, 244]. However, most of the existing fabrication processes for SWCNT based pH sensors are tedious and costly, involve chemical procedures (i.e., chemical vapor deposition) and sophisticated equipment.

Motivated by this challenge, we propose a novel flow-induced microfluidic approach to synthesize electro-conductive SWCNT-based porous scaffold under proper hydrodynamic conditions by mixing dispersion of SWCNTs with a wormlike micellar solution. Synthesis of stable gel-like micellar structures from ionic wormlike micelles was first reported by Vasudevan *et al.* [30]. A semi-dilute ionic micellar precursor solution (CTAB with organic salt sodium salicylate (NaSal)) formed a gel-like *flow-induced structured phase* (FISP) after the wormlike micellar solution flowed through a microfluidic tapered channel packed with glass beads (20-100 $\mu$m in diameter). This irreversible gelation originates from a combination of the high rates of strain ($\dot{\epsilon} \sim 5{,}000\ s^{-1}$) and from the extensional characteristics of the flow. Cardiel *et al.* [167] extended this study and reported the formation of FISP from both ionic shear thinning and shear thickening micellar solutions when subjected to strain rates $\sim 10^3\ s^{-1}$ and strains $\sim 10^3$. The FISP consists of entangled, branched, and multi-connected micellar bundles, evidenced by electron microscopy imagings. To our best knowledge, there is no reported research on the dispersion and encapsulation of SWCNTs in micellar gel-like structures for sensing applications.

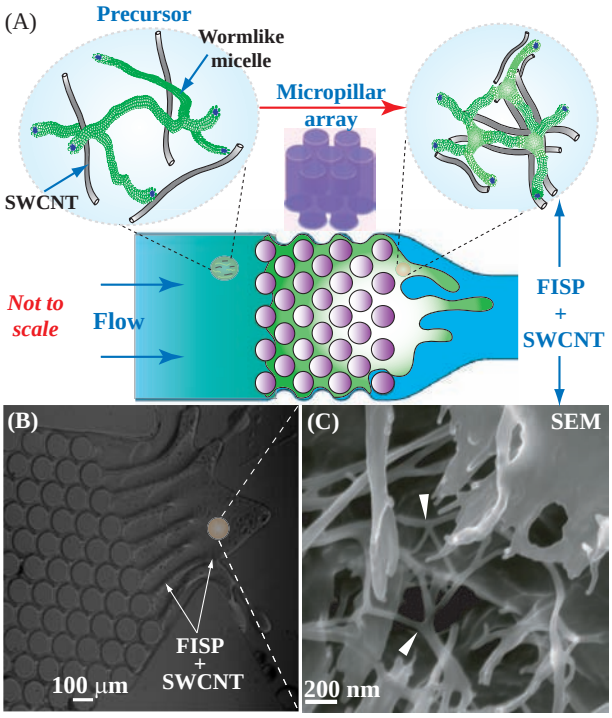


Figure 7.1: (a) Schematics of encapsulating SWCNTs in the gel-like flow-induced structured phase (FISP). When the IP-SWCNTs-SDS precursor was pumped through the microposts, highly entangled and multi-connected micellar networks encapsulated with SWCNTs were formed. (b) Optical microscopy image of the FISP-SWCNTs formed in the microfluidic device. (c) Scanning electron microscopy image (SEM) of the FISP with encapsulated SWCNTs. The white triangles highlight the branched structure made of SWCNTs and CTAB/NaSal wormlike micelles.

In this work, we first prepared SWCNT dispersions in an aqueous solution with anionic surfactant sodium dodecyl sulfate (SDS). We then mixed the dispersion of SWCNTs with a semi-dilute ionic micellar solution containing cationic surfactant cetyltrimethylammonium bromide (CTAB) and organic salt sodium salicylate (NaSal) as the precursor solution. By pumping the precursor solution through a microfluidic device with microposts at room temperature and ambient pressure (see Fig. 7.1), SWCNTs were encapsulated in the gel-like FISP structure, yielding electro-conductive porous scaffolds consisting of bundled networks, assembled from SWCNTs and wormlike micelles. We also show proof of concept studies of using SWCNT-based electro-conductive scaffold for pH sensing.

## *7.2 Experimental Methods*

### *7.2.1 Dispersing single-walled carbon nanotubes (SWCNTs)*

SWCNTs were purchased from Unidym-TM (HIPCO® Single-Wall Carbon Nanotubes) and used as received. Sodium dodecyl sulfate (SDS) was purchased from Sigma Aldrich and mixed with deionized water for the dispersion of SWCNTs. The utilization of surfactant-coated carbon nanotubes has become a standard procedure to uniformly disperse SWCNTs to enhance both materials and device performances [220, 221]. We dispersed 1 wt% of SDS and 1 wt% of SWCNTs in DI-water and sonicated the mixture for 5 hours. Note that the critical micellar concentration (CMC) of SDS in water is $\sim 0.2$ wt%. The dispersed solution was then incubated at room temperature for another 3 hours. The upper 80% ($\sim$0.8 wt% of SWCNTs) of the supernatant was collected and used for the precursor preparation.

### *7.2.2 Electro-conductive response of FISP-SWCNTs scaffold*

For potential sensing applications, FISP-SWCNTs scaffold was tested for pH sensing. After collecting FISP-SWCNTs scaffold (see Fig. 7.7(a)), 3 $\mu$L of the solution was deposited onto a microfabricated gold electrode with 5 $\mu$m in gap size (see schematics in Fig. 7.7). Subsequently $\sim$3 $\mu$L of pH buffer solution was added. The voltage was applied (from 0.0 to 10.0 V with step size of 0.1 V) by using a Keithley 6487 picometer to obtain the current versus voltage curves (IV curves). Three buffer solutions with different pH values (pH= 4.0, 7.0, and 10.0) were used to capture the electro-conductivity response of FISP-SWCNTs.

## *7.3 Experimental Results and Discussion*

For comparison purposes, we have performed systematic materials characterizations involving the following samples: the semi-dilute ionic CTAB/NaSal wormlike micellar solution (IP), the precursor solution containing the dispersion of SWCNTs and IP (IP-SWCNTs-SDS), and the gel-like FISP structure encapsulated with SWCNTs (FISP-SWCNTs).

### *7.3.1 Shear rheology of the precursor*

Fig. 7.2 shows the steady shear rheology of the CTAB/NaSal wormlike micellar solution (IP), mixture of IP with SDS (IP-SDS), and IP-SWCNTs-SDS precursor solution. The IP solution exhibited a distinct viscosity increase once a critical shear rate was reached ($\dot{\gamma}_c \sim 50$ s$^{-1}$). This shear viscosity increase has been attributed to the formation of transient shear-induced structures created by entangled wormlike micellar networks under shear flow [4]. With further increase of shear rates ($\dot{\gamma} \sim 100$ s$^{-1}$), the wormlike micelles would align in the flow direction, leading to a shear viscosity drop (see red open circles in Figure 7.2). After mixing the dispersion of SWCNTs with IP, the shear thickening response disappeared. Instead, shear thinning behavior emerged with a significant increase in the zero shear viscosity by one order of magnitude (see red closed circles in Figure 7.2). We attribute this rheological change in the IP-SWCNTs-SDS precursor to the presence of surfactant SDS molecules rather than the effects from SWCNTs addition. In fact, shear thinning behavior with the similar zero shear viscosity was observed for the mixture of IP-SDS (0.9 wt% CTAB, 0.1 wt% NaSal, and 0.1 wt% SDS), see blue open circles in Fig. 7.2. CTAB wormlike micelles have positively charged head groups while SDS micelles are negatively charged with small head groups. The difference in electric charges and head group size in CTAB and SDS micelles promotes the formation of longer wormlike micelles [1, 4], which can lead to the viscosity increase and shear thinning behavior in both IP-SDS and IP-SWCNTs-SDS solutions. The slight rheological difference between IP-SWCNTs-SDS and IP-SDS is possibly due to the presence of SWCNTs. Nevertheless, the amount of SWCNTs present in the IP is not sufficient to induce significant rheological changes, as evidenced by the variation between blue-symboled curve and close red-symboled curve in Fig. 7.2. In a recent study reported by Ben-David *et al.* [204], a drastic shear viscosity increase was observed when SWCNTs (0.1 wt%) were added to a CTAB (9-23 wt%) micellar solution, also showing shear thinning response. They noted that pure CTAB solutions at concentrations $< 20$ wt% behaved like Newtonian fluids. There are two major differences between Ben-David *et al* 's work and ours. Despite the similar concentration of SWCNTs in the micellar solution ($\sim$ 0.1 wt%), the CTAB concentration in our work is low (0.9 wt%) in comparison to 9-23 wt% CTAB concentration

used in Ben-David *et al* 's work. In addition, anionic surfactant SDS (0.1 wt%) is present in our study. The interaction between anionic SDS molecules and cationic CTAB/NaSal micelles in our micellar solution not only modifies the rheological behavior of the solution, but also potentially screens out the effects from SWCNTs.

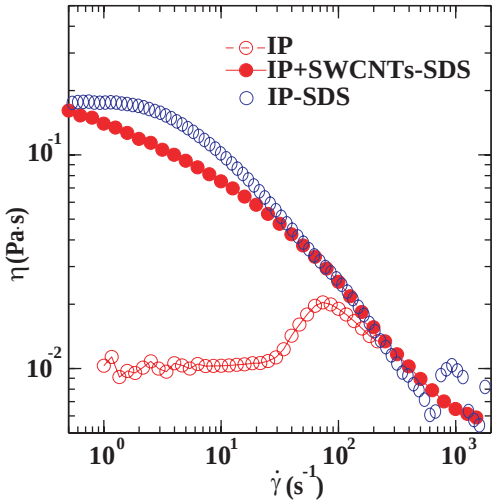


Figure 7.2: The CTAB/NaSal wormlike micellar solution (IP) shows shear thickening followed by shear thinning trend with increasing shear rates, with a zero shear viscosity of ∼0.01 Pa·s (red open circles). The IP-SWCNTs-SDS precursor shows shear thinning response with a zero shear viscosity of ∼0.18 Pa·s (red closed circles). The mixture of CTAB/NaSal and SDS solution (IP-SDS) shows a shear thinning response (blue open circles), with a similar zero shear viscosity of that of IP-SWCNTs-SDS precursor.

### *7.3.2 Electro-conductive porous scaffold synthesis*

The IP-SWCNTs-SDS precursor was driven by Harvard apparatus digital pumps at a constant flow rate (15 mL/h) through the microdevice. Once the IP-SWCNTs-SDS precursor passed through the micropost arrays, a gel-like structured phase appeared. Fig. 6.2(a) illustrates the schematic diagram of the FISP-SWCNTs structure formation, while Fig. 6.2(b) shows an optical microscopy image of the microdevice with finger-like FISP-SWCNTs emerging downstream past the micropost. Fig. 6.2(c) shows a scanning electron microscopy image of the FISP-SWCNTs, with white triangles highlighting the three fold junctions in the FISP-SWCNTs scaffold.

## *7.4 Material characterizations of FISP-SWCNTs scaffold*

Since the conversion rate from the precursor to the FISP scaffold is not 100% from the microfluidic process, we collected the sample from the microchannel containing the FISP-SWCNTs scaffold, liquid precursor, and SWCNT residues. We then added 15 mL of DI-water and centrifuged the diluted solution at 1500 RPM for 30 minutes. We left the centrifuged solution without agitation for 2 days before experiments. A thin layer containing the concentrated FISP-SWCNTs scaffold was extracted at the top of the stored solution (see Fig. 7.3 (a)). We then performed systematic material characterizations of the FISP-SWCNTs scaffold by conducting electron microscopy imaging (SEM and TEM) and ultra-violet spectroscopy, see details below.

### *7.4.1 Electron microscopy*

To investigate detailed composition inside each bundle of the FISP-SWCNTs scaffold, we first compare the microstructure of the FISP with and without SWCNTs. Both FISP-SWCNTs structures (Fig. 7.3 (b, c &d) and FISP (Fig. 7.4 (a)) show highly entangled and multi-connected micellar bundle networks and exhibit similar bundle-like networks with three fold junctions. Since wormlike micelles require less energy to create three fold junctions in comparison to the energy needed to bifurcate or fuse SWCNTs, we speculate that the junctions observed in the FISP-SWCNTs structure are mainly formed by wormlike micelles rather than inter-connected and fused SWCNTs.

The diameter of the micellar bundles in the FISP is $\sim$100$\pm$15 nm with a length of $\sim$350$\pm$45 nm [167], while FISP-SWCNTs scaffold exhibits a wider distribution of bundle diameters, ranging from 30 nm to 2 microns. We suspect that electrostatic interactions among CTAB molecules (positively charged), SWCNTs (positively charged), and SDS molecules (negatively charged) [204, 205, 207, 208, 222] introduce spatially inhomogeneously charged elements in the scaffold, yielding wider size distribution in the bundle diameter. Since an individual CTAB/NaSal wormlike micelle has a diameter of $\sim$5 nm and each thin FISP-SWCNTs bundle has an average diameter of $\sim$58$\pm$12 nm and a length $\sim$100-750 nm, each bundle possibly consists of $\sim$12 CTAB/NaSal wormlike micelles and SWCNTs.

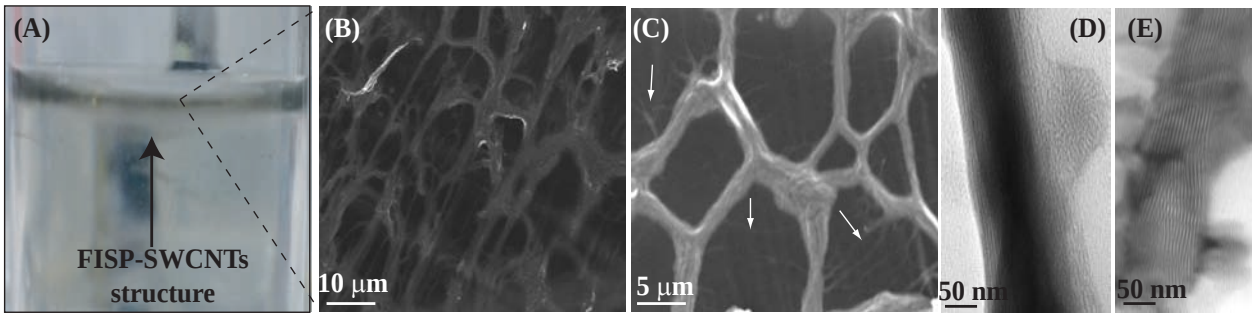


Figure 7.3: (a) Diluted FISP-SWCNTs scaffold suspended in DI-water after centrifugation. (b & c) SEM images of the FISP-SWCNTs showing interconnected bundle structures. Some SWCNTs can be observed in the scaffold (white arrows in c). (d & e) TEM images of the bundle structure composed by wormlike micelles and SWCNTs.

Similarly, Ben-David *et al.* [204] and Nativ-Roth *et al.* [205, 222] showed that CTAB wormlike micelles (concentration ranging ∼2–7 wt%) and SWCNTs (0.5–1 wt%) formed aligned bundle-like structures, where SWCNTs were sandwiched between the CTAB micelles (e.g., micelle-SWCNT-micelle). They also observed a characteristic inter-tube distance ∼15-25 nm inside a single bundle, with individual bundle thickness ∼100 nm. They concluded that the formation of such layered and aligned structures was due to chemical (both carbon based elements) and dimensional matching between CTAB micelles (diameter∼3-5 nm) and SWCNTs (diameter∼1-2 nm). Consistent with their dimensional matching argument, they observed that multi-walled carbon nanotubes (larger diameter than those of SWCNTs) were not able to form aligned structures with CTAB micelles. We propose that the formation of FISP-SWCNTs bundles in our work is induced by the electrostatic interactions, chemical composition, and geometric matching between CTAB wormlike micelles and SWCNTs. Even though SEM images of FISP-SWCNTs illustrate the detailed porous scaffold structure of FISP-SWCNTs, it is difficult to verify the location of SWCNTs within the bundle network. To address this challenge, we further conducted transmission electron microscopy (TEM) and compared the microstructure dimension and pixel mapping of three solutions: the SWCNTs-SDS dispersion solution, CTAB/NaSal wormlike micellar solution (IP), and FISP-SWCNTs scaffold (see Fig. 7.5). The contrast difference in TEM images correlate

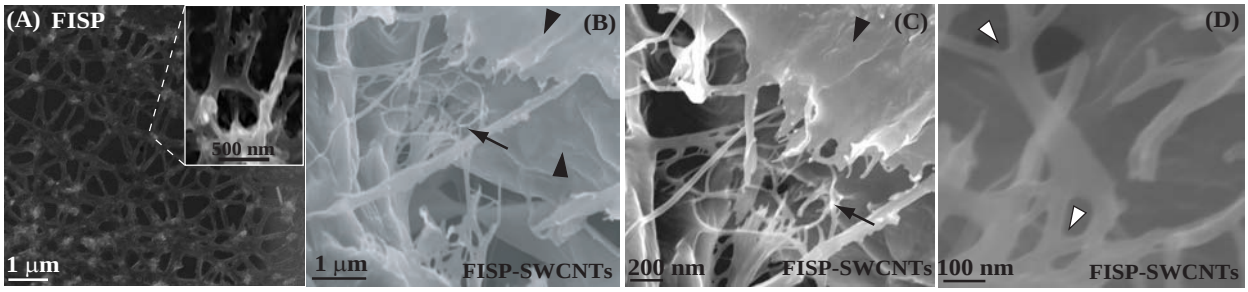


Figure 7.4: (a) SEM image of the FISP (without SWCNTs) shows highly entangled and multi-connected micellar bundles. The bright branches are the micellar bundles while the dark regions are pores. (b, c & d) SEM images of the FISP-SWCNT scaffold. Some thick layers of FISP-SWCNT are marked by black triangles in b & c. Some areas of the FISP-SWCNTs structure exhibit finer FISP-SWCNTs bundles, where some connection points can be observed (black arrows in (b & c). (d) is a high magnification SEM image showing three fold junctions (white triangles).

variations in electron densities: the space formed after the evaporation of water tends to be bright, while the space formed from the micelles and SWCNTs are shown as dark lines. Nativ-Roth *et al.* [222] analyzed TEM images of SWCNTs in CTAB micelles by using electron densitometry maps and concluded that SWCNTs exhibited lower intensity peaks in the electron densitometry maps. Here, we followed a similar procedure to obtain the pixel mapping of TEM images of 3 solutions. Fig. 7.5(a) shows the TEM image of SWCNTs dispersed in DI water and SDS, illustrating several SWCNTs with diameter ∼1 nm. The pixel map (along the white line) reveals that SWCNTs have a diameter of ∼1 nm with a gray intensity of ∼200 pixels. Fig. 7.5(b) is a TEM image of the ionic CTAB/NaSal wormlike micellar solution (IP), exhibiting bundles formed by 10-20 wormlike micelles with hundreds of nanometers in length [167]. The pixel map (along the white line) of IP shows a characteristic size of the CTAB micelle diameter of ∼5 nm and a gray intensity of ∼240 pixels. Finally, Fig. 7.5(c) is a TEM image of FISP-SWCNTs structure, exhibiting a primary peak around ∼250 pixels and a secondary peak (red arrows) around ∼210 pixels. By comparing all three cases, the secondary peaks shown in the FISP-SWCNTs bundle are most likely to be correlated with the encapsulated SWCNTs in the bundle while the primary peaks are consistent with the wormlike micelles intensity formed by CTAB/NaSal. By counting the

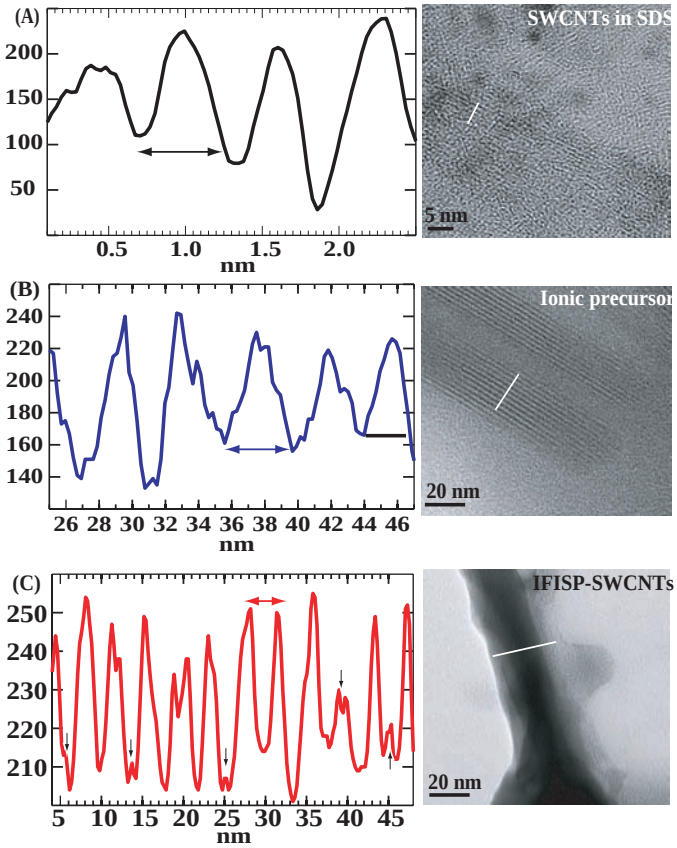


Figure 7.5: Pixel maps (left column) and TEM images (right column) of the SWCNTs-SDS dispersion (a), CTAB/NaSal wormlike micellar solution (b), and FISP-SWCNTs scaffold (c).

small peaks in the pixel map in Fig. 7.5(c), we conclude that individual bundle structure observed in FISP-SWCNTs contains ∼5 SWCNTs.

### *7.4.2 UV-Visible Spectroscopy*

To further verify the encapsulation of SWCNTs in the FISP structure, we conducted UV-vis spectroscopy by using a Varian Cary 5000 UV-Vis-NIR Spectrophotometer coupled with a temperature controller at 25 °C. A wave spectrum scan from 200 nm to 800 nm was conducted to identify the resonance peaks of the SWCNTs-SDS dispersion, precursor solution containing IP-SWCNTs-SDS, and FISP-SWCNTs.

Fig. 7.6(a) shows the absorbance spectra of SWCNTs and SDS (1 wt%) suspended in

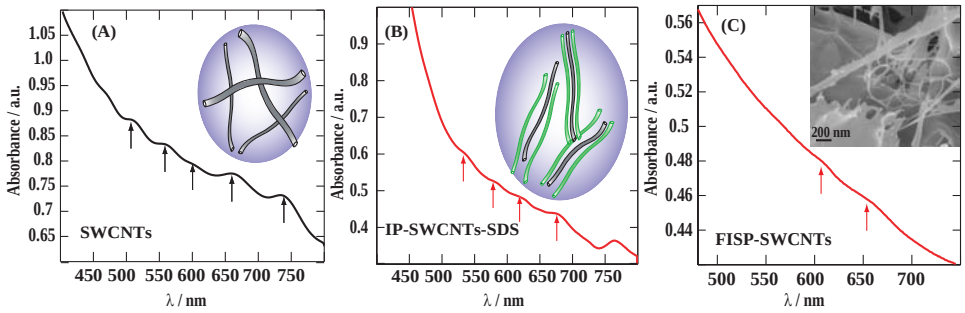


Figure 7.6: (a) UV spectra of SWCNTs-SDS suspended in DI water. The arrows highlight the characteristic resonance peaks of the SWCNTs at wavelengths of 500-800 nm. (b) The precursor IP-SWCNTs-SDS exhibits the characteristic resonances peaks of SWCNTs at wavelengths of 400-800 nm. The schematics in (b) shows the sandwiched and layered structure of SWCNTs based on the TEM images in Figure 7.5 (b). (c) UV spectra of FISP-SWCNTs scaffold. The resonance peaks of the SWCNTs also appear between 600-800 nm. Since SWCNTs are possibly encapsulated inside the FISP (inset in (c)), it shows a lower intensity of the resonance peaks of the FISP-SWCNTs.

water. The spectrum of SWCNTs-SDS dispersion shows characteristic resonance peaks related to $M_{11}$ at ∼400–800 nm [206, 217, 223, 224]. Fig. 7.6(b) exhibits the spectrum of the IP-SWCNTs-SDS precursor solution with resonance peaks of ∼400-800 nm, verifying the presence of SWCNTs in the precursor. The difference in the absorbance intensity is due to surfactant aggregates and sample preparation artifacts. Existing literature reported that the assembled surfactant aggregates would affect the UV-spectometry of SWCNTs [206, 217, 224]. It has also been reported that sample preparation (e.g., centrifuging or sonicating times), bundling and aggregations of SWCNTs could increase, decrease, or shift the UV spectra of SWCNTs [217]. The lower intensity in the resonance peaks from the spectrum plot in Fig. 7.6(c) is possibly due to the fact that SWCNTs have been encapsulated inside the FISP. Nevertheless, some resonance peaks between wavelength 600-750 nm (red arrows in Fig. 7.6(c)) were still observed.

In summary, we have used electron microscopy (SEM and TEM) and UV spectroscopy to verify the porous scaffold formed by wormlike micelles and SWCNTs bundles. In the next section, we show proof of concept studies of utilizing FISP-SWNCTs scaffolds for pH sensing applications.

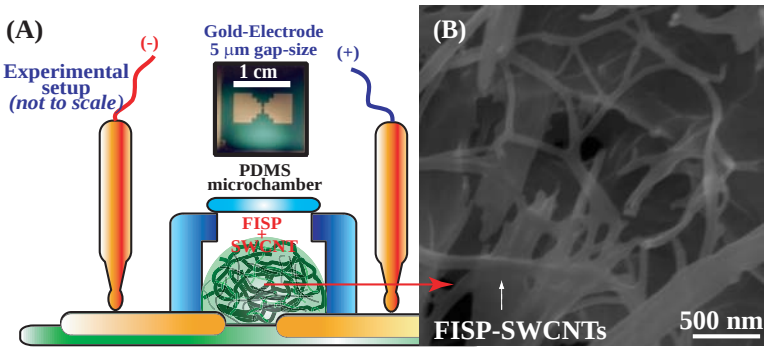


Figure 7.7: (a) Schematics of the experimental setup used to measure the conductivity in the FISP-SWCNTs structures. Approximately 3 $\mu$L of FISP-SWCNT was deposited on top of the gold electrode (5 $\mu$m gap size). Subsequently approximately 3 $\mu$L of pH buffer solution was added. After one minute, a DC voltage sweep was applied (from 0.0 to 1.0 V) to obtain the current versus voltage curves. (b) SEM image of the FISP-SWCNTs scaffold where multi-connected networks are observed.

### *7.5 Electro-conductive response of FISP-SWCNTs scaffold*

For potential sensing applications, FISP-SWCNTs scaffold was tested for pH sensing. Fig. 7.7 shows the schematics of the experimental setup to measure the conductivity in the FISP-SWCNTs structures. Approximately 3 $\mu$L of FISP-SWCNT was deposited on top of the gold electrode (5 $\mu$m gap size). Subsequently approximately 3 $\mu$L of pH buffer solution was added. After one minute, a DC voltage sweep was applied (from 0.0 to 1.0 V) to obtain the current versus voltage curves. Fig. 7.8 shows the IV curves of the FISP-SWCNTs scaffold in

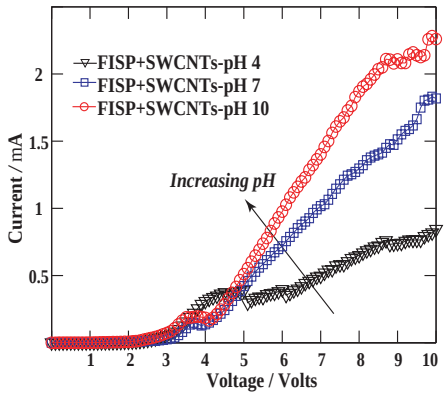


Figure 7.8: Representative curves of the current *versus* voltage response of gel-like FISP-SWCNT structures under different pH conditions.

3 buffer solutions with different pH levels. The conductivity of the FISP-SWCNTs scaffold increased as the pH value of the buffer solution increased. The IV curves of the FISP-SWCNTs exhibit mostly monotonic behavior for all pH values. Similar results have been reported by Weber *et al.* [214] where SWCNTs networks showed monotonic current *versus* voltage response. Based on the TEM and pixel imaging information in Figure 7.5, many SWCNTs are likely wrapped inside the FISP structure (less exposed to the environment), hence the interaction of ($OH^-$) group in the pH buffer solution and FISP-SWCNTs scaffold becomes less direct. In addition, the presence of surfactant SDS and CTAB molecules in the FISP-SWCNTs could affect the conductivity response of the FISP-SWCNTs scaffolds. Fu *et al.* reported that surfactants used to suspend and fabricate SWCNTs networks had strong effects in the electrical response of the integrated system [210]. In fact, surfactants can have different effects on the conductivity of SWCNTs. Cationic surfactants (e.g., CTAB) have shown to decrease the conductance in SWCNTs when the surfactant concentration was increased. Whereas anionic surfactants (e.g., SDS) increase the conductance of SWCNTs with increasing surfactant concentrations. These effects are related to the size and charge of the head groups of the surfactant molecule [210]. Hence the electro-conductive property of the FISP-SWCNTs potentially can have counter effects from CTAB and SDS surfactant molecules, inducing noises in the IV curve. To enhance the signal- to-noise ratio, the concentration of SWCNTs and surfactants can be optimized with a larger voltage to increase the electric current. In this work, we chose surfactant SDS to disperse SWCNTs and used surfactant CTAB to encapsulate SWCNTs to form electro-conductive scaffolds because extensive research has been reported on CTAB-SWCNTs aligned structures [204, 205, 222]. Our future research will focus on identifying alternative surfactant systems to improve the encapsulation of SWNCTs in a scaffold with enhanced conductivity signal. For example, the conductivity signal of a nonionic FISP-SWCNTs scaffold will be explored because of reduced electrostatic effects in the non-ionic surfactant solution [140].

### *7.6 Conclusions*

We presented a simple and low cost microfluidic assisted process to disperse and encapsulate low volumes of SWCNTs in a flow induced structured phase (FISP-SWCNTs), with the

possibility of scale-up operation at high throughput. The FISP showed good chemical and dimensional affinity with the SWCNTs. Evidenced by electron microscopy and UV-vis spectroscopy, porous FISP-SWCNTs scaffold shows multiconnected and entangled bundle-like structure, with individual bundle consisting of both wormlike micelles and SWCNTs. Our preliminary results of the electro-conductivity of the FISP-SWCNTs scaffolds demonstrate promises of using microfluidic procedure to synthesize electro-conductive SWCNTs gels for pH sensing. However, further work is required in selecting optimized surfactants and perfecting the synthesis procedure to improve the connectivity and homogeneity of SWCNTs in the FISP-SWCNTs scaffold. One-step microfluidic process presented in this work opens a new pathway to disperse and encapsulate SWCNTs in a micellar matrix without involving chemical reactions and extreme experimental conditions, with promising potentials for sensing, encapsulation, and catalysis applications.

# Chapter 8

# SUMMARY AND FUTURE WORK

## *8.1 Summary*

We have described experiments in this thesis wherein microrheology (one and two point passive microrheology), bulk rheology, SANS, TEM, SEM, and cryo-EM have been used to understand the behavior of micellar structures. A unifying theme of our work is that the combination of different experimental approaches and theoretical modeling could yield powerful insights into the inner behavior of micellar structures.

We have observed that by using just hydrodynamics conditions and micro-spatial confinement flow-induced structured phases (**FISP**) can be formed by using ionic and non-ionic micellar solutions. We have suggested that the combination of high strain rates ($\sim 10^3\ s^{-1}$), entropic fluctuations, flow-alignment, local gradient concentrations, and spatial confinement are the main reason to induce the formation of FISP. We observed that both wormlike micellar solutions and spherical micelles could form FISP, relating the FISP formation to the hydrodynamic conditions and spatial confinement rather than the type of the micellar structure. We have observed that the both ionic and non-ionic FISPs are composed by highly entangled and multiconnected micellar networks. The FISPs have shown to be stable after a year and with no change in their rheological properties after $\sim$1 month. We have proposed that the high entanglement density, electrostatic interactions, entropic attractions, hydrophobic interactions, and van der Waals forces are the main reasons to maintain stable and irreversible the structure of the FISPs.

We have used the FISPs for potential uses as nanotemplating, pH sensors and glucose sensors. Chapter 6 showed the formation of nano-toroidal structures by using different flow approaches, Chapter 7 presented the used of the ionic FISP to encapsulated single-walled carbon nanotubes for pH sensing purposes, and Chapter 8 exhibited the used of the non-ionic FISP for glucose sensing applications.

## *8.2 Future Work*

Here we describe new directions for the work in this dissertation. New work encompasses both further exploitation of FISP and more understanding of the properties (e.g., thermodynamic and dynamic) properties of the FISP.

### *8.2.1 Scale-up the production of the FISPs*

The production of large volumes (∼10 mL) of FISPs remains unsolved in this dissertation. Although, several approaches were tried to scale-up the production of FISPs none of them was successful. The FISP structure offers great potential for biomedical applications, micro and nano templating and sensing applications. Further, once the FISPs' production reaches larger volumes, the bulk rheometry could be performed, hence, the mircrorheological techniques presented in this dissertation could be corroborated.

### *8.2.2 Active microrheology*

The use of active microrheology could provide more information of the FISP's structure under shear. Porte *et al.* [6] proposed that highly connected micellar networks subjected to shear rate will exhibits high fluidity due to the "sliding-connection" theory. The FISP's structure will provide a perfect scenario to prove Porte *et al.* hypothesis. To date, this scenario has not been experimentally considered for highly entangled and multi-connected micellar bundles.

### *8.2.3 Thermodynamic properties of the FISPs*

Parameters such as the free energy of the FISPs, activation energy required to form FISPs, bending modulus $\kappa_c$ presented on the micellar bundles of the FISPs, and Hamaker constant of the FISPs are still unanswered. Hence, a complete study of the thermodynamic properties of the FISPs have to be performed.

### *8.2.4 Microstructure model of the FISPs*

The complete USANS–SANS spectra of the FISPs could not be fitted because currently there is not model that accounts for the structure factor presented in the FISPs. Hence, mathematical model that accounts the structure and form factors of the FISP has to be developed.

### *8.2.5 New systems*

The use of different materials such as polymers, bloc-copolymers, gemini surfactants, and Janus surfactants to form FISP has to be explored. Using different materials and solving the scale-up issue will open new pathways to create novel nano-materials for different applications.

# VITA

**In this vita, the narcissist author phychoanalyzes himself and narrates important past events absolutelty related to the materialization of this dissertation.**

The author was born in "La Atenas de Guanajuato" (a.k.a Salvatierra, lugar de los salvadolares). After happier experiences in primary and high-school, he enrolled in the Mexican Air Force with the intention of becoming a pilot. After quickly realizing his huge mistake he quit. Then, he spent 2 years of his life trying different colleges, however, he found those colleges depressing and boring. By the moment that he was having an existential shock, he met a fantastic girl (Ely) with whom he spent 8 years of his life. Ely helped him begin his adventure in "La Gran Tenochtitlan" (a.k.a Mexico city) by encouraging him to follow his dreams. After confronting his family, he quit college and left everything behind to begin his journey in "La Gran Tenochtitlan". After several months of challenging experiences but with the great help and support of Ely, the author enrolled at the National Autonomous University of Mexico (UNAM) where he studied Mechanical Engineering. The time at UNAM and "La Gran Tenochtitlan" was simply amazing. He did his bachelor research project under the supervision of Prof. Baltasar Mena Iniesta and graduated in 2009.

In 2009 he got accepted to the University of Washington to study his Masters in Mechanical Engineering in the Soft Matter and Microfluidics Lab. However, he got accepted with no funding so the author passed through some challenging experiences one more time. With the help of his family, master's adviser, and aunt Lety he was able to survive the first year of his Masters degree. Then, with the help of Ely and after $n$–iterations ($n = 3$) he obtained a CONACYT scholarship to finish his Masters program and start his PhD. During his PhD and his stay in the wonderful city of Seattle, the author made new friends and met amazing people.

After having enjoyed to the maximum during his stay at UW and Seattle, the author will continue doing research at the chaotic Daily-Life research center. Gracias a todos!

**Now, let's be serious:**

**Education**

**Dual Ph. D.**, Mechanical Engineering and Nanotechnology 06/11–06/14
University of Washington, Seattle, USA
Adviser: **Professor Amy Q. Shen**
Thesis: *Microfluidics enhanced synthesis of micellar nanostructures*

**M. S.**, Mechanical Engineering 09/09–06/10
University of Washington, Seattle, USA
Adviser: **Professor Amy Q. Shen**
Thesis: *Microrheology of a flow-induced structured phase in wormlike micelles*

**B. S.**, Mechanical Engineering, **with Highest Honors** 06/05–06/09
Universidad Nacional Autonoma de Mexico (UNAM), Mexico D.F
Adviser: **Professor Baltasar Mena**
Thesis: *Acoustic waves through granular materials under seismic motion*

**Publications**

1. **J. J. Cardiel**, Y. Zhao, JH. Kim, J. Chung & A. Q. Shen, "Electroconductive micro-scaffolds made of single-walled carbon nanotubes and wormlike micelles", **in revision in Carbon**, (2014)

2. **J. J. Cardiel**, M. Asgari, & A. Q.. Shen, "Toroidal Bundle Formation in Wormlike Micellar Solutions: Experiment, Modeling, and Material Characterization", **in revision in ACS-NANO**, (2014)

3. **J. J. Cardiel**, Y. Zhao, L. Tonggu, JH. Kim, L. Wang, J. Chung & A. Q. Shen, "Flow-induced immobilization of Glucose Oxidase (GOx) in micellar nano-scaffolds

for glucose sensing",
**in revision in Lab on a Chip**, (2014)

4. **J. J. Cardiel**, Y. Zhao, P. de la Iglesia, L. D. Pozzo & A. Q. Shen, "Microstructure and temperature studies of an ionic micellar structure composed by a $\pi - \pi$ organic salt", **Submitted to Soft Matter**, (2014)

5. **J. J. Cardiel**, A. C. Dohnalkova, N. Dubash, Y. Zhao, P. Cheung & A. Q. Shen, "Microstructure and Rheology of a Flow-Induced Structured Phase in Wormlike Micellar Solutions", **Proc. Natl. Acad. Sci. (PNAS)**, (2013), 110 (18), E1653-E1660.

6. **J. J. Cardiel**, A. C. Dohnalkova, L. Tonggu, P. de la Iglesia, D. Pozzo, L. Wang & A. Q. Shen, "Worming Their Way Into Shape: Toroidal Formations in Micellar Solutions", **ACS-NANO**, (2013), 7 (11), 9704-9713.

7. **J. J. Cardiel**, L. Tonggu, P. de la Iglesia, Y. Zhao, D. Pozzo, L. Wang & A. Q. Shen, "Flow-induced structured phase in nonionic micellar solutions", **Langmuir**, (2013), 29 (50), 15485-15495.

8. N. Dubash, **J. J. Cardiel**, P. Cheung, & Amy Q. Shen, "Irreversible flow-induced gelation in wormlike micellar solutions", **Soft Matter**, (2011), 7 (3), 876-879.

9. D. Lu, **J. J. Cardiel**, G. Cao & Amy Q. Shen, "Nanoporous scaffold with immobilized enzymes during flow induced gelation for sensitive $H_2O_2$ biosensing", **Advanced Materials**, (2010), 22 (25), 2809-2813.

## BIBLIOGRAPHY


[1] Israelachvili, J. *Academic Press* **1998**, New York.

[2] Cates, M.E.; Candau, S.J. *J. Phys. Condens. Matter* **1990**, 2:6869-6892.

[3] Rehage, H.; Hoffmann, H. *Mol. Phys* **1991**, 74:933-973.

[4] Berret, J.F. *in Molecular Gels, edited by R. G. Weiss and P. Terech, Springer, Dordrecht* **2006**, 667-720.

[5] Rehage, H.; Hoffmann, H. *American Chemical Society 1988*, 92:4712-4719.

[6] Porte, G; Gomati, R.; Haitami, O.E.; Appell, J.; Marignan, J.J. *J. Phys. Chem.* **1986**, 90:5746-5751.

[7] Appell, J.; Porte, G.; Khatory, A.; Kern, A.; Candau, S.J. *J. Physics II* **1992**, 2:1045-1052.

[8] Khatory, A.; Kern, F.; Lequeux, F.; Appell, J.; Porte, G.; Moire, N.; Ott A.; Urbach, W. *Langmuir* **1993**, 9:933-939.

[9] Candau, S.J.; Khatory, A.; Lequeux, F.; Kern, F. *J. Phys. IV* **1993**, 3:197-209.

[10] Shikata, T.; Hirata, H.; Kotaka, T. *Langmuir* **1988**, 4:354-359.

[11] Cappelaere, E.; Cressely, R. *Colloid. Polym. Sci.* **1998**, 276:1050-1056.

[12] Cappelaere, E.; Cressely, R. *Rheol. Acta* **2000**, 39:346-353.

[13] Kadoma, I.A.; van Egmond, J.W. *Phys. Rev. Lett.* **1996**, 76:4432-4435.

[14] Kadoma, I.A.; Ylitalo, C.; van Egmond, J.W. *Rheol. Acta.* **1997**, 36:1-12.

[15] Kadoma, I.A.; van Egmond, J.M. *Langmuir* **1997**, 13:4551-4561.

[16] Schubert, B.A.; Kaler, E.W.; Wagner, N.J. *Langmuir* **2003**, 19:4079-4089.

[17] Oelschlaeger, C.I.; Waton, G.; Candau, S.J. *Langmuir* **2003**, 19:10495-10500.

[18] Croce, V.; Cosgrove, T.; Maitland, G.; Hughes, T.; Karlsson, G. *Langmuir* **2003**, 19: 8536-8541.

[19] Oelschlaeger, C.; Schopferer, A.; Scheffold, F.; Willenbacher, N. *Langmuir* **2009** 25:716-723.

[20] Fischer E and Callaghan PT (2001). *Shear banding and the isotropic-to-nematic transition in wormlike micelles*. Phys. Rev. E 64:011501–1–15.

[21] Olmsted PD (2008). *Perspectives on shear banding in complex fluids*. Rheologica Acta 47:283-300.

[22] Hartmann, V.; Cressely, R. *EuroPhys. Lett.* **1997** 40:691-696.

[23] Hartmann, V.; Cressely, R. *Colloid Polym. Sci.* **1998**, 276:169-175.

[24] Liu, C.H.; Pine, D.J. *Phys. Rev. Lett.* **1996**, 77:2121-2124.

[25] Hu, Y.T.; Boltenhagen, P.; Pine, D.J. *J. Rheol.* **1998**, 42:1185-1208.

[26] Kim, W.J.; Yang, S.M. *Langmuir* **2002**, 16: 4761-4765.

[27] Kim, W.J.; Yang, S.M. *J. Colloid Interface Sci.* **2000**, 232: 225-234.

[28] Ouchi, M.; Takahashi, T.; Shirakashi, M. *J. Rheol.* **2006** 50:341-352.

[29] Vasudevan, M.; Shen, A.Q.; Khomani, B.; Sureshkumar, R. *J. Rheol.* **2008**, 52:527-550.

[30] Vasudevan, M.; Buse, B.; Lu, D.L.; Krishna, H.; Kalyanaraman, R.; Shen, A.Q.; Khomami, B.; Sureshkumar, R. *Nat. Mat.* **2010** 9:436-441.

[31] Ezrahi, S.; Tuval, E.; Aserin, A. *Adv. Colloid Interface Sci.* **2006**, 128:77-102.

[32] Lu, D.L.; Cardiel, J.; Cao, G.Z.; Shen, A.Q. *Adv. Mater.* **2010**, 22:2809-2813.

[33] Yang, J. *Curr. Opin. Colloid Interface Sci.* **2002**, 7:276-281.

[34] Varade, D.; Ushiyama, K.; Shrestha, L.K.; Aramaki, K. *J. Colloid Interf. Sci.* **2007**, 312, 489-497.

[35] Varade, D.; Sharma, S.C.; Aramaki, K. *J. Colloid Interf. Sci.* **2007**, 313, 680-685.

[36] Sharma, S.C.; Shrestha, R.G.; Shrestha, L.K.; Aramaki, K. *Colloid Polym. Sci.* **2008**, 286, 1613-1619.

[37] Sharma, S.C.; Acharya, D.P.; Aramaki, K. *Langmuir* **2007**, 23, 5324-5330.

[38] Sharma, S.C.; Abe, M.; Aramaki, K. in *Self-Organized Surfactant Structures* (ed T. F. Tadros), Wiley-VCH Verlag GmbH & Co. KGaA, Weinheim, Germany. **2010**.

[39] Sharma, S.C.; Tsuchiya, K.; Sakai, K.; Sakai, H.; Abe, M. **2009**, 335, 23-27.

[40] Sharma, S.C.; Shrestha, L.K.; Sakai, K.; Sakai, H.; Abe, M. *Colloid Polym. Sci.* **2010**, 288, 405-414.

[41] Bernheim-Groswasser, A.; Tlusty, T.; Safran, S.A.; Talmon, Y. *Langmuir* **1999**, 15, 5448-5453.

[42] Dan, N; Safran, S.A. *Advances in Colloid and Interface Science* **2006**, 123-126, 323-331.

[43] Tlusty, T.; Safran S.A. *Science* **2000**, 290, 1328-1331.

[44] Acharya, D.P.; Kunieda, H. *J. Phys. Chem. B* **2003** 107, 10168-10175.

[45] Clausen, T.M.; Vinson, P.K.; Minter, J.R.; Davis, H.T.; Ylamon, Y.; Miller, W.G. *J. Phys. Chem.* **1992**, 96, 474-484.

[46] Frounfelker, Bradley D. and Kalur, Gokul C. and Cipriano, Bani H. and Danino, Dganit and Raghavan, Srinivasa R.,*Langmuir* **2008**, 25, 167-172

[47] Dubash, N.; Cardiel, J.; Cheung, P.; Shen, A.Q. *Soft. Matters* **2011**, 7:876-879.

[48] Cheung, P.; Dubash, N.; Shen, A.Q. *Soft Matter* **2012**, 8:2304-2309.

[49] Xia, Y.; Whitesides, G.M. *Angew. Chem. Int. Ed.* **1998**, 37, 550-575.

[50] Macosko, C.W., *WILEY-VCH* **1994**

[51] Squires, T.M.; Manson, T.G. *Ann. Rev. of Fluid Mech.* **2010**, 42:413-438.

[52] Mason, T.G. *Rheol. Acta.* **2000**, 39:371-378.

[53] Mason, T.G.; Ganesan, K.; van Zanten, J.F.; Wirtz, D.; Kuo, S.C. *Phys. Rev. Lett.* **1997**, 79:3282-3285.

[54] Crocker, J. C., Valentine, M. T., Weeks, E. R., Gisler, T., Kaplan, P. D., Yodh,A. G., Weitz, D. A., *Phys. Rev. Lett.* **2000**, 85, 888-891

[55] Crocker, J. C., Grier, D. G., *J. Colloid and Interface Sci.* **1996**, 179, 298-310

[56] Levine, A.J. and Lubensky, T.C., *Phys. Rev. Lett.* **2000**, 85, 1774-1777

[57] SasView, http://www.sasview.org/.

[58] Kline, S.R.; *J. Appl. Cryst.* **2006**, 39, 895-890.

[59] Raghavan, S.R.; Fritz,G.; Kaler, E.W. *Langmuir* **2002**, 18, 3797-38102.

[60] Barker, J.G; Glinka, C.J.; Moyer, J.J; Kim, M.H.; Drews, A.R.; Agamalian, M. *J. Appl. Cryst.* **2005**, 38, 1004-1011.

[61] Takahashi, T.; Sakata, D. *J.Rheol.* **2011**, 55:225-240.

[62] Moss, G.R.; Rothstein, J.P. *J. Non-Newtonian Fluid Mech.* **2010**, 165:1505-1515.

[63] Turner, M.S.; Cates, M.E. *J. Phys.: Condens. Matter* **1992**, 4:3719-3741.

[64] Wang, Z.; Larson, R. *J. Phys. Chem. B.* **2009**, 113:13697-13710.

[65] Mohanty, S.; Davis, H.T.; McCormick, A.V. *Langmuir* **2001**, 17:7160-7171.

[66] Olsson, U.; Soderman, O.; Gudringt, P. *J. Phys. Chem.* **1986**, 90: 5223-5232.

[67] Drye, T.J.; Cates, M.E. *J. Chem. Phys.* **1992**, 96:1367-1375.

[68] Yamamoto, S.; Hyodo, S.J. *J. Chem. Phys.* **2005**, 122:204907(1)-204907(8).

[69] Helfand, E.; Fredrickson, G.H. *Phys. Rev. Lett.* **1989**, 62:2468-2471.

[70] Graessle, W.W. *Adv. Polym. Sci.* **1982**, 47:67-117.

[71] Li, X.B.; Lin, Z.C.; Cai, J.; Scriven, L.E.; Davis, H.T. *J. Phys. Chem.* **1995**, 99:10865-10878.

[72] Ziserman, L.; Abezgauz, L.; Ramon, O.; Raghavan, S.R.; Danino, D. *Langmuir* **2009**, 25:10483-10489.

[73] Shikata, T.; Pearson, D.S. *Langmuir* **1994**, 10:4027-4030.

[74] Galvan-Miyoshi, J.; Delgado, J.; Castillo, R. *Eur. Phys. J. E. Soft Matter* **2008**, 26:369-377.

[75] Rouse, P.E. *J. Chem. Phys.* **1953**, 21:1272-1280.

[76] Zimm, B.H. *J. Chem. Phys.* **1956** 24:269-278.

[77] Turner, M.S.; Cates, M.E. *Langmuir* **1991**, 7:1590-1594.

[78] Granek, R.; Cates, M.E. *J. Chem. Phys.* **1992**, 96:4758-4767.

[79] Shikata, T.; Hirata, H.; Kotaka, T. *Langmuir* **1989**, 5:398-405.

[80] Kern, F.; Lemarechal, P.; Candau, S.J.; Cates, M.E. *Langmuir* **1992**, 8:437-440.

[81] Berret, J.F.; Appell, J.; Porte, G. *Langmuir* **1993**, 9:2851-2854.

[82] Buchanan, M.; Atakhorrami, M.; Palierne, J.F.; MacKintosh, F.C.; Schmidt, C.F. *Phys Rev E Stat Nonlin Soft Matter Phys.* **2005**, 72:011504(1)-011504(9).

[83] Imae, T.; Kohsaka, T. *J. Phys. Chem.* **1992**, 96:10030-10035.

[84] Doi, M.; Edwards, S.F. *Oxford University Press: Oxford* **1986**.

[85] Cardiel, J.J; Dohnalkova, A.C.; Dubash, N.; Zhao, Y.; Cheung, P.; Shen, A.Q., *PNAS* **2013**, 110 (18), E1653-E1660.

[86] Abdel-Rahem, R., *Adv. Colloid Interface Sci.* **2008**, 141, 24-36.

[87] Acharya, Durga P. and Kunieda, Hironobu, *Adv. Colloid Interface Sci.* **2006**, 12312,401-413

[88] Zakin, J. L. and Lu, B. and Bewersdorff, H. W., *Rev. Chem. Eng.* **1998**, 14

[89] Maitland, G. C., *Curr. Opin. Colloid Interface Sci.* **2000**, 5, 301-311

[90] Abdel-Rahem, R. and Gradzielski, M. and Hoffmann, H. *J. Colloid Interface Sci.* **2005**, 288, 570-582

[91] Horbaschek, K. and Hoffmann, H. and Thunig, C. *J. Colloid Interface Sci.* **1998**, 206, 439-456

[92] Verma, Gunjan and Aswal, V. K. and Fritz-Popovski, Gerhard and Shah, C. P. and Kumar, Manmohan and Hassan, P. A., *J. Colloid Interface Sci.* **2011**, 359, 163-170

[93] Padalkar, Kshipra V. and Pal, Omprakash R. and Gaikar, Vilas G., *J. Mol. Liq.* **2012**, 173, 18-28,

[94] Hassan, P. A. and Valaulikar, B. S. and Manohar, C. and Kern, F. and Bourdieu, L. and Candau, S. J., *Langmuir* **1996**, 12, 4350-4357.

[95] Hassan, P. A. and Narayanan, J. and Menon, S. V. G. and Salkar, R. A. and Samant, S. D. and Manohar, C., *Colloids Surf. A* **1996**, 117, 89-94

[96] Mendes, E. and Narayanan, J. and Oda, R. and Kern, F. and Candau, S. J. and Manohar, C., *J. Phys. Chem. B* **1997**, 101, 2256-2258

[97] Lutz-Bueno, V. and Kohlbrecher, J. and Fischer, P., *Rheol. Acta* **2013**, 52, 297-312

[98] Tanaka, F., *Langmuir* **2010**, 26, 5374-5381

[99] Brackman, J. C. and Engberts, J., *Langmuir* **1991**, 7, 2097-2102

[100] Oelschlaeger, C. and Waton, G. and Candau, S. J. *Langmuir* **2003**, 19, 10495-500

[101] Raghavan, Srinivasa R. and Kaler, Eric W., *Langmuir* **2001**, 17, 300-306

[102] Croce, V. and Cosgrove, T and Maitland, G and Hughes, T and Karlsso, G., *Langmuir* **2003**, 20, 8536-85419

[103] Gravsholt, S., *J. Colloid Interface Sci.* **1976**, 57, 575-577

[104] Kaler, E. W. and Murthy, A. K. and Rodriguez, B. E. and Zasadzinski, J. A. N., *Surfactants Science* **1989**, 245, 1371-1374

[105] Brown, W. and Johansson, K. and Almgren, M. *J. Phys. Chem.* **1989**, 93, 5888-5894

[106] Kalur, G. C. and Frounfelker, B. D. and Cipriano, B. H. and Norman, A. I. and Raghavan, S. R., *Langmuir* **2005**, 21, 10998-11004

[107] Krishnaswamy, R. and Ghosh, S. K. and Lakshmanan, S. and Raghunathan, V. A. and Sood, A. K., *Langmuir* **2005**, 21, 10439-10443

[108] Mishra, B. K. and Samant, S. D. and Pradhan, P. and Mishra, Sushama B. and Manohar, C., *Langmuir* **1993**, 9, 894-898

[109] Mishra, Sushama and Mishra, B. K. and Samant, S. D. and Narayanan, Janaky and Manohar, C., *Langmuir* **1993**, 9, 2804-2807

[110] Nash, T. T. ,*J. Colloid Interface Sci.* **1958**, 13, 134-139

[111] Raghavan, Srinivasa R. and Kaler, Eric W. *Langmuir* **2001**, 17, 300-306

[112] Buhler, E. and Oelschlaeger, C. and Waton, G. and Candau, S. J., *J. Phys. Chem. B* **2004**, 108, 11236-11243

[113] Nemoto, N. and Kuwahara, M. and Yao, M. L. and Osaki, K., *Langmuir* **1995**, 11, 30-36

[114] Yin, Haiqing and Lin, Yiyang and Huang, Jianbin, K., *J. Colloid Interface Sci.* **2009**, 338 , 177-183

[115] Garg, Gunjan and Hassan, P. A. and Kulshreshtha, S. K., *Colloids Surf. A* **2006**, 275, 161-167

[116] Bijma, Koos and Engberts, Jan B. F. N., *Langmuir* **1997**, 13, 4843-4849

[117] Bijma, Koos and Rank, Elisabeth and Engberts, Jan B. F. N., *J. Colloid Interface Sci.* **1998**, 205, 245-256

[118] Savin, T., Doyle, P. S., *Biophys J.* **2005**, 88, 623638

[119] Crdoba, A., Schieber, J. D., Indei, T., *Phys. Fluids* **2012**, 24, 073103(1)- 073103(19)

[120] Pelletier, V., Gal, N.,Fournier, P. and Kilfoil, M. L., *Phys. Rev. Lett.* **2009**, 102,

[121] Gardel, M. L., Valentine, M.T. , Crocker, J. C., Bausch, A. R., Weitz, D. A., M., *Phys. Rev. Lett.* **2003**, 91

[122] McCabe, W. L. and Smith, J. C. and Harriott, P., *McGraw Hill* **2001**

[123] Dreiss, C.A. *Soft Matter* **2007**, 3, 956-970

[124] Ha, E.; Wang, W.; Wang, J.Y. *J. Pharm. Sci.* **2002**, 91, 2252-2264

[125] Kerwin, B.A. *J. Pharm. Sci.* **2008**, 97, 2924-2935

[126] Teepireddy, T.; Kumar, S. *Master Thesis, National Institute of Technology* **2011**, 1-62

[127] O'Sullivan, S.M.; Woods, J.A.; O'Brien, N.M. *Br. J. Nutr.* **2004**, 91(5), 757-764

[128] Radomska, R.; Dobrucki, R. *Int. J. Pharm.* **2000**, 196, 131-134

[129] Kabir-ud-Din; Sharma, G.; Naqvi, A.Z. *Colloids and Surfaces A: Physicochem. Eng. Aspects* **2011**, 385, 63-71

[130] Moulik, S.P.; Ghosh, S. *J. Mol. Liq.* **1997**, 72, 145-161

[131] Tan, A.L.; Laili, C.R.; Hamdan, S.; Doreen Ng, S.H. *J.Sci. Tech. UTHM* **2009**, 1, 1-12

[132] Rharbi, Y.; Li, M.; Winnik, M.A.; Hahn, K.G.Jr. *J. Am. Chem. Soc.*, **2000**, 122, 6242-6251

[133] Landazuri, G; Fernandez, V.V.A; Soltero, J.F.A.; Rharbi, Y. *J. Phys. Chem. B* **2012**, 116, 11720-11727

[134] May, S.; Bohbot, Y.; Ben-Shaul, A. *J. Phys. Chem. B* **1997**, 101, 8648-8657.

[135] Barentin, C.; Liu, A.J. *Europhys. Lett.* **2001**, 55 (3), 432-438.

[136] Bulut, S.; Hamit, J.; Olsson, U.; Kato, T. *Eur. Phys. J. E.* **2008** 27, 261-273.

[137] Bernheim-Groswasser, A; Wachtel, E.; Talmon, Y. *Langmuir* **2000**, 16, 4131-4140.

[138] Afifi, H.; Karlsson, G.; Heenan, R,K.; Dreiss C.A. *J. Coll. Intf. Sci.* **2012**, 378, 125-134.

[139] Dan, N.; Shimoni, K.; Pata, V.; Danino, D. *Langmuir* **2006**, 22, 9860-9865.

[140] Cardiel, J.J.; Tonggu, L.; Dohnalkova, A.; de-la-Iglesia, P.; Pozzo, D.; Wang, L.; Shen, A.Q.; *ACS NANO*, (2013).

[141] Forster, S.; Hermsdorf, N.; Leube, W.; Schnablegger, H.; Regenbrecht, M.; Akari, S.; Lindner, P.; Bottcher, C. *J. Phys. Chem. B* **1999**, 103, 6657-6663.

[142] Candau, S.J.; Oda, R., *Colloid and Surfaces A* **2001**, 183185, 5-14.

[143] Minot, E.D.; Anne M. Janssens, A.M.; Heller, I.; Heering, H.A.; Dekker, C.; Lemay, S.G.; *App. Phys. Lett.* **2007**, 91, 093507.

[144] Vaisman, L.; Wagner, H.D.; Marom, G. *Adv. Coll. Intf. Sci.* **2006**, 37-46,128130.

[145] Wang, Y., Q.; Chen, X.; . *Biosensors and Bioelectronics* **2011**, 25: 1356-1362.

[146] Humpolicek, P.; Kasparkova, V.; Saha, P.; Stejskal., J.; *Synthetic Metals* **2012** 162: 722 727.

[147] Sun, X.; Zaric, S.; Daranciang, D.; Welsher, K.; Lu, Y.; Li, X.; Dai, H. *JACS* **2000**, 45, 48-53.

[148] Alcock, S.J.; Turner, A.P. *Cranfield press, Bedford,* **1994**.

[149] Dennison, M.J.; Turner. A.P. *Biotechnol. Adv.* **1995**, 13, 1-12.

[150] Taxis du, D.P.; Miyamoto, P.S.; Murakami, T.; Kimura, J.; Karube, I. *Anal. Chim. Acta* **1990**, 235, 255-264.

[151] Gerard, M., A.; Malhotra, C.B.D. *Biosens. Bioelectron* **1990** , 17, 345-359

[152] Tlusty, T., Safran, S.A., Menes, R.; Strey, R., *Phys. Rev. Lett.* **1997**, 78, 2616-2619.

[153] Tlusty, T., Safran, S.A. *J. Phys.: Condens. Matter* **2000**, 12, A253-A262.

[154] Cates M.E.; Candau, S.J. *Europhys. Lett.* **2001**, 55, 887-893.

[155] In, M.; Aguerre-Chariol, O; Zana, R. *J. Phys. Chem. B* **1999**, 103, 7747-7750.

[156] Gummel, J.; Sztucki, M.; Narayanan, T.; Gradzielskib, M. *Soft Matter* **2011**, 117, 5731-5738.

[157] Padding, J.T.; Boek, E.S. *Phys. Rev. E* **2004**, 70, 031502(1)-031502(10)

[158] Helfrich, W. *Z. Naturforsch*, **1973**, C-28, 693-703.

[159] Sakaue, T. *J. Chem. Phys.* **2004**, 120, 6299-6304.

[160] Seifert, U. *Phys. Rev. Lett.* **1991**, 66, 2404-2407.

[161] Ou-Yang, Z.C. *Phys. Rev. A* **1990**, 41, 4517-4520.

[162] He, X.; Schmid, F. *Phys. Rev. Lett.* **2008**, 100, 137802(1)-137802(4).

[163] Zhang, J.; Li, X; Li, X. *Prog. Polym. Sci.* **2012**, 37, 1130-1176.

[164] Conwell, C.C.; Vilfan, I.D.; Hud, N.V. *PNAS* **2003**, 100, 92969301.

[165] Lu, Y.; Fan, H.; Stump, A.; Ward, T.L.; Rieker, T.; Brinker, J. *Nature* **1999**, 938, 223-226.

[166] Wang, B; Shum, H.C.; Weitz, D.A. *ChemPhysChem* **2009**, 10, 641-645.

[167] Cardiel, J.J.; Dohnalkova, A.; Dubash, N.; Zhao, Y.; Cheung, P.; Shen, A.Q. *PNAS* **2013**, 110, E1653.

[168] Pope, S.B. Turbulent flows. In *Cambridge University Press* **2000**.

[169] Jung, H.T.; Coldren, B.; Zasadzinski, J.A.; Iampietro, D.J.; Kaler, E.W. *PNAS* **2001**, 98, 1353-1357.

[170] Clausen, T. M., Vinson, P. K., Minter, J. R., Davis, H. T., Ylamon,Y., and Miller, W. G., *J. Phys. Chem.*, **1992**, *96*, 474.

[171] Michalet, X.; Bensimon, D. *J. Phys. II (France)* **1995**, 5, 263-287.

[172] Diat, O.; Roux, D.; Nallet, F. *J. Phys. II (France)* **1993**, 3, 1427-1452.

[173] Yusof, N.S.M.; Ashokkumar, M. *Soft Matter* **2013**, 9, 19972002.

[174] Safran, S. A., Pincus, P. A., Andelman, D., and MacKintosh, F. C., *Phys. Rev. A* **1991**, 43-2, 1071–1078.

[175] Moulin, R., Julien, S., Lecchi, A., Degrouard, J., and Impéror-Clerc M., *Soft Matter* **2013**, 9, 11085–11092.

[176] Coldren, B. A., Warriner, H., Zanten, R. V., Zasadzinski, J. A., and Sirota, E. B., *Langmuir* **2006**, 22, 2474–2481.

[177] Jung, H. T., Lee, S. Y., Kaler, E. W., Coldren, B., and Zasadzinski, J. A., *Proc. Natl. Acad. Sci.* **2002**, 99, 15318–15322.

[178] Jung, H. T., Coldren, B., Zasadzinski, J. A., Iampietro, D. J., and Kaler, E. W., *Proc. Natl. Acad. Sci.* **2001**, 98, 1353–1357.

[179] Cardiel, J. J., Tonggu, L., Dohnalkova, A. C., Iglesia, P., Pozzo, D. C., Wang, L., and Shen, A. Q., *ACS Nano*, **2013**, *7-11*, 9704–9713.

[180] Ou-Yang, Z.-C., *Phys. Rev. A*, **1990**, 41, 4517–4520.

[181] Bergström, L. M., *J. Colloid Interface Sci.* **2006**, 293, 181–193.

[182] Shikata, T., Dahman, S. J., and Pearson, D. S., *Langmuir* **1994**, 10, 3470–3476.

[183] Gradzielski, M. *Curr. Opin. Colloid Interface Sci.* **1998**, 3, 478–484.

[184] Nettesheim, F., and Wagner, N. J., *Langmuir* **2007**, 23, 5267–5269.

[185] Schubert, B. A., Kaler, E. W., and Wagner, N. J., *Langmuir* **2003**, 19, 4079–4089.

[186] Abillon, O., and Perez, E., *J. Phys. France* **1990**, 51, 2543–2556.

[187] Ohshima, H., and Hyono, A., *J. Colloid Interface Sci.* **2009**, 332, 251–253.

[188] Bergström, L. M., *J. Colloid Interface Sci.*, **2008**, *327*, 191–197.

[189] Lauw, Y., Leermakers, F. A. M., Stuart, M. A. C., *J. Phys. Chem. B*, **2003**, *107*, 10912–10918.

[190] Selby, S. M., *CRC Standard Mathematical Tables.*, CRC Press, 1973.

[191] Nakahara, H., Shibata, O., and Moroi, Y., *Phys. Chem. B*, **2011**, 115, 9077–9086.

[192] Goyal, P. S., Menon, S. V. G., Dasannacharya, B. A., and Rajagopalan, V., *Chem. Phys. Lett.*, **1993**, 211, 559–563.

[193] Dorshow R., Briggs J., Bunton C. A., Nlcoli D. F., *J. Phys. Chem.*, **1982**, 86, 2388–2395.

[194] Sonin, A. A., Seon, J-B., Yang, M-H, Jeong H-D. *Mol. Cryst. Liq. Cryst.*, **2006**, 451, 33–40.

[195] Spalla, O., and Kekicheff, P., *Langmuir*, **1994**, 10, 1584–1591.

[196] De Volder,M. F. L., Tawfick,S. H., Baughman, R. H., Hart,A. J., *Science* **2013**, 339, 535.

[197] Graham,A. P., Duesberg,G. S., Seidel,R. V., Liebau, M., Unger,E., Pamler,W., Kreupl,F., Hoenlein, W., *Small*, **2005**, 1, 382.

[198] Yan,Y., Chan-Park, M. B., Zhang, Q., *Small* **2007**, 3, 24.

[199] McEuen,P. L., Fuhrer,M., Park,H., *IEEE Trans. Nanotech.* **2002**, 1, 78.

[200] Moore,V. C., Strano,M. S., Haroz,E. H., Hauge, R. H., Smalley,R. E., Schmidt, J., Talmon,Y., *Nano Lett.* **2003**, 3, 1379.

[201] Kim,J. S., Song,K. S., Lee,J. H., Yu, I. J., *Arch Toxicol.* **2011**, 85, 1499

[202] Kato,H., Mizuno,K., Shimada,M., Nakamura,A., Takahashi,K., Hata,K., Kinugasa,S., *Carbon* **2009**, 47, 3434.

[203] Bystrzejewski,M., Huczko,A., Lange,H., Gemming,T., Buchner,B., Rummeli,M. H., *J. Colloid Interface Sci.* **2010**, 345, 138.

[204] Ben-David,O., Nativ-Roth,E., Yerushalmi-Rozen,R., Gottlieb,M., *Soft Matter* **2009**, 5, 1925.

[205] Nativ-Roth,E., Nap,R.J., Szleiferb,I., Yerushalmi-Rozen,R., *Soft Matter* **2010**, 6, 5289

[206] Rastogi,R., Kaushal, R., Tripathi,S.K., Sharma,A.L., Kaur,I., Bharadwaj,L.M., *J. Colloid Interface Sci.* **2008**, 328, 421.

[207] Richard,C., Balavoine, F., Schultz,P., Ebbesen,T. W., Mioskowski, C., *Science* **2003**, 300, 775.

[208] O'Connell,M. J., Bachilo,S. M., Huffman,C. B., Moore,V. C., Strano,M. S., Haroz,E. H., Rialon,K. L., Boul, P. J., Noon,W. H.,Kittrell, C., Ma,J., Hauge,R. H., Weisman,R. B., Smalley,R. E., *Science* **2002**, 297, 593.

[209] Ghosh, M., Maiti,S., Dutta,S., Das, D., Das,P. K., *Langmuir* **2012**, 28, 1715.

[210] Fu, Q., Liu,J., *Langmuir* **2005**, 21, 1162.

[211] Calvaresi,M., Dallavalle, M. , Zerbetto,F., *Small*, **2009**, 5, 2191.

[212] Lee,K., Kwon,J. H., Moon, S., Cho, W. S., Ju,B. K., Lee, Y. H., *Mater. Lett.* **2007**, 61, 3201.

[213] Zhao, W., Song,C., Pehrsson,P. E., *J. Am. Chem. Soc.* **2002**, 24, 12418.

[214] Weber,J., Kumarc,A., Kumara,A., Bhansali, S., *Sens. Actuators, B* **2006**, 117, 308.

[215] Lee,D., Cui,T., *Biosens. Bioelectron.* **2010**, 25, 2259.

[216] Yang, C. F., Chen,C. L., Busnaina,A., Dokmeci,M. R., *31st Annual International Conference of the IEEE EMBS* **2009**.

[217] Hirano,A., Tanaka,T., Urabe,Y., Kataura,H., *ACS Nano* **2013**, 7, 10285.

[218] Timmermans,M. Y., Estrada,D., Nasibulin,A. G., Wood,J. D., Behnam,A., Sun,D., Ohno,Y., Lyding,J. W., Hassanien, A., Pop, E., Kauppinen, E. I., *Nano Res.*, **2012**, 5, 307.

[219] Xie,J., Wang,H., Bai,H., Yang,P., Shi,M., Guo,P., Wang,C., Yang,W., Song, H., *ACS Appl. Mater. Interfaces* **2012**, 4, 2891.

[220] Islam,M. F., Rojas, E., Bergey,D. M., Johnson,A. T., and Yodh,A. G., *Nano Lett.* **2003**, 3, 269.

[221] Vaisman,L., Wagner,H. D., Marom, G., *Adv. Colloid Interface Sci.* **2006**, 128, 37.

[222] Nativ-Roth,E., Yerushalmi-Rozen,R., Regev,O., *Small* **2008**, 4, 1459.

[223] Hagen,A., Hertel, T., *Nano Lett.* **2003**, 3, 383.

[224] Geng,H. Z., Lee,D. S., Kim,K. K., Han,G. H., Park,H. K., Lee,Y. H., *Chem. Phys. Lett.* **2008**, 455, 275.

[225] Pickup,J.C., *Diabetes Care* **1993**, 16, 335-339,

[226] McNichols,R. J. and Cote, G.L., *J. Biomedical Optics* **2000**, 5, 5-16,

[227] Kimmel,D. W., LeBlanc,G. , Meschievitz,M.E., and Cliffel,D. E., *Anal. Chem.* **2012** , 84, 685-707,

[228] Lin, P. and Yan,F., *Adv. Mater* **2012**, 24, 34-51, .

[229] Kros,A., van Hovell, S. W. F. M., Sommerdijk, N. A. J. M., and Nolte, R. J. M., *Adv. Mater.* **2001**, 13, 1555-1557,

[230] Yang, Y., Yi, C., Luo, J., Liu, R., Liu, J., Jiang, J. , Liu, X., *Biosensors and Bioelectronics* **2011**, 26, 26072612,

[231] P.D. Gaikwad, D.J. Shirale, V.K. Gade, P.A. Savale, H.J. Kharat, K.P. Kakde, and M.D. Shirsat, *Int. J. Electrochem. Sci.* **2006** , 1, 425-434,

[232] Liu,J., Agarwal, M., Varahramyan, K., *Sensors and Actuators B* **2008**, 135, 195-199,

[233] Nien, P-C., Tung, T-S., Hoa,K-C., *Electroanalysis* **2006**, 18, 1408-1415,

[234] Borole,D. D. , Kapadi,U. R., Mahulikar, P. P. , and Hundiwale,D. G. , *Polym. Adv. Technol.* **2004**, 15, 306312,

[235] Wang ,Z. , Liu,S., Wu, P. , and Cai,C., *Anal. Chem.* **2009** , 81, 16381645,

[236] Hiller,M. , Kranz, C. , Huber,J., Bauerle,P. and Schuhmann,W., *Adv. Mater.* **1996**, 8, 219-222,

[237] Ammam,M., Easton, E. B. , *Sensors and Actuators B* **2011**, 155, 340-346

[238] Gutierrez,F., Rubianes,M. D., Rivas, G. A., **2012** 161, 191-197,

[239] Wang X. and Uchiyama, S., *Analytical Letters* **2008**, 41, 1173-1183,

[240] Rai,P., Ho,T., Xie,J., Hestekin, J.A., and Varadan,V.K., *J. Nanotechnology in Engineering and Medicine* **2010** , 1, 021009-1–0121009-7,

[241] Luckarift, H. R., Ivnitski, D., Rincon,R., Atanassov,P., Johnson,G. R., *Electroanalysis* **2010**, 22, 78-792,

[242] Palestino, G.,Legrosa, R., Agarwal,V., Perezd,E., Gergelya,C., *Sensors and Actuators B* **2008**, 135, 27-34,

[243] Zhou,K., Zhu,Y., Yang,X., Li,C., *Electroanalysis* **2010**, 22, 259-264,

[244] Lee,D., Lee,J., Kim,J., Kim,J. , Na,H. B. , Kim, B., Shin,C-H., Kwak,J. H.,Dohnalkova, A. , Grate,J. W.,Hyeon, T. , and Kim, H-S., *Adv. Mater.* **2005**, 17, 2828-2833,

[245] Yoshimoto, M. , Sato,M. ,Wang, S. , Fukunaga,K. ,Nakao,K. , *Biochemical Engineering J.* **2006** , 30, 1580-163,

[246] Blin,J.L., Carteret,C., Bleta,R., Stebe, M.J., *Coll. Surf. A: Physicochem. Eng. Aspects* **2010** , 357, 128-135,

[247] Olea,D.,Viratelle, O., Faure,C., *Biosens Bioelectron* **2008** , 18, 788-94,

[248] Kamyshny,A., Danino, D., Magdassi,S., and Talmon,Y., *Langmuir* **2002**, 18, 3390-3391,

[249] Haouz,A., Twist,C., Zentz,C., Tauc, P. ,Alpert, B., *Eur. Biophys. J.* **1998** , 27, 19-25,

[250] Wang,J., *Electroanalysis* **2004** , 17, 7-14,